

Corso di Dottorato in Ingegneria Biomedica XXVII ciclo

POLITECNICO DI TORINO



Doctoral Thesis

# **Analysis of sEMG on biceps brachii and brachioradialis in static conditions**

Effect of joint angle and contraction level

**Subaryani Dambawati Harjaya Soedirdjo**

**Supervisor:**

A handwritten signature in purple ink that reads "R. Merletti".

**Prof. Roberto Merletti**

May 2016



## **ACKNOWLEDGEMENTS**

I would like to thank my supervisor Prof. Roberto Merletti for his precious support, guidance and supervision.

My gratitude is extended to all my colleagues of the Laboratory for Engineering of the Neuromuscular System. I would like to thank Rev. Steven Henrich, O.S.C. for his great help and effort on editing this manuscript.

Finally, this work would not have been possible without the support of my parents and my brother.



LVMINA SI QVAERIS, BENEDICTE, QUID ELIGIS ANTRA?  
QUÆSITI SERVANT LVMINIS ANTRA NIHIL.  
SED PERGE IN TENEBRIS RADIORVM QUÆRERE LUCEM  
NONNISI AB OSCURA SIDERA NOCTE MICANT.



# CURRICULUM VITAE

Subaryani Dambawati Harjaya Soedirdjo was born in Jakarta, Indonesia, in 1986. In August 2011 she graduated in Biomedical Engineering at Institut Teknologi Bandung, Indonesia.

In the same year she worked within the laboratory of Biomedical Engineering in the same university to develop a software to store an X-RAY photo of a patient to standardize format (DICOM). She also develop a text to speech software for Bahasa Indonesia using syllable concatenation.

In 2012 she started the Ph.D. in Biomedical Engineering at Politecnico di Torino. Her main research interests are in the areas of signal processing applied to biomedical signals, basic and applied physiology of the neuromuscular system, human kinesiology, and robotic prosthetics.

## *List of Publications in International Journals*

### Review Articles:

Hutabarat, Mervin T, and Subaryani D H Soedirdjo. 2010. "Safety System Design Simulation for Transcutaneous Electrical Nerve Stimulator Using Electrode Contact Test." *IJEHMC* 1 (3): 79–89. doi:10.4018/jehmc.2010070108.

## *Presentations at national and international conferences*

1. Soedirdjo, S D H, K Ullah, and R Merletti. 2015. "Power Line Interference Attenuation in Multi-Channel sEMG Signals : Algorithms and Analysis." In 37th Annual International Conference of the IEEE Engineering in Medicine and Biology Society (EMBC), 2:3823–26.
2. Soedirdjo S.D.H., Merletti R. Comparison of different digital filtering techniques for surface EMG envelope recorded from skeletal muscle. "XX Congress of The International Society of Electrophysiology and Kinesiology", Rome, Italy, July 15-18, 2014.
3. Soedirdjo, Subaryani D H, Hasballah Zakaria, and Richard Mengko. 2011. "Indonesian Text-to-Speech Using Syllable Concatenation for PC-Based Low Vision Aid." In Proceedings of the 2011 International Conference on Electrical Engineering and Informatics, ICEEI 2011. doi:10.1109/ICEEI.2011.6021792.
4. Soedirdjo, Subaryani D H, Ine Renata Musa, Tati L R Mengko, and Iwan Sovani. 2010. "Low Vision Aid with Image to Text Converter to Enhance Magnified Text

Image.” In 6th World Congress of Biomechanics (WCB 2010). August 1-6, 2010 Singapore, 1386–89.

5. Soedirdjo, S. D H, and Mervin T. Hutabarat. 2009. “Microcontroller-Based Transcutaneous Electrical Nerve Stimulator with 8 Bit Cascade DAC.” In International Conference on Instrumentation, Communication, Information Technology, and Biomedical Engineering 2009, ICICI-BME 2009. doi:10.1109/ICICI-BME.2009.5417264.

#### Accepted manuscript

Soedirdjo S.D.H., Afsharipour B., Cattarello P., Merletti R. Errors in RMS amplitude estimation attributable to the Inter Electrode Distance of the surface EMG electrode grids. “XXI Congress of The International Society of Electrophysiology and Kinesiology”, Chicago, USA, July 5-8, 2016

#### Submitted manuscript

1. Cattarello P., Soedirdjo S.D.H., Afsharipour B., Merletti R. Effect of electrode size on amplitude estimation of HDsEMG maps. “3rd International Conference on NeuroRehabilitation (ICNR2016)”, Segovia, Spain, October 18-21, 2016
2. Soedirdjo S.D.H., Afsharipour B., Cattarello P., Merletti R. Introduction to EMG for the study of movement: from bipolar to high-density. “3rd International Conference on NeuroRehabilitation (ICNR2016)”, Segovia, Spain, October 18-21, 2016







# Table of contents

<b>Abstract</b>	<b>1</b>
<b>PART I: Methodological Issues</b>	
<b>Chapter I</b>	
Human elbow joint ang surrounding muscles	9
Normalizing force	10
EMG, force, and elbow joint angle	11
Objectives	13
Structure of the Thesis	13
Main results and future perspectives	14
<b>Chapter II</b>	
Power Line Interference attenuation in multi-channel sEMG signals: algorithm and analysis	19
<b>Chapter III</b>	
Extracting surface EMG envelope	31
<b>Chapter IV</b>	
Effect of subcutaneous layer thickness on the recorded sEMG	47
<b>PART II: High density detection system</b>	
<b>Chapter V</b>	
Electrode's size and estimation of biceps brachii muscle activity	63
<b>Chapter VI</b>	
Surface EMG spatial frequency bandwidth analysis	75
<b>Chapter VII</b>	
Effect of inter-electrode distance on RMS amplitude estimation	89
<b>PART III: Applications</b>	
<b>Chapter VIII</b>	
Effect of elbow joint angle and contraction level on the RMS of sEMG	107
<b>General Conclusions</b>	<b>124</b>



# *Abstract*





Despite several previous investigations, the direct correlation between the elbow joint angle and the activities of related muscles is still an unresolved topic. The sEMG signals were recorded from biceps brachii (6x8 electrodes, 10mm IED,  $\varnothing=3\text{mm}$ ) and brachioradialis (1x8 electrodes, 5mm IED,  $\varnothing=3\text{mm}$ ) of ten subjects. The subjects were asked to perform isometric elbow flexion at five joint angles with four contraction levels with respect to the maximum contraction (MVC) at that joint angle. The RMS values of biceps brachii (BB) and brachioradialis (BR) are computed within 500ms epoch and averaged over the muscle's active region. These values increase along as force increases regardless the joint angle. Concerning the different joint angle, we found that as the arm extended, the RMS values of seven subjects decreased, while the RMS values of three subjects increased. This behavior suggests different strategies of muscle contribution to the task in different subjects but may also be attributed to the technical issues discussed in Chapter 2 - 7.

Prior to this investigation, several issues related to the sEMG signals recording and processing were evaluated. Analysis on the effect of different elbow joint angle on the position of the innervations zone (IZ) of biceps brachii muscle indicates that the IZ shifts distally  $24\pm 9\text{mm}$  as the subjects extend their arms. Thus to assure sEMG signal recording, a grid of electrodes is selected instead of bipolar electrodes.

The issue of spatial aliasing, which has not been addressed before, was studied. Greater electrode's diameter implies higher spatial low pass filtering effect which gives an advantage as anti-aliasing filter in space. On the other hand, this low pass filtering effect increase the error on the power for the single sEMG image ( $\varnothing=10\text{mm}$ , 10mm IED) to  $3\pm 13.5\%$  compared to the continuous image. Larger IED introduces RMS estimation error up to  $\pm 18\%$  for the single sEMG image (15mm IED). However, taking the mean of a group of maps, the error of the mean is negligible ( $<3\%$ ).

Furthermore, the envelope of the rectified EMG has been investigated. Five digital low pass filters (Butterworth, Chebyshev, Inverse Chebyshev, and Elliptic) with five different orders, four cut off frequencies and one or bi-directional filtering were tested using simulated sEMG interference signals. The results show that different filters are optimal for different applications. Power line interference is one of the sources of impurity of the sEMG signals. Notch filter, spectral interpolation, adaptive filter, and adaptive noise canceller with phase locked loop were compared. Another factor that affects the amplitude of sEMG is the subcutaneous layer thickness (ST). Higher contraction level and greater elbow joint angle lead to thinner ST. RMS values tend to decrease for thicker ST at a rate of 1.62 decade/decade.





# Part I



*EMG signal processing:  
Methodological issues*



# Chapter I

*Introduction of sEMG  
recordings from biceps brachii  
at different force levels and  
elbow joint angles:  
State of the art and research questions*



## Introduction of sEMG recordings from biceps brachii at different force levels and elbow joint angles

### State of the art

#### *Human elbow joint and surrounding muscles*

The complexity of the elbow joint provides us with a stable flexion and extension mechanism, slight medial and lateral mobility, and medial-lateral rotation [1]. It allows us to accomplish various activities of daily living such as dressing, hygiene, tying a shoe, eating, using a telephone, and opening a door. These activities are accomplished with a varied arc of motion [2]. Muscles around the elbow joint not only provide a dynamic stabilizer but also provide movements.

The primary flexors of the elbow are the brachialis (BS), the biceps brachii (BB), and the brachioradialis (BR) muscle (see Figure 1). The biceps brachii muscle has two heads at its origin, i.e. the short and long heads. Each of them is attached to the coracoid process and superior glenoid aspect respectively. At the distal, this muscle inserts on the radial tuberosity. The brachialis muscle originates on both the humerus and the intermuscular septum and inserts on the anterior side of the proximal ulna. The elbow flexor muscle, which runs exclusively across the elbow, is the brachioradialis. The brachioradialis originates from the intermuscular septum and the lateral aspect of the distal humerus and inserts on the distal radius.

From the biomechanics point of view, the muscle that has the greatest mechanical advantage is brachioradialis while the muscle that suffers from a poor mechanical advantage is the brachialis [1]. This mechanical advantage is expressed as greater moment arm as shown in Figure 2 [3]–[6].

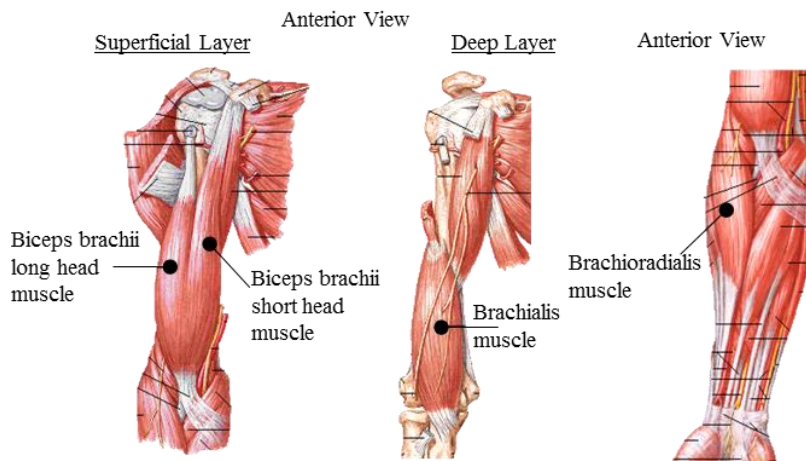


Figure 1. The anatomy of the elbow flexor muscles: biceps brachii, brachialis, and brachioradialis. The image is taken from [7].

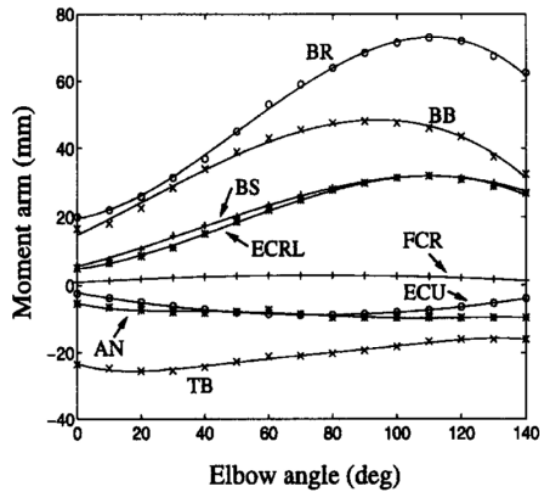


Figure 2. The moment arm of each muscle is changing depends on the elbow joint angle. Eight muscles are presented in this plot: brachioradialis (BR), biceps brachii (BB), brachialis (BS), extensor carpi radialis longus (ECRL), flexor carpi radialis (FCR), extensor carpi ulnaris (ECU), anconeus (AN), and triceps brachii (TB). This plot is reproduced from [5].

Since the force around the joint must be in equilibrium and its balance should lead to a zero resultant [1], the coordination of muscle activation to exert certain force should exist. As the consequence of variation on the muscle's moment arm, the force contribution of each muscle for the same loads also changes according to the joint angle. In the isometric contraction, the torque contribution of BB (both heads) increases at a greater elbow joint angle while for the other elbow flexor muscles (BR and BS) the torque contribution decreases [8].

### Normalizing force

The forces around the joint must be in equilibrium and their balance should lead to zero resultant [1]. As the consequence of variation on the muscle's moment arm, the force contribution of each muscle for the same loads also changes according to the joint angle. In the isometric contraction, the torque contribution of BB (both heads) increases at greater elbow joint angle while for BR and BS muscles, the torque contributions decrease [8].

To produce a certain amount of force, the muscles need to contract. It has been demonstrated that the maximum force exerted by the elbow flexor muscles (MVC) depends on the elbow joint angle (see Figure 3). The joint angle was observed to have a significant effect on the resultant MVC force for both flexion and extension of the elbow joint [9].

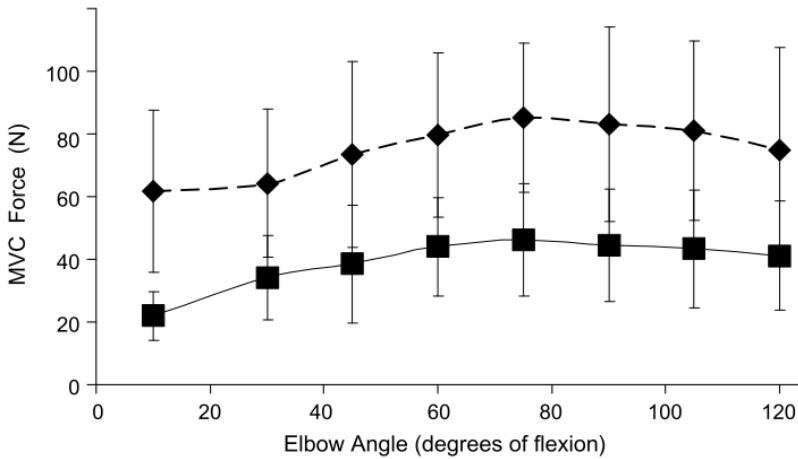


Figure 3. The MVC force on elbow flexion (◆) and extension (■) depends on the elbow joint angle. Plot reproduced from [9]

Normalization of the force must be set to allow a proper comparison of muscle activation. The force normalization can be made with respect to the maximum force produced at one arbitrary angle or to the maximum force produced at each joint angle. The first method of normalization assumes that for each joint angle the muscles produce the same torque. Since the MVCs at different joint angles is different, the percentage of force produced by the muscle at the reference joint angle will not reflect an equal force percentage at the other joint angles.

The second method is normalization with respect to the MVC at each joint angle. In this work, the second method of normalization is used thus the percentage of force to its MVC is maintained.

Up to this point, there are two factors that affect contraction of the elbow flexor muscle: the elbow joint angle and the force exerted by the muscle. One of the methods to analyze the muscle contraction is through the biophysical signal generated by the motor unit of the muscle, named electromyogram (EMG).

#### *EMG, force, and elbow joint angle*

The relationship between an EMG signal amplitude and a force (torque) has been addressed in the literature, e.g. [9]–[11]. The relationship demonstrates that the amplitude of the EMG increases non-linearly along with an increasing force level. On the other hand, the relation between the EMG signal amplitude and joint angle has been and is still discussed with diverging results [9], [12]–[14]. One hypothesis by Uchiyama et al [12] is, that the envelope of the rectified EMG decreased as the subjects flexed their arms. Doheny et al [9] reported no difference in the RMS value of the EMG as the arm flexed. In contrast, Kleiber et al [13] and Werder et al [14] demonstrate that the envelope of the rectified EMG increased as the subjects flexed their arms.

These contradictory results might arise as the consequence of inaccurate sEMG signal acquisition. Although a guideline for bipolar electrode placement has been developed [15], still the recorded signals can still be affected by several factors such as the shifts of innervation zones (IZ) due to changing of the elbow joint angle. The IZ was reported to shift up to 30mm distally [16] as the subjects extended their arms. This issue is important since the IZ could alter the sEMG signal recording, i.e. the amplitude of the EMG signals recorded in single differential configuration is nearly zero (see Figure 4) [17], [18]. Although the general locations of the IZ for both superficial elbow flexor muscles (BB and BR) are known (see Figure 5) [19], the result is still vulnerable unless the location of the IZ was detected before attaching the bipolar electrode. Therefore, a linear array or grid of electrodes is suggested for this purpose[20].

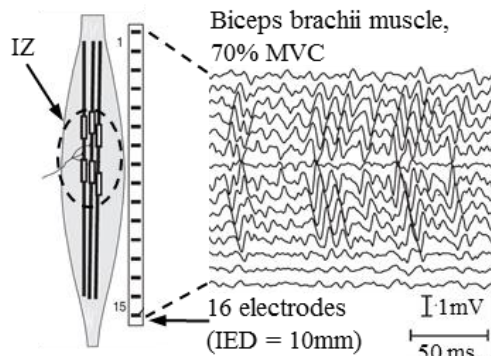


Figure 4. The single differential signal obtained from biceps brachii muscle contracted at 70% MVC shows that the amplitude of the signals is lower at the IZ. The image was taken from [21].

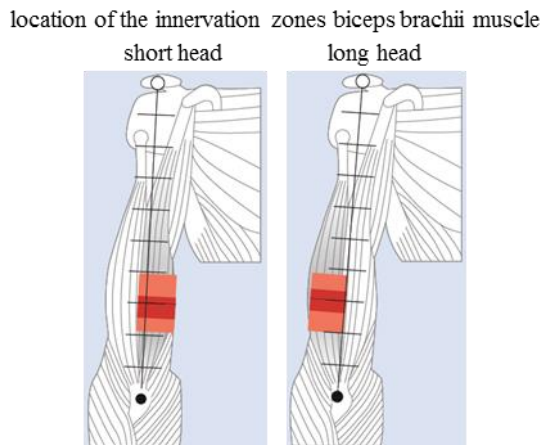


Figure 5. Common IZ location of the biceps brachii short head and long head obtained from 40 subjects (20 males and 20 females). The pink area in each figure shows the range of IZ location. The edges of the red area show the location of IZ for 25% and 75% of the subjects. The figure depicted from [19].



In this study, a 2D grid of electrodes is used to avoid the issue of the IZ shifts. SENIAM recommendations [15] indicates required bipolar electrode configurations but not for a linear array nor a grid of electrodes. To my knowledge, a guideline for the 2D electrodes' configuration does not exist. Therefore, the second part of this thesis (*Evaluating a grid of electrodes*) is dedicated to investigating optimal 2D electrode configurations: a) the electrode size (Chapter V), b) the sEMG spatial bandwidth (Chapter VI), and c) the effect of IED on sEMG spatial RMS (Chapter VII).

Another issue that might reduce the quality of the recorded signal is power line interference. Even with good skin preparation and the use of well-designed instrumentation this interference still appears. Therefore, an adequate signal processing method is needed [22]. The investigation of several signal processing methods to attenuate the power line interference is addressed in Chapter II.

After assuring that the measurement system and the pre-processing method of the signal are sufficient, an investigation on the correlation between the EMG recorded from biceps brachii and brachioradialis is presented in the third part of this thesis.

### **Objectives**

This Ph.D. thesis contributes to the research field through the analysis and interpretation of multichannel surface EMG signals during different elbow joint angle and contraction level. Furthermore, evaluation of spatial characteristic of the recorded sEMG signals which have not been addressed before was studied.

The main objectives of the thesis were to:

1. establish the optimal configuration of the 2D surface EMG detection systems in order to allow a correct sEMG features estimation;
2. evaluate different digital low pass filtering techniques to obtain the envelope of sEMG;
3. assess a suitable method to attenuate power line interference;
4. study the effect of subcutaneous layer thickness on the sEMG recording;
5. examine the effect of elbow joint angle and force level on the sEMG RMS amplitude;

### **Structure of the Thesis**

This work is structured in three parts.

#### *Part 1. EMG signal processing: Methodological issues*

This section focuses on methodological issues concerning signal acquisition and processing. Chapter I includes a brief introduction to the anatomy structure of an elbow joint angle and surrounding muscles, the issue of normalization, and the effect of

1  
innervation zones on the bipolar recording. Chapter II reports a study of different signal processing techniques to attenuate the power line interference on the multichannel simulated monopolar sEMG signal.

Chapter III describes an investigation of the advantages and disadvantages of several digital low pass filters that can be used to obtain the envelope of the rectified interference sEMG signals. Evaluations were made on the root mean square error between the ARV of the output and input signals, the rise time of the output signal, the computation time, and the delay. Furthermore, in Chapter IV, the effect of the subcutaneous layer on the sEMG signal recordings is discussed.

Realizing that a bipolar recording is not sufficient, we use a 2D grid of electrodes. Since a guideline of 2D electrodes configuration does not exist the second part of this thesis is dedicated to investigate this issue.

### *Part 2. High density detection systems: evaluating optimal configuration*

Chapter V describes the effect of electrode size on the power of a sEMG map at an instantaneous time. The monopolar sEMG signals were recorded using a grid of electrodes (16x8,  $\varnothing=1\text{mm}$ , and IED of 5mm or 200 samples/m).

To define an optimal IED, we evaluate the spatial bandwidth of the sEMG in Chapter VI. Two definitions of sEMG spatial bandwidth are presented. Later on in Chapter VII, the error of the RMS value caused by different IED is investigated.

### *Part 3. Elbow joint angle and force: effect of the recorded EMG*

The third section (Chapter VIII) is focused on the study of the sEMG recorded from biceps brachii and brachioradialis. The aim of these studies is to demonstrate the behavior of the two superficial elbow flexor muscles due to different joint elbow angles and contraction levels through the analysis of EMG signals.

## **Main results and future perspectives**

### *Part 1. EMG signal processing: Methodological issues*

The results of the studies reported in Chapters II, and III showed that different methods of processing the sEMG signals might change the output results and that these changes could be crucial. As shown in Chapter II, the use of the Notch filter to attenuate the power line interference will change the shape of the signal since it removes the frequency component of the power line as well as the sEMG. The study reported in Chapter III showed that the choice of the digital low pass filter properties should be selected carefully based on the application and the consideration of the trade off.

The recorded sEMG is also affected by the thickness of the subcutaneous layer. The finding in Chapter IV shows that the RMS values decrease as subcutaneous layer thickness increases.

*Part 2. High density detection systems: evaluating optimal configuration*

A guideline for a 2D detection systems is not yet established. Therefore, the purpose of Chapters V, VI, and VII in this thesis is to figure out the optimal configuration of a 2D detection systems (e.g. a grid of electrodes). The analysis of the sEMG signals recorded from biceps brachii using a grid of electrodes (16x8,  $\varnothing=1\text{mm}$ , and IED of 5mm or 200 samples/m) demonstrates that the error of a sEMG map power and RMS are increased along with a greater diameter of the electrodes and a larger IED.

In addition, two definitions of spatial sEMG bandwidth are proposed in Chapter VI to investigate the optimal IED that satisfies the Nyquist-Shannon theorem. Based on the threshold of 95% power, the sEMG spatial bandwidth in 90% of the cases lies between 25.0-87.5 cycle/m. On the other hand, the sEMG spatial bandwidth in 90% of the cases lies between 9.4 – 59.4 cycle/m based on the threshold of the amplitude of spectral line (>5% of the spectral peak).

*Part 3. Elbow joint angle and force: effect of the recorded EMG*

The analysis of the effect of the elbow joint angle and the force level indicated that the sEMG increases along with a higher force level but might not be affected by the elbow joint angle (Chapter VIII). Furthermore, the EMG amplitude depends on the strategy of the muscle contribution as some subjects show similar activity among both heads of the biceps brachii while other subjects show higher activity on the short head of biceps brachii. However, there is no general pattern of this activation.

Future studies will be aimed to confirm recent preliminary evidence about the spatial sEMG bandwidth especially on the effect of windowing (size of the grid of electrodes). The present work can be further extended to investigate on the effect of joint angle and force to the sEMG of elbow flexor muscles in dynamic condition.

## REFERENCES

- [1] L. A. Pederzini, D. Eyendaal, and M. Denti, *Elbow and Sport*. Springer, 2016.
- [2] B. F. Morrey, L. J. Askew, and E. Y. Chao, "A biomechanical study of normal functional elbow motion.," *J. Bone Joint Surg. Am.*, vol. 63, no. 6, pp. 872–877, 1981.
- [3] A. A. Amis, D. Dowson, and V. Wright, "Muscle strengths and musculo- skeletal geometry of the upper limb," *Arch. Eng. Med. 1971-1988 (vols 1-17)*, vol. 8, no. 1, pp. 41–48, 1979.
- [4] W. M. Murray, S. L. Delp, and T. S. Buchanan, "Variation of muscle moment arms with elbow and forearm position," *J. Biomech.*, vol. 28, no. 5, pp. 513–525, May 1995.
- [5] P. Pigeon, L. Yahia, and A. G. Feldman, "Moment arms and lengths of human upper limb muscles as functions of joint angles," *J. Biomech.*, vol. 29, no. 10, pp. 1365–1370, 1996.
- [6] W. M. Murray, T. S. Buchanan, and S. L. Delp, "Scaling of peak moment arms of elbow muscles with upper extremity bone dimensions," *J. Biomech.*, vol. 35, no. 1, pp. 19–26, Jan. 2002.
- [7] F. H. Netter, *Atlas of human anatomy*. Elsevier Health Sciences, 2010.
- [8] B. M. Van Bolhuis and C. C. A. M. Gielen, "The relative activation of elbow-flexor muscles in isometric flexion and in flexion/extension movements," *J. Biomech.*, vol. 30, no. 8, pp. 803–811, 1997.
- [9] E. P. Doheny, M. M. Lowery, D. P. FitzPatrick, and M. J. O'Malley, "Effect of elbow joint angle on force-EMG relationships in human elbow flexor and extensor muscles," *J. Electromyogr. Kinesiol.*, vol. 18, no. 5, pp. 760–770, 2008.
- [10] J. H. Lawrence and C. J. De Luca, "Myoelectric signal versus force relationship in different human muscles.," *J. Appl. Physiol.*, vol. 54, no. 6, pp. 1653–1659, 1983.
- [11] H. Onishi, R. Yagi, K. Akasaka, K. Momose, K. Ihashi, and Y. Handa, "Relationship between EMG signals and force in human vastus lateralis muscle using multiple bipolar wire electrodes," *J. Electromyogr. Kinesiol.*, vol. 10, no. 1, pp. 59–67, 2000.
- [12] T. Uchiyama, T. Bessho, and K. Akazawa, "Static torque — angle relation of human elbow joint estimated with artificial neural network technique," vol. 31, pp. 545–554, 1998.
- [13] T. Kleiber, L. Kunz, and C. Disselhorst-Klug, "Muscular coordination of biceps brachii and brachioradialis in elbow flexion with respect to hand position," *Front. Physiol.*, vol. 6, no. Aug, pp. 1–5, 2015.
- [14] S. C. F. A. von Werder and C. Disselhorst-Klug, "The role of biceps brachii and brachioradialis for the control of elbow flexion and extension movements," *J. Electromyogr. Kinesiol.*, vol. 28, pp. 67–75, 2016.
- [15] H. J. Hermens, B. Freriks, C. Disselhorst-Klug, and G. Rau, "Development of recommendations for SEMG sensors and sensor placement procedures," *J. Electromyogr. Kinesiol.*, vol. 10, no. 5, pp. 361–374, Oct. 2000.
- [16] S. Martin and D. MacIsaac, "Innervation zone shift with changes in joint angle in the brachial biceps," *J. Electromyogr. Kinesiol.*, vol. 16, no. 2, pp. 144–148, Apr. 2006.

- [17] D. Farina, R. Merletti, M. Nazzaro, and I. Caruso, "Effect of joint angle on EMG variables in leg and thigh muscles," *Eng. Med. Biol. Mag. IEEE*, vol. 20, no. 6, pp. 62–71, 2001.
- [18] A. Rainoldi, G. Melchiorri, and I. Caruso, "A method for positioning electrodes during surface EMG recordings in lower limb muscles," *J. Neurosci. Methods*, vol. 134, no. 1, pp. 37–43, 2004.
- [19] M. Barbero, R. Merletti, and A. Rainoldi, *Atlas of muscle innervation zones: understanding surface electromyography and its applications*. Springer Science & Business Media, 2012.
- [20] R. Merletti, D. Farina, and M. Gazzoni, "The linear electrode array: A useful tool with many applications," *J. Electromyogr. Kinesiol.*, vol. 13, no. 1, pp. 37–47, 2003.
- [21] R. Merletti and P. A. Parker, *Electromyography: physiology, engineering, and non-invasive applications*, vol. 11. John Wiley & Sons, 2004.
- [22] E. A. Clancy, E. L. Morin, and R. Merletti, "Sampling, noise-reduction and amplitude estimation issues in surface electromyography," *J. Electromyogr. Kinesiol.*, vol. 12, no. 1, pp. 1–16, 2002.



# Chapter II

*Power Line Interference  
attenuation in multi-  
channel sEMG signals:  
algorithms and analysis*





## Power Line Interference Attenuation in Multi-channel sEMG signals: Algorithms and Analysis

S. D. H. Soedirdjo, K. Ullah, and R. Merletti, "Power Line Interference Attenuation in Multi-channel sEMG signals : Algorithms and Analysis," in *37th Annual International Conference of the IEEE Engineering in Medicine and Biology Society (EMBC), 2015, vol. 2, pp. 3823–3826.*

### Abstract

Electromyogram (EMG) recordings are often corrupted by power line interference (PLI) even though the skin is prepared and well-designed instruments are used. This study focuses on the analysis of some of the recent and classical existing digital signal processing approaches that have been used to attenuate, if not eliminate, the power line interference from EMG signals. A comparison of the signal to interference ratio (SIR) of the output signals is presented for four methods: 1) classical notch filter; 2) spectral interpolation; 3) adaptive noise canceller with phase locked loop (ANC-PLL); and 4) adaptive filter, applied to simulated multichannel monopolar EMG signals with different SIR. The effect of each method on the shape of the EMG signals is also analyzed. The results show that ANC-PLL method gives the best output SIR and lowest shape distortion compared to the other methods. Classical notch filtering is the simplest method but some information might be lost as it removes both the interference and the EMG signals. Thus, it is obvious that notch filter has the lowest performance and it introduces distortion into the resulting signals.

### Introduction

Electrical activity of the muscle can be measured from the skin surface over the muscle through surface electrodes in either monopolar or bipolar form. Several algorithms can be applied to the electromyogram (EMG) recordings to obtain muscle physiological and anatomical information. Most of these algorithms assume that the recorded EMG has an adequate quality, i.e. high signal to interference ratio (SIR). Even with good skin preparation and the use of well-designed instrumentation, various noises and interferences still affect the recorded EMG signals in practical conditions. One of these interferences is power line interference (PLI).

A power line that provides power to measurement devices also produces an electromagnetic field which may couple with a biopotential measurement system [1]. The fundamental frequency of these fields is 60 Hz in North America or 50 Hz in Europe and its harmonics. Improvement of the instrument by utilizing some hardware methods such as active electrodes, driven-right-leg circuit, virtual ground circuit, electrode-skin impedance equalization, and guarding systems has been proposed to reduce PLI but the interference may still be present in the

recorded signals due to limitations of the hardware. Thus to attenuate this interference digital signal processing (DSP) methods need to be used [2].

A number of digital signal processing techniques are available for reducing the PLI from EMG signals. Each method has its own limitations and complexities. In this study, some classical and recent methods like 1) notch filter, 2) spectral interpolation, 3) adaptive noise canceller with phase locked loop (ANC-PLL) and 4) adaptive filtering are analyzed. Notch filter is the simplest and most straightforward method that directly eliminates the frequency component of the interference with a disadvantage of removal of the same frequency component of EMG signal. Spectral interpolation interpolates the frequency component of the interference to the neighbor frequency components thus preserving the signal component while failing to maintain the signal's form due to domain conversions (from time to frequency domain and its inverse process) and interpolation. On the other hand, the adaptive noise canceller with PLL and the common adaptive filters first estimate the frequency of the PLI and its harmonics, their amplitudes and phases and then remove the PLI while maintaining the information of the recorded EMG signal [3].

Then we evaluate the performances of the above mentioned four methods using two criteria: 1) the SIR of resulting output signals and 2) their correlation coefficient with the original simulated signal. Our results indicate that for contaminated input simulated signals with 24 dB of SIR, the output SIR of the adaptive noise canceller with phase locked loop is higher (32 dB) than the other three methods (13 dB with notch filter, 7 dB with spectral interpolation, and 18 dB with common adaptive filter). The output of the ANC-PLL is also highly correlated with the original simulated signals, which means that this method has least distortion on the shape of EMG signals.

## Materials and methods

*Generation of the simulated signals.* Eighty one sets of 16 channels monopolar EMG signals were generated based on the planar model [4]. The signals are generated for 10 seconds with sampling frequency of 2048 Hz (Figure 1a). The PLI is modeled as a periodic signal with constant frequency and amplitude. Then seven sets of test signals with different SIR (24dB, 15 dB, 10dB, 4dB, -10dB, -16dB, -22dB) are obtained by adding the interference to each channel of the simulated EMG signals as can be expressed mathematically as

$$X_n(t) = S_n(t) + I_n(t) \quad (1)$$

$$I_n(t) = A \sum_{h=1}^H \sin(2\pi h f t) \quad (2)$$

where in every channel  $n$ ,  $X_n(t)$  is the contaminated EMG signal,  $S_n(t)$  is the simulated signal and  $I_n(t)$  is the PLI interference with amplitude  $A$ , frequency  $f$

and its harmonics  $h$ . For simplicity, the phase shift was set to zero and only the first three harmonics were chosen ( $H=3$ ).

In absence of EMG, the PLI appears at each channel as non-propagating biphasic signals (Figure 1b). The effect of PLI to the EMG signals can be seen clearly in frequency domain, i.e. the discontinuity of the shape of signal's spectrum (Figure 1c).

Each of the 16 channels contaminated monopolar EMG signals was passed through each of the DSP technique described in following section, resulting in 4 sets of 16-channels cleaned signals  $C_n(t)$ . The remaining interference  $R_n(t)$  of each channel is obtained by subtracting the simulated EMG  $S_n(t)$  from the cleaned signals  $C_n(t)$ .

$$R_n(t) = C_n(t) - S_n(t) \quad (3)$$

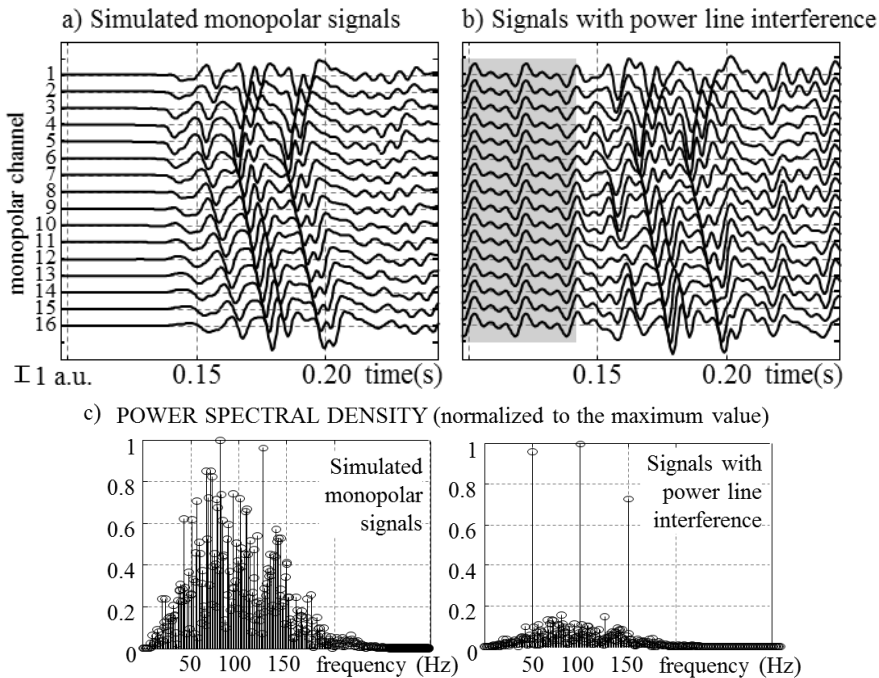


Figure 1. (a) An example of 16-channels monopolar simulated EMG signals with innervation zone under channel 5. (b) Power line interference (PLI), added to the simulated signals in (a). The PLI is assumed to have equal magnitude for every channel with fundamental frequency at 50 Hz and harmonics at 100 and 150 Hz. The PLI appear as non-propagating signals as shown in the darker area. (c) In frequency domain, the PLI appears as peaks whose magnitude depends on severeness of the interference.

*Four methods to attenuate PLI.* The four methods used for PLI removal (notch filter, spectral interpolation, adaptive filtering, and adaptive noise canceller with phase locked loop) analyzed in this study are discussed in details in the following.

#### A. Notch filter

Fixed narrow band notch filter is the simplest method for removing narrow bandwidth interference from the EMG signals. The mathematical expression for an IIR notch filter's transfer function is shown below.

$$H(z) = b_0 \frac{1 - 2\cos\omega_0 z^{-1} + z^{-2}}{1 - 2r\cos\omega_0 z^{-1} + r^2 z^{-2}} \quad (4)$$

where  $\omega_0$  is the central angular frequency of the interference and the width of the notch at -3dB is  $2(1-r)$ rad/s. Q-factor of the filter is defined as follows.

$$Q = \frac{f_c}{\Delta f} \quad (5)$$

where  $f_c$  is the central of the spectrum line which would like to be removed and  $\Delta f$  is the width of the notch filter, i.e. the distance between the lowest and highest frequencies of the -3dB points. In this study, the 2Hz of  $\Delta f$  is selected.

Since the power line fundamental frequency and its harmonics are located within the bandwidth of EMG (20-500Hz) notch filter removes PLI as well as the component of the EMG signals at that frequency. Therefore the filter distorts the signal [2], [5]. A notch filter with a narrow band and high Q-factor is used to minimize the distortion.

#### B. Spectral interpolation

This method deals with the PLI by interpolating the signal component at PLI in the frequency domain. The general idea of amplitude and phase spectral interpolation is elimination of PLI spectral lines and replacing these with the interpolated value of their neighbors. Then the inverse Fourier transform is performed to get the EMG signals with reduced interference in time domain.

The assumption used in this technique is that the 'true' amplitude spectrum of the corrupted EMG signal is supposed to be a continuous curve with a superimposed peak at the power line frequency. With this method, the information of the signals superimposed by PLI are still conserved but with the drawback of the signals' distortion and sensitivity to spectral leakage and selection of window length [6].

#### C. Adaptive filtering

Various adaptive filters are being used for reducing the PLI in biomedical signals. One of the recent works proposed in [3] uses a recursive algorithm to first estimate the frequency of the PLI and then generate the other

harmonics of the PLI. Amplitude and phase of the PLI and its harmonics are then approximated using the recursive least square algorithm. Then the estimated PLI are subtracted from the corrupted EMG signal to reduce PLI.

D. Adaptive noise canceller with phase locked loop (ANC-PLL)

An adaptive noise canceller (ANC) to remove the PLI from biopotential signals was first proposed in [7]. The original method uses a synthetic reference signal, i.e. sinusoidal signal with constant fundamental frequency of the interference. This approach might not be sufficient since the fundamental frequency of PLI deviates up to  $\pm 1\%$  from its nominal frequency. To counteract the PLI's deviation, a synthetic reference with varying frequency and phase is proposed in [8]. Phase Locked Loop was used to track the fundamental frequency and phase of the PLI. Based on this information, a synthetic signal reference was generated as an input of the ANC that uses Least Mean Squares (LMS) to optimize the weights of input signals. This method works with multichannel signals, i.e. taking information of the interference at the other channels such as to allow PLI reduction in all channels in real time.

*Criteria of performances.* The four methods discussed above are applied to seven simulated multichannel monopolar EMG signals (of 3 seconds length) with different magnitude of PLI. The criteria used for the performance analysis of each method are SIR and shape distortion of the output signals. For simplicity, we assume that the magnitude of PLI is the same for all the channels, the fundamental frequency of PLI is not changing in time (fixed at 50 Hz), and only its first three harmonics of the same amplitude are considered. The performance of the four methods was evaluated using the signal to interference ratio (SIR) of the output signals and their correlation coefficient with the original simulated signals.

A. Signal to Interference Ratio (SIR)

SIR values computed for every channel  $n$ , are defined as the ratio of the power of simulated signal ( $P_{S,n}$ ) to the power of the remaining interference ( $P_{R,n}$ ). Global SIR ( $SIR_G$ ) for each method is then computed by taking the average across the total number of channel  $N$ .

$$SIR_G = \frac{1}{N} \sum_{n=1}^N 10 \log_{10} \left( \frac{P_{S,n}}{P_{R,n}} \right) = \frac{1}{N} \sum_{n=1}^N 10 \log_{10} \left( \frac{\frac{1}{T} \sum_{t=1}^T S_n(t)^2}{\frac{1}{T} \sum_{t=1}^T R_n(t)^2} \right) \quad (6)$$

B. Correlation coefficient

The Pearson's correlation coefficient is computed for each pair of corresponding channels ( $\rho_{S_n, C_n}$ ) of the output signals with the original

simulated signals after removal of the mean and averaged across the channels to obtain a global value  $\rho_G$  as expressed mathematically in (7).

$$\rho_G = \frac{1}{N} \sum_{n=1}^N (\rho_{S_n, C_n}) = \frac{1}{N} \sum_{n=1}^N \frac{E[S_n C_n]}{\sigma_{S_n} \sigma_{C_n}} \quad (7)$$

where  $\sigma_{S_n}$  and  $\sigma_{C_n}$  are the standard deviation of each channel  $n$  of simulated signal and  $E[\bullet]$  is the expected value of  $S_n$  and  $C_n$ . The value of the correlation coefficient (ranged from 0 to 1) shows the shape similarity of the cleaned signals and the original simulated signals. A higher correlation coefficient means lower signal's shape distortion.

## Results and discussion

Each of the four methods discussed before, has its own advantages and tradeoffs that are presented and discussed in this section.

*Notch filter:* The classical notch filter eliminates the spectral lines of selected frequency components and reduces the power of the nearby frequencies. Sufficient attenuation of the intended frequency for highly interfered signals can be obtained by adjusting the configuration of the notch filter, i.e. increasing the width of the bandstop. However, wider bandstop results in more information removal from the signal. Another disadvantage of notch filter is a great distortion of signal's shape. In line with the results presented in Figure 5, the output of the Notch filter has the lowest quality of signal's shape (lowest coefficient of correlation). The reason of the shape distortion is the fact that the filter introduces phase alternation to the signal's frequencies components located at certain range (see Figure 2).

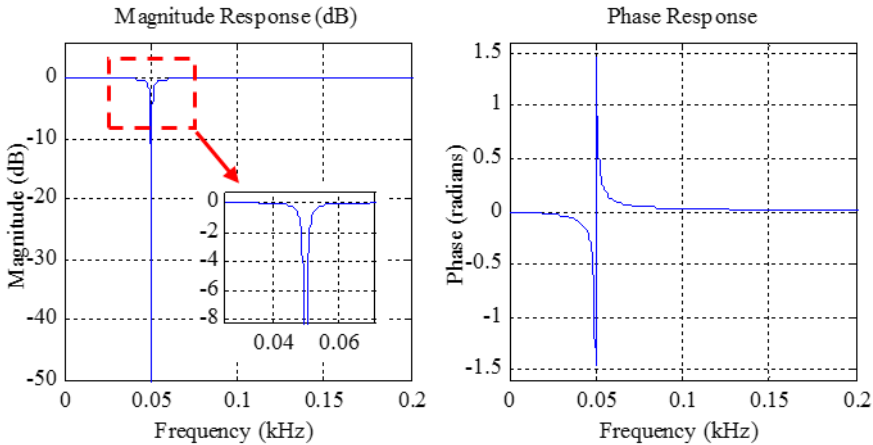


Figure 2. This figure demonstrates the magnitude response and phase response of a Notch filter designed with central frequency  $f_c$  at 50Hz and the width of the -3dB points is 2Hz.

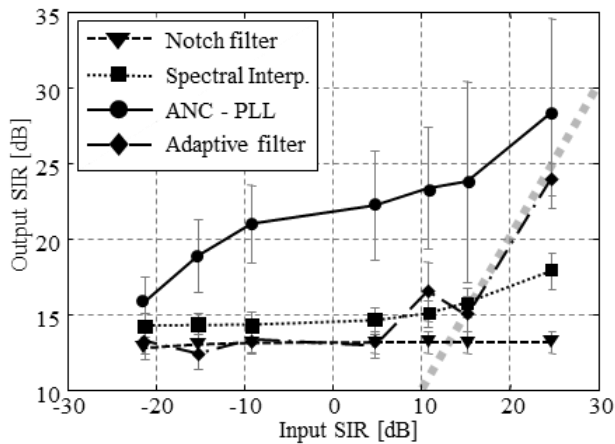


Figure 3. The ANC-PLL gives the best SIR at the output even though the input signals were highly corrupted by the interference (-20 dB). Except for the spectral interpolation method, the output SIR decreases as the magnitude of interference increases. The dashed grey line corresponds to output SIR equal to input SIR. The points that appear below this line imply that the corresponding filter aggravate the output SIR. Bars are  $\pm\sigma$  for 81 sets of simulated 16 channels monopolar EMG signals.

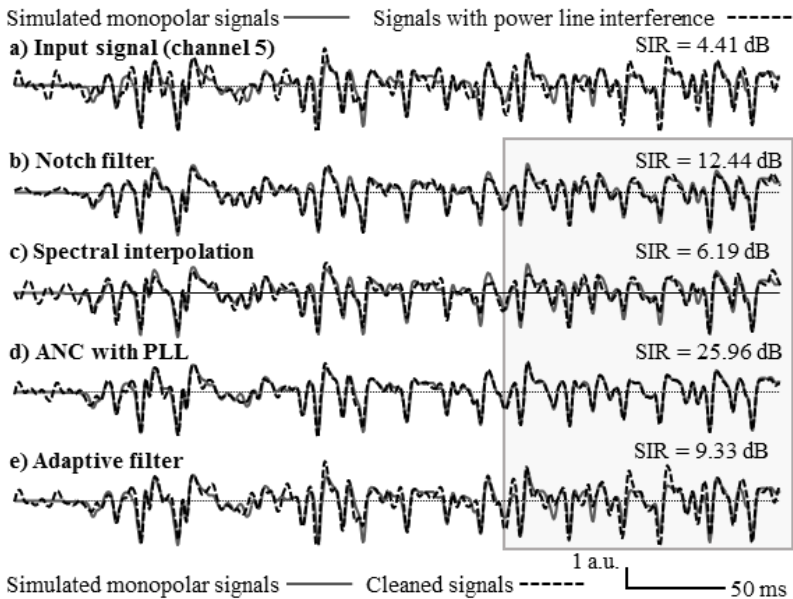


Figure 4. The original and output signal of different techniques to reduce the power line interference (PLI) are shown. (a) Example of one original signal (—) and the contaminated signal (- - -). (b) Original signal and output of the notch filter. (c) Original signal and output of the spectral interpolation. (d) Adaptive noise canceller with phase locked loop (ANC with PLL). (e) Original signal and output of the adaptive filter described in [3].

*Spectral interpolation:* At higher interference, the performance of all the methods degrade except that of spectral interpolation, which results in a constant SIR regardless of the magnitude of the interference (Figure 3). This is obvious since the PLI spectral lines are replaced by the interpolated value of its neighbors, which does not change while interference is being increased. This method might be of advantage compared to the rest of the methods if one works with highly corrupted EMG signals. Furthermore, since the phase of each signal's frequencies components is maintained [5], only slight distortion on the shape of the signal occurs. However, this method can only be applied offline and it is sensitive to the selection of the window length used in interpolation.

*Adaptive filtering:* The adaptive filtering method proposed in [3] has two main limitations:

- 1) It requires a large number of parameters and is very difficult to find the optimal initial values for these parameters; and,
- 2) The frequency of the harmonics of PLI is dependent on accurate estimation of the fundamental frequency of PLI, which sometimes is removed fully by the hardware and thus the harmonic cannot be estimated and removed from the signal.

*Adaptive Noise Canceller with Phase Locked Loop:* The decrease of the output SIR as the interference increases also occurs with ANC-PLL method. This method takes several hundred milliseconds to optimize the coefficients and converge. As shown in Figure 4 the PLI still appears in the first several hundred milliseconds which may be discarded for further processing of the signals and the output signals start to converge at the time marked with the grey square. As the result of phase estimation [8], this method gives the best output SIR and the highest coefficient of correlation which means that the distortion of the signal's shape is negligible.

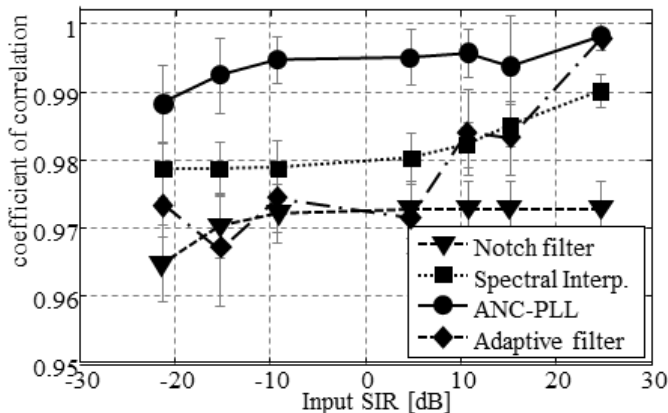


Figure 5. Correlation coefficient, averaged across the channels, between the original simulated signals and the output of each method. Bars are  $\pm\sigma$  for 81 sets of simulated 16 channels monopolar EMG signals.



Although sensitive to the number of channels in the EMG measurement system [7], ANC-PLL gives the highest SIR compared to the notch filtering, spectral interpolation and Keshtkaran and Yang's adaptive filtering methods. Except for spectral interpolation, all methods can be applied for online PLI removal. The results also indicate that the ANC-PLL gives the highest correlation of the output signals with original simulated signals which implies that it has least effect on the shape of the signals (Figure 5).

### **Conclusion**

Four methods used for reducing PLI in EMG signals are compared in this study. For quantitative analysis of their performance, SIR and correlation coefficients were evaluated as performance indexes of each method and the one with the highest output SIR and correlation coefficient is chosen. Simulated signals with various levels of SIR were used to evaluate the performance of each method. The adaptive noise canceller with phase locked loop, although taking several hundred milliseconds for tuning of the parameters to converge, has the best performances in terms of SIR and average correlation coefficient with original signals.

## REFERENCES

- [1] J. Webster, *Medical instrumentation: application and design*. John Wiley & Sons, 2009.
- [2] E. A. Clancy, E. L. Morin, and R. Merletti, "Sampling, noise-reduction and amplitude estimation issues in surface electromyography," *J. Electromyogr. Kinesiol.*, vol. 12, no. 1, pp. 1–16, 2002.
- [3] M. R. Keshtkaran and Z. Yang, "A fast, robust algorithm for power line interference cancellation in neural recording.," *J. Neural Eng.*, vol. 11, no. 2, p. 026017, 2014.
- [4] D. Farina and R. Merletti, "A novel approach for precise simulation of the EMG signal detected by surface electrodes," *Biomed. Eng. IEEE Trans.*, vol. 48, no. 6, pp. 637–646, 2001.
- [5] D. T. Mewett, H. Nazeran, and K. J. Reynolds, "Removing Power Line Noise From Recorded EMG," in *Proceedings of the 23rd Annual EMBS International Conference*, 2001, pp. 2190–2193.
- [6] D. T. Mewett, K. J. Reynolds, and H. Nazeran, "Reducing power line interference in digitised electromyogram recordings by spectrum interpolation," *Med. Biol. Eng. Comput.*, vol. 42, pp. 524–531, 2004.
- [7] B. Widrow, J. R. Glover Jr., J. M. McCool, J. Kaunitz, C. S. Williams, R. H. Hearn, J. R. Zeidler, J. Eugene Dong, and R. C. Goodlin, "Adaptive noise cancelling: Principles and applications," in *Proceedings of the IEEE*, 1975, vol. 63, no. 12, pp. 1692–1716.
- [8] L. Mesin, A. Boye, A. Troiano, R. Merletti, and D. Farina, "Real-time Reduction of Power Line Interference in Multi-channel Surface EMG," in *ISEK (International Society of Electrophysiology and Kinesiology)*, 2008, pp. 1 – 2.

# **Chapter III**

## *Extracting surface EMG envelope*



## Extracting surface EMG envelope

Adapted from:

Soedirdjo S.D.H., Merletti R. *Comparison of different digital filtering techniques for surface EMG envelope recorded from skeletal muscle. "XX Congress of The International Society of Electrophysiology and Kinesiology", Rome, Italy, July 15-18, 2014*

### Abstract

The choice of filter parameters that would provide the “best” estimate of EMG envelopes is an open issue. This study investigates the most appropriate mono- or bi-directional low pass filters (LPF) for extracting the EMG envelope. Four different filter types (Butterworth, Chebyshev, Inverse Chebyshev, and Elliptic) were considered. Four cut off frequencies (1 Hz, 3 Hz, 5 Hz, and 10 Hz), five filter orders (1<sup>st</sup> to 5<sup>th</sup> for each direction), and two configurations (mono-directional/MD or bi-directional/BD) were tested with 100 simulated interference EMG signals. These filters were evaluated through: rise time, time delay, computation time and average of relative root mean square error (RMSE) between the true calculated average rectified value (ARV) of the input and the ARV of each output signal. The results suggest that the selection of the filter has a distinctive trade-off for specific application. The globally best filter is the 2<sup>nd</sup> order Butterworth LPF with 5 Hz cut off frequency.

### Introduction

The amplitude of sEMG can be estimated through several methods: 1) low pass filtering of the rectified EMG signal, 2) moving average, and 3) adaptive algorithm [1], [2]. This study will investigate the first method, i.e. extracting the sEMG envelope using low pass filtering of the rectified EMG signal. Low pass filter has been considered as the simplest method. It is widely used with a great variety of filter configurations. An ideal low pass filter is the filter whose delay, root means square error (RMSE), and rise time are zero. Since different filter configurations have their own characteristics, it is interesting to find out which filter's configuration has characteristics closest to the ideal filter.

### Materials and methods

*Generation of the simulated signals.* One hundred EMG signals (9 s length each) were generated using white noise passed through a Shwedyk filter [3] and sampled at 2048 Hz. The Shwedyk filter is a shaping filter so that, by the given input of white Gaussian noise, the spectral shape of the output signal will be

similar to those of the EMG. The power spectrum of the Shwedyk filter is written as follows

$$H(f) = \frac{k f_h^4 f^2}{(f^2 + f_l^2)(f^2 + f_h^2)^2} \quad (1)$$

where  $k$  is gain,  $f_l$  is the lower frequency parameter in Hertz;  $f_h$  is the upper frequency parameter in Hertz. In this study the values of  $f_l$  and  $f_h$  are set to 40 Hz and 80 Hz respectively. Each signal was multiplied with a 3 s gate function such that we obtain a 3 s burst of simulated EMG signal (see Figure 1). Then we normalize each of the signals to its average rectified value (ARV). These signals were processed using MATLAB for Macintosh installed on a PC with 4 GB of RAM.

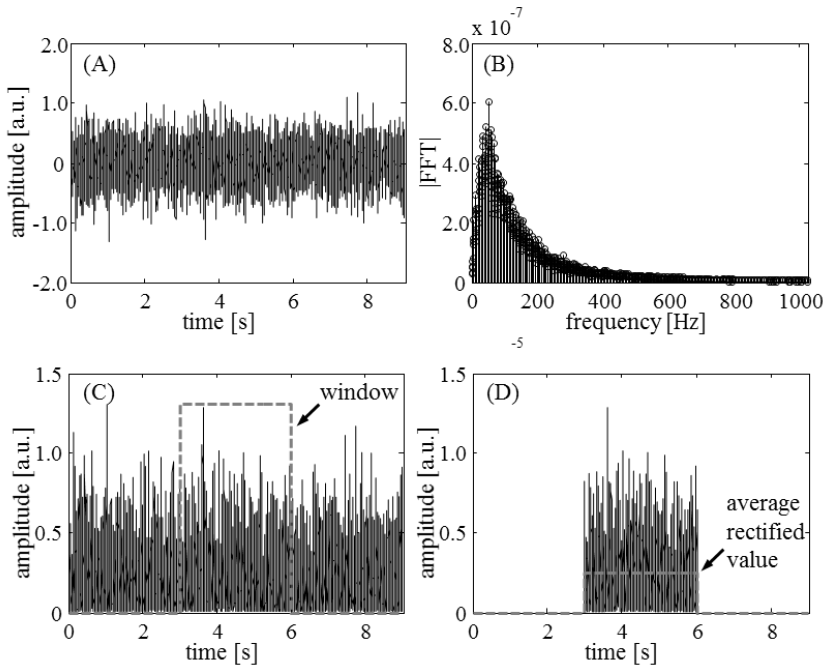


Figure 1. (A) An example of interference EMG signal generated by applying Shwedyk filter on white Gaussian noise. (B) The spectrum of the signal shown in panel A. (C) The signal was rectified and modulated with a 3s windows resulting a burst of signal (D). Then the signal is normalized to its average rectified value (ARV).

*Four IIR digital low pass filters.* A detailed explanation of digital low pass filters can be found easily in many writings. Some of them are mentioned in the references [4], [5]. The following section provides a brief explanation of each filter (see Figure 2).

## A. Butterworth

Butterworth filters are designed to have an amplitude response characteristic as flat as possible at pass-band and monotonically decreasing at stop band. The amplitude response will decrease at a frequency greater than the defined corner frequency as specified:

$$G^2(\omega) = \frac{1}{1 + (\omega/\omega_c)^{2n}} \quad (2)$$

where  $G(\omega)$  represents the magnitude response,  $n$  represents the order of the filter and  $\omega_c$  represents the cut off frequency.

## B. Chebyshev

The Chebyshev filter has a faster gain transition from pass-band to the stop-band (steeper roll-off) compared to the Butterworth filter but has a ripple in the pass-band. Mathematically, characteristic of the filter can be written as:

$$G^2(\omega) = \frac{1}{1 + \varepsilon^2 T_n^2(\omega_n)} \quad (3)$$

where  $G(\omega)$  represents the magnitude response,  $T_n(\omega_n)$  is a Chebyshev polynomial of the order  $n$ ,  $\omega_n$  is the frequency normalized to the edge of pass-band frequency, and  $\varepsilon$  is a ripple factor defined as a function of the desired pass-band peak-to-peak attenuation  $A_p$

$$\varepsilon^2 = 10^{0.1A_p} - 1 \quad (4)$$

The cut off frequency of this filter usually refers to the edge of the pass band frequency instead of the frequency where the power is attenuated by 50% (-3dB point). Thus to obtain an exact frequency of the -3dB point ( $\omega_{\text{desired}}$ ), we can adjust the cut off frequency ( $\omega_{\text{cut-off}}$ ) as follows:

$$\frac{\omega_{\text{desired}}}{\omega_{\text{cut-off}}} = \cosh\left(\frac{\cosh^{-1}(1/\varepsilon)}{n}\right) \quad (5)$$

## C. Inverse Chebyshev

The Inverse Chebyshev (or Chebyshev type II) has an inverse characteristic of the Chebyshev filter. While Chebyshev type I shows a ripple in the pass-band and monotonically amplitude decrease in the stop-band, the Inverse Chebyshev has a flat response in the pass-band as in the Butterworth filter, yet it gives a ripple in the stop-band. The magnitude of this filter is:

$$G^2(\omega) = \frac{1}{1 + \varepsilon^2 T_n^2(1/\omega_n)} \quad (6)$$

where  $G(\omega)$  represents the magnitude response,  $T_n(1/\omega_n)$  is a Chebyshev polynomial of the order  $n$ ,  $\omega_n$  is the frequency normalized to the edge of pass-band frequency, and  $\epsilon$  is ripple factor calculated from the minimal attenuation of the ripple in stop-band  $A_a$  and defined as:

$$\epsilon^2 = 1 / (10^{0.1A_a} - 1) \tag{7}$$

Similar to the Chebyshev filter, the cut off frequency of this filter refers to the edge of the stop-band frequency, i.e., the frequency at which the attenuation of the frequency component is  $A_a$ . Thus, to obtain an exact frequency of the -3dB point ( $\omega_{\text{desired}}$ ) we can adjust the cut off frequency ( $\omega_{\text{cut-off}}$ ) as follows:

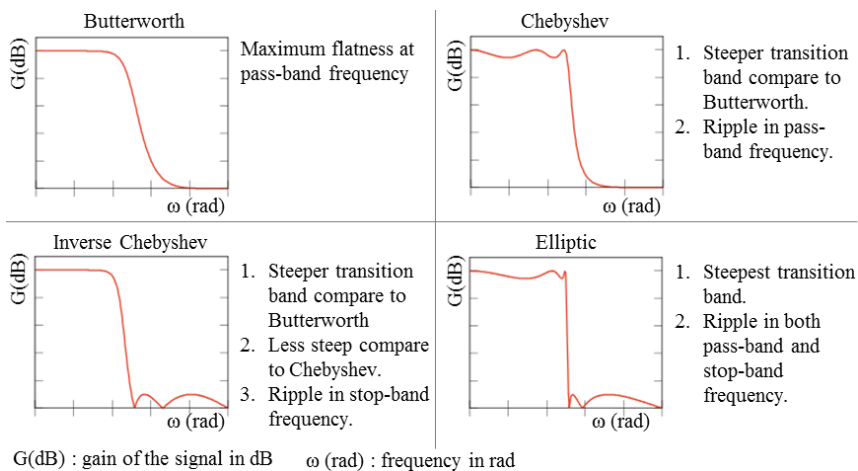
$$\frac{\omega_{\text{cut-off}}}{\omega_{\text{desired}}} = \cosh \left( \frac{\cosh^{-1} \left( \sqrt{1/\epsilon^2 (\sqrt{2}-1)} \right)}{n} \right) \tag{8}$$

D. Elliptic

The Elliptic filter has the steepest gain transition of these four filters but with a trade off ripple in both pass-band and stop-band. The magnitude of the filter is mathematically expressed as:

$$G^2(\omega) = \frac{1}{1 + \epsilon^2 R_n^2(\xi, \omega_n)} \tag{9}$$

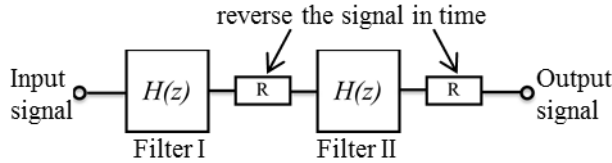
where  $G(\omega)$  represents the magnitude response as function of Jacobian Elliptic rational function  $R_n(\xi, \omega_n)$  and the ripple factor  $\epsilon$  calculated as in (4).



G(dB) : gain of the signal in dB    ω (rad) : frequency in rad  
 Figure 2. Each type of the filter has its own characteristic which is summarized in this figure.



*Zero phase filter or bi-directional filtering.* All of the causal filters introduce time delay to the output signal. In the case of digital applications, this time delay can be eliminated using a configuration called zero phase filter or bi-directional filter. A zero phase filter comprised of two identical filters  $H(z)$  and two blocks for reversing the signal's sequence (see Figure 3).



$H(z)$  : transfer function of the filter

Figure 3. A zero phase filter comprised of two identical filters  $H(z)$  and two blocks  $R$  to reverse the sequence of the signal. The output of the signal has zero delay since the second filter eliminates the delay caused by the first filter.

Filter I introduces a certain delay depending on the frequency. The second filter (Filter II) introduces exactly the same delay as the first, yet, due to the signal being fed backward, the delay is actually a time advance and therefore, cancels the delay caused by the first filter [4].

The advantage of using zero phase filters is that the filter will not introduce delay to the signal output. However, with the signal passing through two filters, the attenuation of the signal is doubled as demonstrated below.

$$H_{\text{zero-phase}}(e^{j\omega T}) = H(e^{j\omega T})H(e^{-j\omega T}) = |H(e^{j\omega T})|^2 \quad (10)$$

At the cut off frequency, the magnitude of each filter  $H(e^{j\omega T})$  is 0.707 or -3dB such that for the zero phase filter the value becomes:

$$H_{\text{zero-phase}}(e^{j\omega T}) = |H(e^{j\omega T})|^2 = 0.5 = -6\text{dB} \quad (11)$$

Therefore, adjustment of the cut off frequency is needed to obtain the desired attenuation.

*Criteria of performances.* The four low pass filters mentioned above are varied with four cut-off frequencies (1Hz, 3Hz, 5Hz, and 10Hz), five filter orders (from 1<sup>st</sup> order to 5<sup>th</sup> order for each direction), and two configurations (mono-direction filtering or bi-directional filtering). The total number of filters is 160. We apply each of these filters to 100 simulated sEMG signals (see section “Generation of the simulated signals”) and evaluate their performances based on four criteria:

- A. Relative root mean square error (RMSE)  
The RMSE is computed between the envelopes obtained from each filter and the corresponding average rectified value (ARV) of the input signals.
- B. Rise time  
Rise time is defined as the time required to go from 10% to 90% of the final value of the envelope
- C. Time delay  
The time delay of each filter is defined as the delay of the peak of cross correlation between the input signal and the filter output.
- D. Computational time  
Computation time depends on the specifications of the processor used to perform the filtering and the other running programs at the same time as the computation.

### Results and discussion

The performances of the mentioned low pass filters with different cut off frequencies, filter order, and mode of filtering (one directional or zero phase) are compared to select the most appropriate filters to obtain the sEMG envelope.

*Time delay.* The time delay of filters with bi-directional configuration is zero since the second filter cancels the delay introduced by the first filter (see **Materials and methods**). Filters with mono-directional configuration show greater time delay along with the higher filter order. However, these delays decrease as we shift the cut-off frequency to the higher frequency (see Figure 4).

*Relative root mean square error.* The average of relative RMSE values of mono directional filters is higher than that of the bi-directional configurations (see Figure 5). Some remarks for each filter's order with mono-directional configuration are listed below:

- The 1<sup>st</sup> order filter. The lowest averages of relative RMSE value can be obtained by setting the cut off frequency to 3 Hz except for Elliptic filters (1 Hz).
- The 2<sup>nd</sup> order filter. The lowest averages of relative RMSE value can be obtained by setting the cut off frequency to 5 Hz except for Elliptic filters (3 Hz).
- The 3<sup>rd</sup> order filter. The lowest averages of relative RMSE value can be obtained by setting the cut off frequency to 5 Hz except for Chebyshev filters (10 Hz).
- The 4<sup>th</sup> and 5<sup>th</sup> order filters. The lowest averages of relative RMSE value can be obtained by setting the cut off frequency to 10 Hz except for Inverse Chebyshev and Elliptic filters (5 Hz).

To obtain the lowest averages of relative RMSE for filters with bi-directional configuration, the cut off frequency needs to be set to 3Hz regardless of the order except for the 1<sup>st</sup> order zero phase Elliptic low pass filter (1 Hz).

*Rise time.* The rise time of the signal's envelope obtained from mono directional filters is similar to that obtained by the filters with bi-directional configuration (see Figure 6). The results show that a higher cut off frequency implies a shorter rise time and the higher filter's order caused longer rise time. In consequence, lower filter order with higher cut off frequency should be preferred for minimizing rise time. Rise time of the filter's output is important for the application that needs fast response such as controlling an actuator.

*Computation time.* Computation time depends on the specifications of a processor applied to perform the filtering and the other programs running at the same time as the computation. Computation time also depends on sampling the frequency of the signal since sampling frequency determines the number of samples taken into process. In general, zero phase filters require more time to filter the signal (see Figure 7). This is obvious since the signal is passed through two filters.

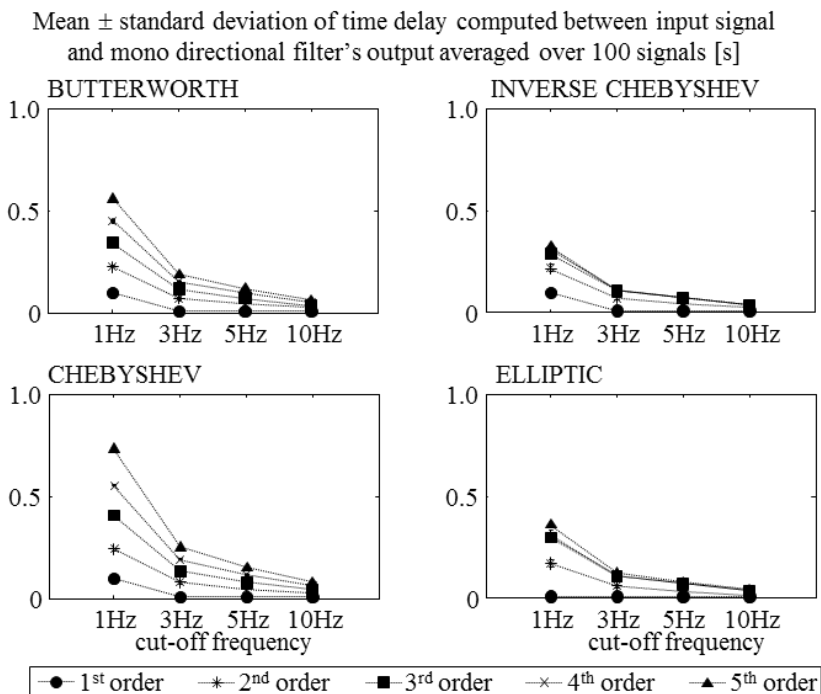


Figure 4. Delay of the signal's envelope only occurs when a low pass filter with mono-directional configuration is used. A higher filter order implies longer delay. However, these delays decrease as we shift the cut off frequency to the higher value.

Mean  $\pm$  standard deviation of relative RMSE between signal's envelope obtained by each filter and the ARV of the input signal, averaged over 100 signals. [%]

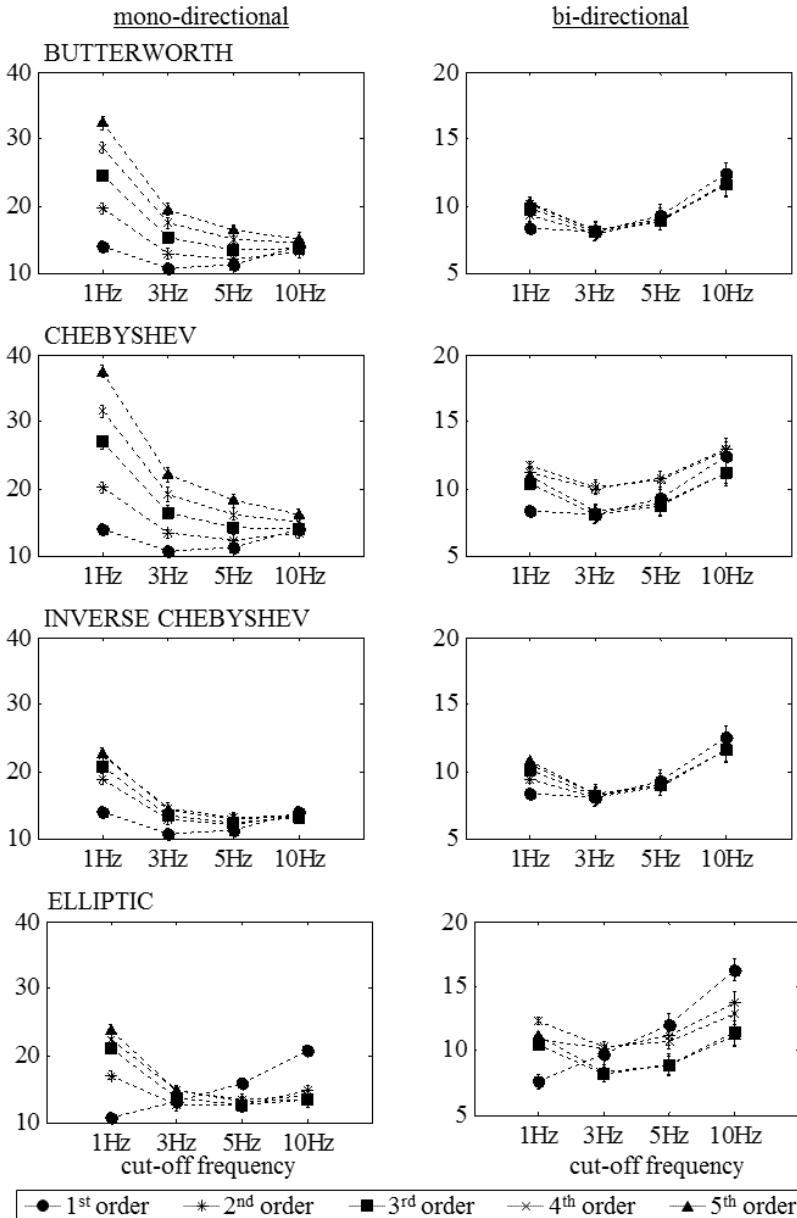


Figure 5. Relative RMSE between the signal's envelope, obtained by a low pass filter with bi-directional configuration and the ARV of the input signal, is lower than those obtained with mono-directional configuration.

Mean  $\pm$  standard deviation of signal's envelopes rise time obtained by each filter, averaged over 100 signals [s]

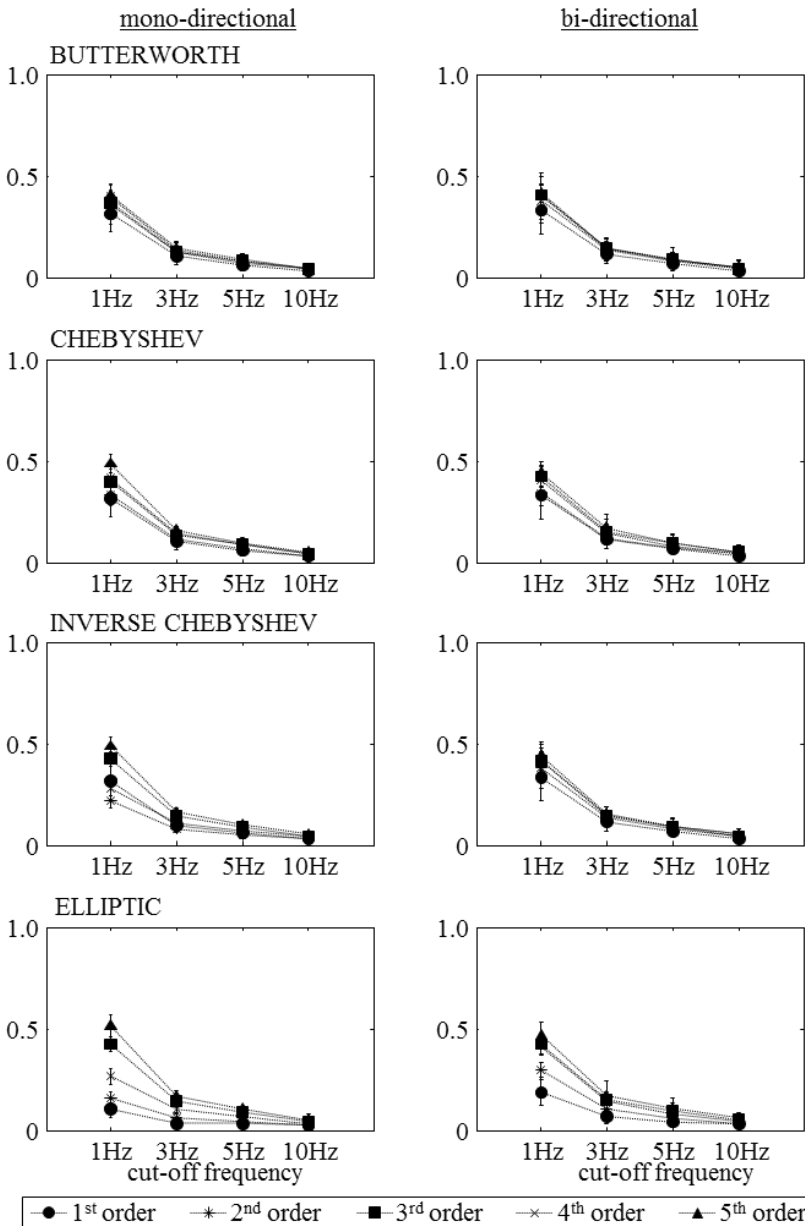


Figure 6. Rise time of the signal's envelope obtained by filter with mono-directional configuration is similar to that obtained with bi-directional configuration.

Mean  $\pm$  standard deviation of computation time for each filter, averaged over 100 signals [ms]

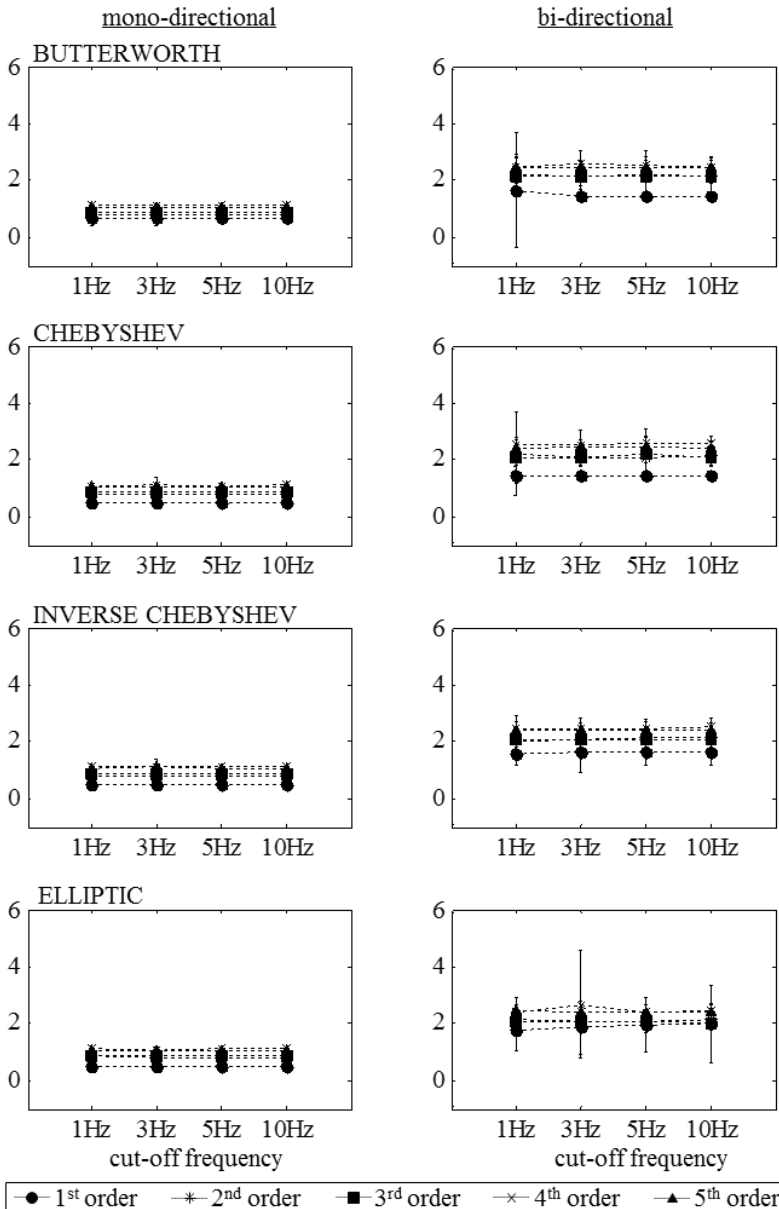


Figure 7. Computation time needed by bi-directional filter is twice of the filter with mono-directional configuration. The specification of the computer used in this calculation is mentioned in section "Materials and method"

Based on these results, we can surmise that the computation time of the bi-directional filters are double compared to that of the mono-directional filters although they provide zero delay and lower RMSE. We found that there is a boundary of the filter's performances (see Figure 8) where the rise time cannot be shorter than 0.025 s, the RMSE cannot be lower than 7.5%, and the computation time cannot be shorter than 0.48 ms.

The results show that none of the filters satisfied all of the criteria. The filters can be categorized based on their performances as follows:

1. filters with short rise time but with high RMSE
2. filters with low RMSE but with long rise time
3. filters which compromised both values (RMSE and rise time).

### Conclusion

Filters with different properties have different performance characteristics. Zero phase filters give no delay to the output and have lower RMSE (computed between output signal and ARV of input signal) despite the longer computation time than the one of a direction filter. Based on the results, we found that there is no filter which has best performance over all criteria. Some trade-off should be considered to have optimum performance on one of the criteria.

The 1<sup>st</sup> order zero phase low pass Elliptic filter with 1 Hz cut off frequency provides the lowest RMSE (7.61%) and zero delay in the output. However, the rise time is 189 ms and it takes 1.79 ms to process a 9 s signal sampled at 2048 Hz.

The shortest rise time of 24ms can be obtained by using a 2<sup>nd</sup> order one directional low pass Elliptic filter with cut off frequency of 10 Hz. The trade offs are high RMSE (14.76%), 17 ms time delay and 0.84 ms of computation time.

The shortest computation time provided by the 1<sup>st</sup> order one directional low pass Elliptic filter is with 3 Hz cut off frequency (0.48 ms). Trade off using this filter is a high RMSE (13.23%), 36 ms of rise time, and 2 ms delay.

Global best filters are selected by choosing filters that have zero delays and close to the data boundary which is obtained with a curve fitting line. The results suggest that the 2<sup>nd</sup> order zero phase Butterworth low pass filter with 5 Hz cut off frequency shows the best performance.

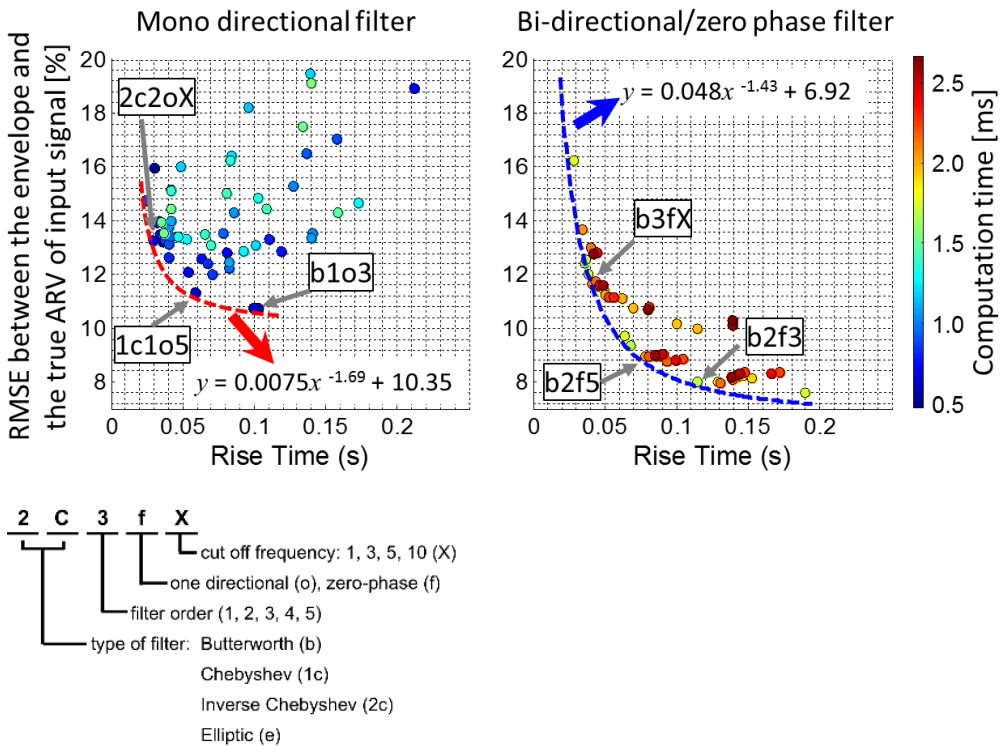


Figure 8. Evaluation of the filter's performance was carried out using 100 simulated sEMG signals. Each point in the plots represents one filter. The left and right plots, respectively, show the performance of mono-directional and bi-directional filters. There is a boundary of performance for each configuration.



**REFERENCES**

- [1] E. A. Clancy, E. L. Morin, and R. Merletti, "Sampling, noise-reduction and amplitude estimation issues in surface electromyography," *J. Electromyogr. Kinesiol.*, vol. 12, no. 1, pp. 1–16, 2002.
- [2] T. D'Alessio and S. Conforto, "Extraction of the envelope from surface EMG signals," *IEEE Engineering in Medicine and Biology Magazine*, vol. 20, no. 6, pp. 55–61, 2001.
- [3] E. Shwedyk, R. Balasubramanian, and R. N. Scott, "A Nonstationary Model for the Electromyogram," no. 5, pp. 417–424, 1977.
- [4] A. Antoniou, *Digital Signal Processing, Signals, Systems and Filters*. McGraw-Hill, 2006.
- [5] J. G. Proakis and D. G. Manolakis, *Digital Signal Processing (3rd Ed.): Principles, Algorithms, and Applications*. Upper Saddle River, NJ, USA: Prentice-Hall, Inc., 1996.



# **Chapter IV**

*Effect of subcutaneous  
layer thickness on the  
sEMG recorded from the  
biceps brachii muscle*



**Effect of subcutaneous layer thickness on the sEMG recorded from the biceps brachii muscle**

**Introduction**

The recorded surface EMG (sEMG) signal is negatively affected by the thickness of a subcutaneous layer (ST) under the electrodes [1]–[3]. A thicker subcutaneous layer means that the distance between the source of the EMG signals and detection electrode is increased, resulting in increased spatial filtering of the EMG signal and hence a decrease in surface EMG amplitude as shown mathematically in [4]–[7]. Previous investigators also demonstrate that subcutaneous fat and skin attenuate the higher spatial frequency components of the sEMG signals [8] and increase the possibility of the recorded sEMG corruption by crosstalk signals from other muscles [9].

However, most of these experimental observations were made under one position of joint angle and one contraction level. It is less well known whether joint angle and contraction level affect the ST which later might give false indication of the real sEMG signals. The reason for the lack of study on the effect of ST at different joint angles and contraction levels on the amplitude of sEMG might be a technical issue, i.e. measuring the ST at the same place for different conditions.

There are two main methods to measure the thickness of a subcutaneous layer: using a skinfold caliper and ultrasound. Some consideration of both techniques has been reported including the error and accuracy of each method. Skinfold caliper, as the classical technique, seems not to provide accurate measurement since the measured value depends on the deformability of the skin and tissue compressibility [10]. On the other hand, subcutaneous layer thickness measured by ultrasound depends on the pressure applied by the probe to the scan site. Changes in pressure by probe application can affect the distribution of adipose tissue and mislead the ultrasonic determination of adipose thickness. Depending on the body area, subcutaneous layer thickness could decrease 25-37% with maximum pressure applied to the ultrasound probe [11]. Comparing these two methods with the result obtained from computed tomography (gold standard), and the measurement using skinfold caliper give superior relative agreement to that exhibited by ultrasound measurements [12]. Despite the advantage and disadvantage, both of the methods are known to have nearly the same degree of accuracy [13] especially if the subjects were young men [14].

In this study, we detected sEMG signals from the biceps brachii during non-fatiguing contractions at different elbow joint angles. The ST values were measured from the same location as the recording electrode using ultrasound technique. Ultrasound technique was chosen since it gave more flexibility to measure ST under actual condition. A customized holder made from ultrasound-transparent material [15] was used to maintain the position of the ultrasound probe during the experiment. The aims were to examine if the ST changed by joint angle and contraction level and to investigate the relation between ST and the amplitude of sEMG. These issues will be addressed in two parts: A) the effect

of contraction level and elbow joint angle to the ST, and B) the relation between the recorded sEMG and measured ST located below the electrodes.

#### **PART A. THE EFFECT OF CONTRACTION LEVEL AND ELBOW JOINT ANGLE ON THE SUBCUTANEOUS LAYER THICKNESS**

##### **Materials and methods**

*Subjects.* Five healthy sedentary men [median (interquartile range): age 25 (5) years; height 171 (2) cm; weight 70 (13) kg] volunteered to participate in the study. No subject had any known neuromuscular or skeletal impairment. Each subject received a detailed explanation of the study and gave written informed consent prior to participation.

*Experimental procedure.* One of the elbow flexor muscles (*biceps brachii*) of the dominant arm (the right side for all subjects) was observed. Participants were sitting comfortably on a chair with their arms 90° flexion, the upper arm of the subjects was rested on a brace, and the lower arm was in supinated position (see Figure 1). The participants were asked to perform isometric contractions at two different contraction levels (rest and 100% of maximum voluntary contraction) and two elbow joint angles (75 and 135 deg.) against the isometric brace. The maximum voluntary contraction (MVC) was measured for each joint angle.

*Measurement of the subcutaneous layer thickness.* Subcutaneous layer thickness (ST) was measured using a B-mode ultrasound (TELEMED). An ultrasound image was taken for each task performed by the participant. The ultrasound probe was placed longitudinally on the upper arm of the participants to avoid excess pressure [11] and was positioned 0.5 cm laterally from the longitudinal centerline of the *biceps brachii* (M) and 1.0 cm below the end of the deltoid muscle with the tip of the probe orientated towards the distal direction. The end of the deltoid muscle was determined by performing transversal examination along the upper arm and was defined as the position where the deltoid muscle no longer appeared on the screen (see Figure 2). To assure that the probe applied on the skin was at the same position and of equal pressure, a custom ultrasound probe holder was used. This probe holder was made from silicon rubber which has acoustic impedance similar to that of the skin therefore transparent to ultrasound [15].

The length of the image captured by the ultrasound probe was 6 cm. The subcutaneous layer thickness (ST) was measured on-screen at seven points with equal distance using electronic calipers, defined by the perpendicular distance between the upper border of the dermal/adipose interface and the upper border of the adipose/muscle interface. Thus for each task and each joint angle, we obtained seven values of ST.

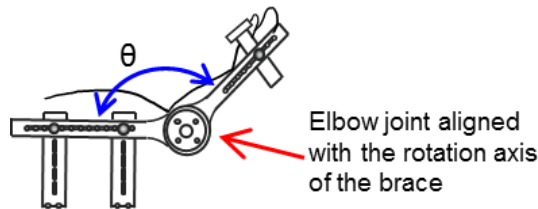


Figure 1. The position of a participant's arm on an isometric brace. The elbow joint was aligned with the rotation axis of the isometric brace. Elbow joint angle  $\theta$  was defined as the internal angle between the upper and lower arm.

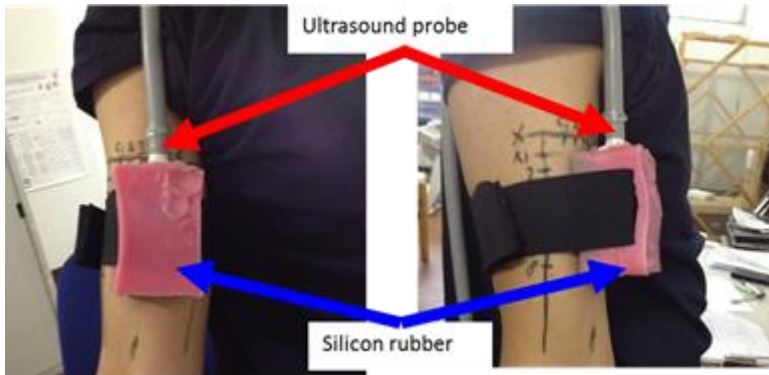


Figure 2. The ultrasound probe was fixed on the participant's upper arm using an elastic band.

## Results and discussion

The ST values obtained from seven measurement points for each participant for each task were averaged for analysis of the characteristic of ST due to different joint angles and contraction levels. In a relaxed condition, the ST of all participants ranged from 2 to 5 mm at 135 deg. elbow joint angle and 3 to 5 mm at 75 deg. elbow joint angle. This finding was in line with those reported in [16].

As shown in Figure 3, a higher contraction level and greater elbow joint angle lead to thinner ST. This phenomenon occurred due to the fact that the skin was more stretched when the participant extended his arm and in the condition of higher contraction level the volume of the muscles increases which further pressed the subcutaneous layer.

The significance of these changes were analyzed using the data from all participants. A Kruskal-Wallis non-parametric test shows that the ST is significantly different ( $p < 0.05$ ) when participants extended their arm at the relaxed condition from 75 deg. to 135 deg., and when the participants performed

a MVC task from the rest condition at 75 deg. joint angle (see Figure 4). There is no significant difference in the ST when the participants extend their arm from 75 deg. to 135 deg. joint angle at the MVC level and when the participants increase the contraction level from the rest condition to MVC at 135 deg. joint angle. In other words, at 135 deg. joint angle the ST tends to be stable, in the range of 2-5 mm, and remains unaffected by the contraction level while at the MVC level the ST is equal for all joint angles.

These findings suggest that increasing sEMG amplitude at lower elbow joint angle (75 deg., loose tissue condition) due to increasing contraction level might also be caused by the decrease of the ST under the electrodes. While, at a higher elbow joint angle (135 deg., more stretched tissue condition), the increment of the sEMG amplitude due to a higher contraction level does not seem to be caused by the difference of ST since there is no significant difference in the ST in both relax and MVC conditions. The effect of different ST on sEMG amplitude is demonstrated in the following section (Part B).

## PART B. THE RELATION BETWEEN THE RECORDED SEMG AND MEASURED ST LOCATED BELOW THE ELECTRODES

### Materials and methods

*Subjects.* Ten healthy sedentary men [median (interquartile range): age 25 (5) years; height 170 (2) cm; weight 70 (16) kg] volunteered to participate in the study. No subject had any known neuromuscular or skeletal impairment. Each subject received a detailed explanation of the study and gave written informed consent prior to participation.

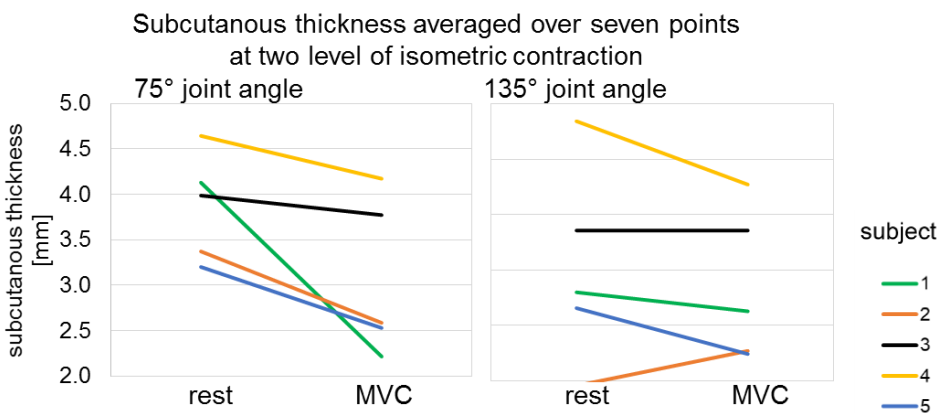


Figure 3. The average values over seven measurement points for each task show that the ST tends to decrease when the contraction level and the elbow angle increase.



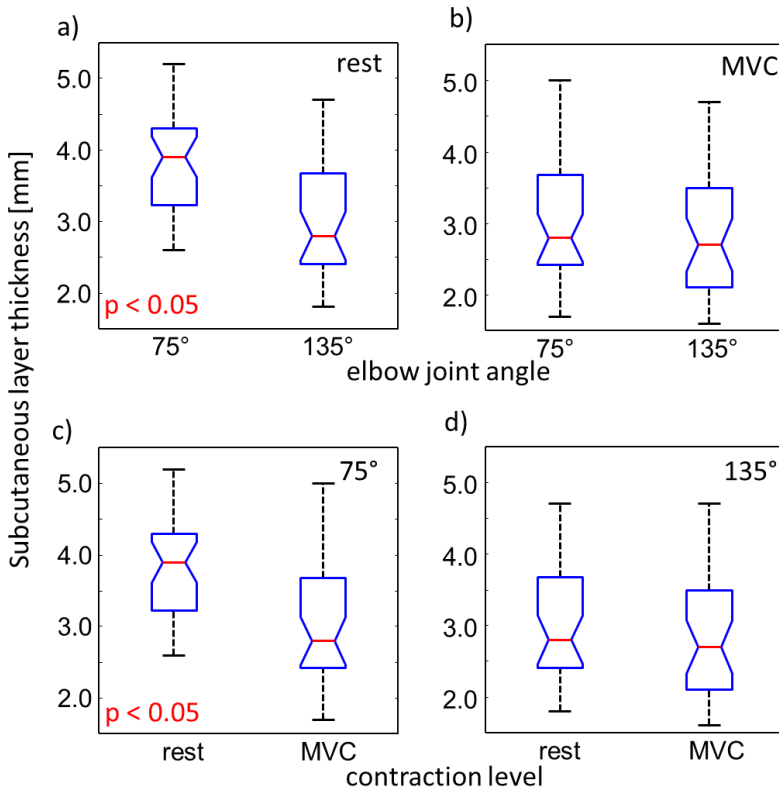


Figure 4. This figure shows the distribution of subcutaneous layer thickness (ST) above the biceps brachii of five male subjects in four different conditions. ST distribution at rest condition and maximum voluntary contraction (MVC) in two elbow joint angles are shown in a) and b) respectively while the values ST at the same joint angles and at different contraction levels are shown in c) and d). The ST values are significantly different in two conditions: a) and c) indicating that ST is influenced by angle at rest (not at MVC) and by contraction level at 75 deg. (not at 135 deg.).

*Experimental procedure.* The biceps brachii of the dominant arm (the right side for all subjects) was investigated. Participants were sitting comfortably on a chair with the arm 90° flexion, the upper arm of the subjects was rested on a brace and the lower arm was in supinated position (see Figure 1). The participants were asked to perform isometric contractions at four different contraction levels (10%, 30%, 50% and 100% of MVC) and two elbow joint angles (75 and 135 degree) against the isometric brace. The MVC was measured for each joint angle.

*Measurement of the subcutaneous layer thickness.* Subcutaneous layer thickness (ST) were measured using a B-mode ultrasound (TELEMED) for each task as explained in Part A.

*Surface EMG recordings.* After taking the ultrasound images the surface EMG signals were recorded from the same location where the subcutaneous layer thickness was measured. A flexible array of electrodes (8 electrodes, 10mm inter-electrode distance) was placed over the biceps brachii aligned with the position of the ultrasound probe (see Part A and Figure 5) after slightly abrading the skin with abrasive paste (Nuprep; Weaver and Company, USA) and cleaning it with water. The 5 s of monopolar signals were sampled at 2kHz and the center 3 s of the signals were used for further offline processing.

*EMG data processing.* After signal preprocessing (2<sup>nd</sup> order zero lag bandpass Butterworth filter, final cut off frequency 20-500Hz) and power line attenuation using spectral interpolation [17], the RMS values from each single differential channel were computed within 1s epoch and averaged over 3 epoch. The selection of the time window was based on previous studies [18] showing that for non-fatiguing isometric contraction with constant force, the EMG signal can be considered stationary (i.e., autocorrelation function of the EMG signal does not change with time) for epoch duration of 1-2 seconds. Thus for each task and each participant, we obtained seven RMS values which correspond to seven ST measurement points. RMS values and their paired ST originated outside the tendon area and innervation zones were similar and therefore averaged and used for further analysis.

*Statistics.* Data processing and statistic calculation was performed with Curve Fitting Toolbox from MATLAB version R2014a.

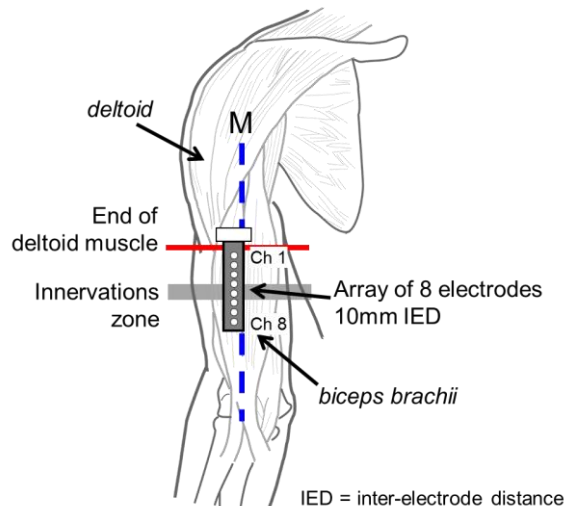


Figure 5. Placement of the electrodes array over the biceps brachii. The array was aligned with the position of the ultrasound probe (see Figure 2), i.e. 0.5 cm laterally from centerline of the biceps brachii (M). Seven longitudinal differential channels were used for further analysis

### Results and discussion

The RMS values from ten participants were plotted against their corresponding ST values for each task (see Figure 6). A fitting line using a power model,  $y = ax^m$  with  $x$  is the ST in mm and  $y$  is the RMS value, was computed for each group of tasks. These RMS values increase with the increment of the contraction level and slightly affected by different joint angles.

Higher contraction level tends to increase the decay rate when the arm was positioned at 135 deg. elbow joint angle but not at 75 deg. This finding supports the hypothesis that the subcutaneous tissue layer produces an attenuation as previously investigated [1]–[3] and can be explained as the increasing distance between the source and the detection system. As the subcutaneous layer has resistive behavior with the EMG signal in general, greater distance means greater resistance and therefore results in a higher voltage drop between the source and the detection system. The decrement of measured EMG signal due to distance follows a power function [19]. As shown in Figure 6, a negative trend of the RMS values along with the increment of subcutaneous layer thickness is detected in every task as decay in amplitude with rate 0.69 to 2.11 power of the ST in mm. The Spearman test shows a negative correlation between subcutaneous layer thickness and RMS values for the two joint angles and four contraction levels ( $R = -0.58 \pm 0.10$ , range -0.45 to -0.78) although it is only significant when the joint angle is 135 deg. with maximal contraction level ( $p < 0.05$ ).

This present study shows result similar to those of a previous investigation involving lean and obese patients ( $n=28$ ) [2]. One of their objectives is to investigate if surface EMG signals can be detected from the quadriceps muscle of severely obese patients. In that investigation, the monopolar sEMG signals from *quadriceps femoris* muscle were recorded using two arrays of eight electrodes with 5mm inter electrode distance attached on both the *vastus lateralis* and *medialis*. Each of the subject performed the voluntary exercise in a seated posture on a horizontal leg press machine with 120° knee angle and five contraction levels (15%, 30%, 50%, 70%, and 100% MVC). As shown in Figure 7, they found that there is a non-linear relation between subcutaneous tissue thickness and RMS estimates obtained from all of the subjects for the five contraction levels and the 10mm inter electrode distance.

They observed a significant negative correlation between subcutaneous tissue thickness and RMS estimates using the Spearman test with  $R = -0.86 \pm 0.02$ , range -0.81 to -0.92 for values obtained from *vastus medialis*. In the mentioned study, the correlation is stronger than present study.

To obtain general information about the effect of subcutaneous layer thickness to the RMS values, all the data from 10 participants were collected. After removing the data outside the 95% confidence interval, a regression line in log coordinates is drawn (see Figure 8). The Spearman test of this set of RMS-ST values shows a significant negative correlation between the thickness of subcutaneous layer thickness and RMS values ( $R = -0.64$ ,  $p < 0.05$ ).

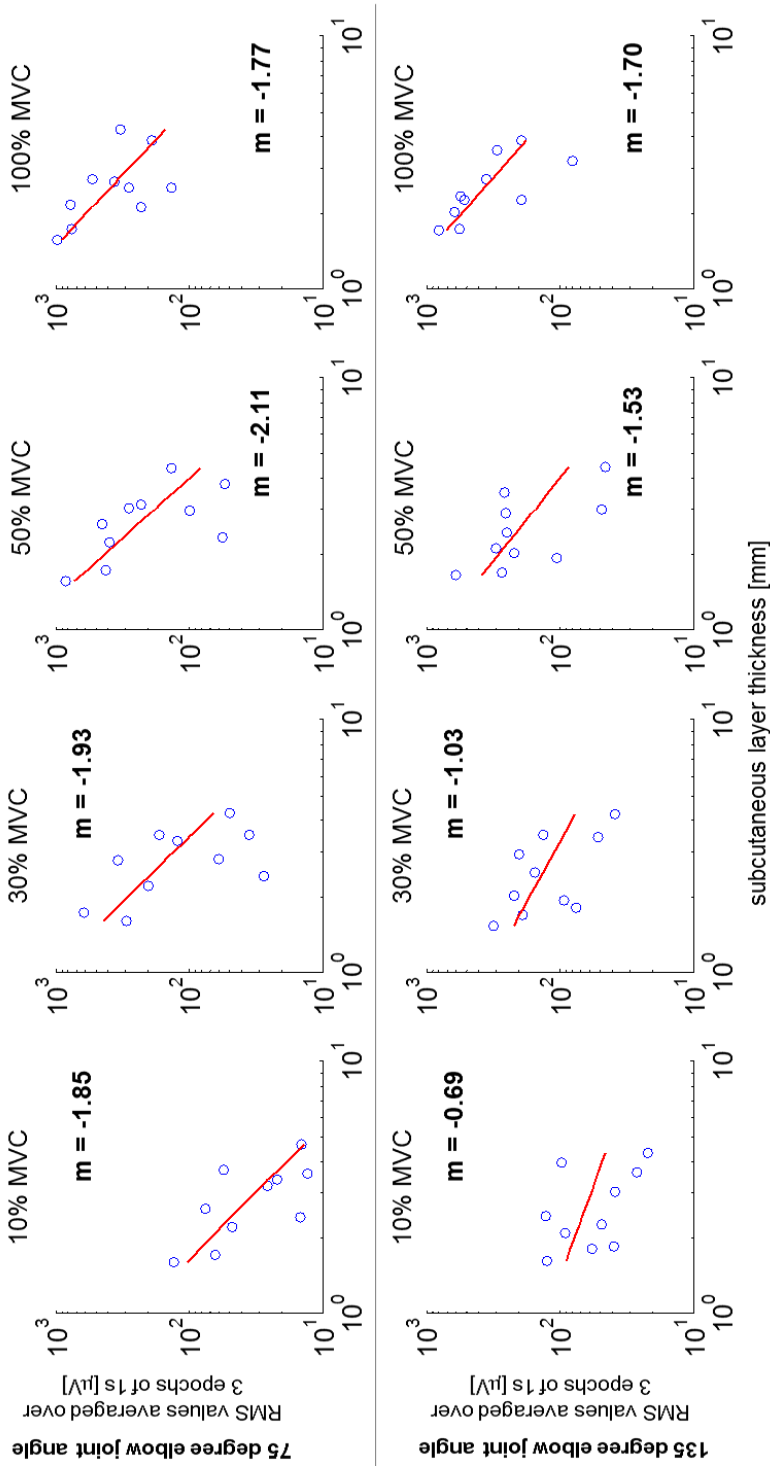


Figure 6. The averaged RMS values computed at the same location as the subcutaneous layer thickness (ST) measurement point show the same characteristics against the ST in all tasks performed by ten participants. Gradient of the fitting line in logarithmic scale 'm' showing the severeness of the effect of ST on the recorded RMS value. These plots show that thicker ST results in lower RMS values and the decrement ranged from 0.69 to 2.11 decade/decade. The fitting line for each condition follows a power equation in linear scale  $y = ax^m$ .

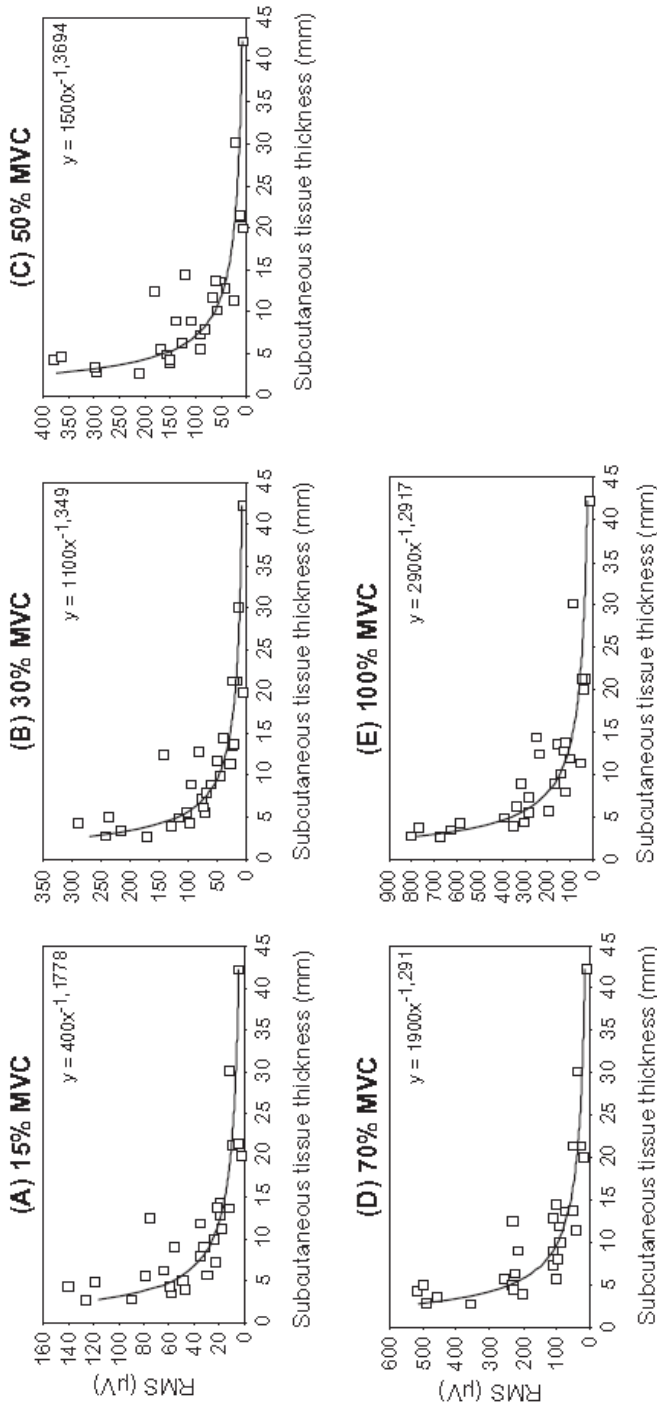


Figure 7. A negative non-linear correlation between subcutaneous layer thickness and RMS estimated from vastus medialis for all contraction levels and the 10mm inter electrode distance was observed. The measured data were fitted with line  $y=ax^b$  where  $x$  is subcutaneous layer thickness in mm. The RMS were decayed with power of 1.2 to 1.4. This figure was taken from [2].

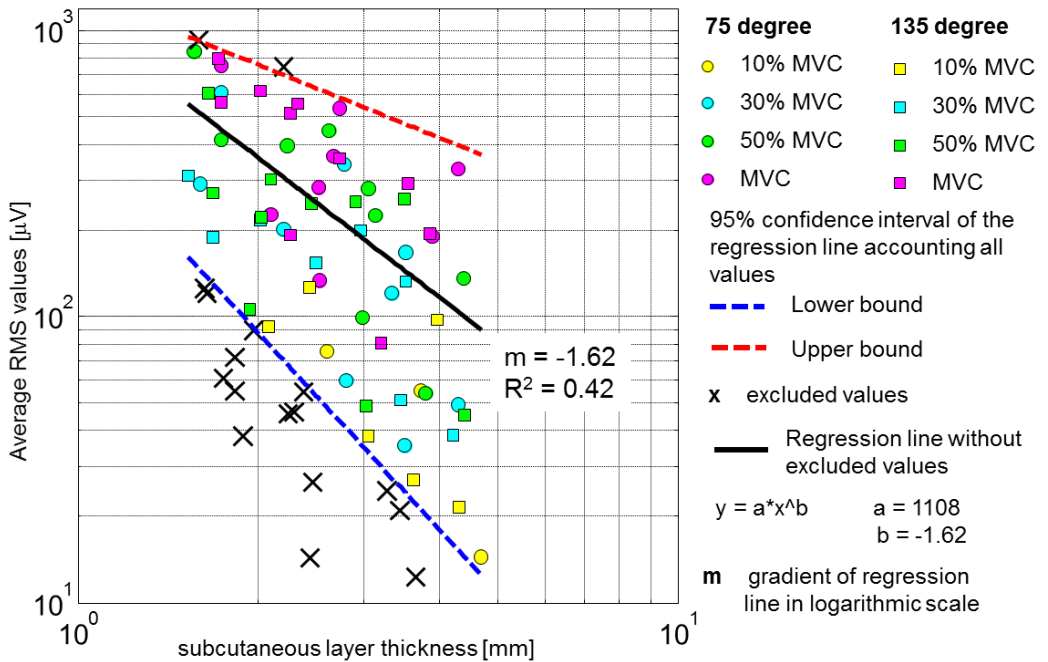


Figure 8. The global plot of averaged RMS values against the subcutaneous layer thickness (ST) at corresponding point shows that RMS values tend to decrease as thicker ST with 1.62 decade/decade.

### Conclusion

The present work shows that the subcutaneous layer thickness (ST) changes due to two factors: joint angle and contraction level except for two conditions: a) the maximum voluntary contraction where the ST is not affected by the joint angle, and b) the extended arm where the ST is not affected by the level of contraction. This work also demonstrates that at thicker ST, the amplitude of recorded sEMG (presented as RMS value) is lower than those coming from thinner ST (see Figure 8). One possible explanation is at MVC and at stretched arm the subcutaneous tissue is less soft and not so compressible as in the other conditions.

It is suggested that at the condition of flexed arm, the increasing RMS value at higher contraction level is not only caused by the increasing rate of motor unit firing and recruitment of another motor unit, but also by the decreasing ST. However, generalized mathematical correlation between ST and surface RMS is poor since the exact location of the motor units with respect to the recording electrode remains unknown. In addition, other properties of the subcutaneous tissue (such as conductivity, anisotropy and dishomogeneity) are not known.

## REFERENCES

- [1] C. Nordander, J. Willner, G.-Å. Hansson, B. Larsson, J. Unge, L. Granquist, and S. Skerfving, "Influence of the subcutaneous fat layer, as measured by ultrasound, skinfold calipers and BMI, on the EMG amplitude," *Eur. J. Appl. Physiol.*, vol. 89, no. 6, pp. 514–519, 2003.
- [2] M. A. Minetto, A. Botter, S. Šprager, F. Agosti, A. Patrizi, F. Lanfranco, and A. Sartorio, "Feasibility study of detecting surface electromyograms in severely obese patients," *J. Electromyogr. Kinesiol.*, vol. 23, no. 2, pp. 285–295, 2013.
- [3] H. Baars, T. Jöllenbeck, H. Humburg, and J. Schröder, "Surface-electromyography: skin and subcutaneous fat tissue attenuate amplitude and frequency parameters," in *ISBS-Conf. Proc. Arch*, 2007, vol. 1.
- [4] T. A. Kuiken, M. M. Lowery, and N. S. Stoykov, "The effect of subcutaneous fat on myoelectric signal amplitude and cross-talk," *Prosthet. Orthot. Int.*, vol. 27, no. 1, pp. 48–54, Apr. 2003.
- [5] K. Roeleveld, J. H. Blok, D. F. Stegeman, and A. Van Oosterom, "Volume conduction models for surface EMG; confrontation with measurements," *J. Electromyogr. Kinesiol.*, vol. 7, no. 4, pp. 221–232, 1997.
- [6] D. Farina and A. Rainoldi, "Compensation of the effect of sub-cutaneous tissue layers on surface EMG: a simulation study," *Med. Eng. Phys.*, vol. 21, no. 6, pp. 487–497, 1999.
- [7] D. Farina and R. Merletti, "A novel approach for precise simulation of the EMG signal detected by surface electrodes," *Biomed. Eng. IEEE Trans.*, vol. 48, no. 6, pp. 637–646, 2001.
- [8] B. Gerdle, S. Karlsson, S. Day, and M. Djupsjöbacka, "Acquisition, processing and analysis of the surface electromyogram," in *Modern techniques in neuroscience research*, Springer, 1999, pp. 705–755.
- [9] C. J. De Luca and R. Merletti, "Surface myoelectric signal cross-talk among muscles of the leg," *Electroencephalogr. Clin. Neurophysiol.*, vol. 69, no. 6, pp. 568–575, 1988.
- [10] H. C. Lukaski, "Methods for the assessment of human body composition: traditional and new.," *Am. J. Clin. Nutr.*, vol. 46, no. 4, pp. 537–556, 1987.
- [11] C. Toomey, K. McCreesh, S. Leahy, and P. Jakeman, "Technical considerations for accurate measurement of subcutaneous adipose tissue thickness using B-mode ultrasound," *Ultrasound*, vol. 19, no. 2, pp. 91–96, May 2011.
- [12] C. Orphanidou, L. McCargar, C. L. Birmingham, J. Mathieson, and E. Goldner, "Accuracy of subcutaneous fat measurement: Comparison of skinfold calipers, ultrasound, and computed tomography," *J. Am. Diet. Assoc.*, vol. 94, no. 8, pp. 855–858, 1994.
- [13] M. T. Fanelli and R. J. Kuczmarski, "Ultrasound as an approach to assessing body composition.," *Am. J. Clin. Nutr.*, vol. 39, no. 5, pp. 703–709, May 1984.
- [14] T. Weits, E. J. Van Der Beek, and M. Wedel, "Comparison of ultrasound and skinfold caliper measurement of subcutaneous fat tissue.," *Int. J. Obes.*, vol. 10, no. 3, pp. 161–168, 1985.
- [15] A. Botter, T. M. M. Vieira, I. D. Loram, R. Merletti, and E. F. Hodson-Tole, "A novel system of electrodes transparent to ultrasound for simultaneous detection of myoelectric activity and B-mode ultrasound images of skeletal muscles," *J. Appl. Physiol.*, vol. 115, no.

- 8, pp. 1203–1214, 2013.
- [16] J. V. G. A. Durmin and J. Womersley, “Body fat assessed from total body density and its estimation from skinfold thickness : measurements on 481 men and women aged from 16 to 72 Years,” *Br. J. Nutr.*, vol. 32, no. 01, pp. 77 – 97, 1974.
- [17] D. T. Mewett, H. Nazeran, and K. J. Reynolds, “Removing Power Line Noise From Recorded EMG,” in *Proceedings of the 23rd Annual EMBS International Conference*, 2001, pp. 2190–2193.
- [18] E. A. Clancy, D. Farina, and G. Filligoi, “Single-Channel Techniques for Information Extraction from the Surface EMG Signal,” in *Electromyography: Physiology, Engineering, and Noninvasive Applications*, R. Merletti and P. Parker, Eds. John Wiley & Sons, Inc., 2004.
- [19] K. Roeleveld, D. F. Stegeman, H. M. Vingerhoets, and A. van Oosterom, “Motor unit potential contribution to surface electromyography,” *Acta Physiol. Scand.*, vol. 160, no. 2, pp. 175–183, 1997.





# Part II



*High density detection systems:  
evaluating optimal configuration*



# Chapter V

*Electrode's size and  
estimation of biceps  
brachii muscle activity*



## Electrode's size and estimation of biceps brachii muscle activity

*Adapted from:*

*P. Cattarello, S. D. H. Soedirdjo, B. Afsharipour, and R. Merletti. Effect of electrode size on amplitude estimation of HDsEMG maps. "3rd International Conference on NeuroRehabilitation", Segovia, Spain, October 18-21, 2016.*

*Submitted*

### **Abstract**

The purpose of this work is to evaluate the effect of the electrode size on recorded High Density surface electromyography (HDsEMG) maps. We recorded the sEMG signals using a grid of electrodes placed on biceps brachii (5 mm inter-electrode distance, IED). Each instantaneous map was interpolated using the 2D Sinc function to obtain a "continuous" map (10,000 samples/m). To simulate acquisition with different electrode sizes, each "continuous" map was filtered with a circular averaging filter (2-10 mm diameter) and re-sampled with a 10 mm IED. The inverse transfer function of the filter was applied on each map to compensate for the effect of the electrode size. We used the power ( $\text{RMS}^2$ ) of each map to quantify these effects. The results suggest that a greater electrode size implies a higher error of power values with respect to the "continuous" map. Depends on the IED, electrode with diameter smaller than 6 mm do not introduce significant alteration of power of the map.

### **Introduction**

The activity of the whole muscle can be observed by recording the sEMG signals using a grid of equally spaced electrodes (HDsEMG). The monopolar signals can be shown as a series of maps where each pixel in each sEMG map represents the instantaneous amplitude of the signal at the corresponding channel. The features of these maps (such as their power) are affected by three factors: a) the size of the electrodes, b) the inter electrode distance (IED), and c) the size of the grid. The size of the electrode was reported to have no effect on the estimation of the conduction velocity in the case of fibers inclined with respect to the detection system [1]. Another investigation reports that different sizes of electrodes give similar results on the detection depth of motor unit action potentials [2]. However, it is not known how these differences in size will affect the estimation of sEMG amplitude.

Two electrode's shapes that are widely used are circular and square. The impulse responses ( $h_E$ ) for every point in the space  $(x,y)$  of a circular electrode with radius  $r$  is defined as [3]

$$h_E(x, y) = \begin{cases} 1/\pi r^2 & \text{if } x^2 + y^2 \leq r^2 \\ 0 & \text{otherwise} \end{cases} \quad (1)$$

In the frequency domain, the transfer function (TF) of a circular electrode in Cartesian coordinate is

$$H_E(r, f_x, f_y) = \frac{2 \cdot J_1\left(2\pi \cdot r \cdot \sqrt{f_x^2 + f_y^2}\right)}{2\pi \cdot r \cdot \sqrt{f_x^2 + f_y^2}} \quad (2)$$

where  $J_1$  is the Bessel function of first kind and first order,  $f_x$  and  $f_y$  are the frequency component in the  $x$  and  $y$  directions. Since the TF of a circular electrode has circular symmetry, we can show only a section of the 2D transfer function, as in Figure 1, over a bandwidth of 200 cycles/m.

In case of rectangular electrode with side  $a$ , the impulse responses ( $h_E$ ) for every point in the space ( $x, y$ ) is

$$h_E(x, y) = \begin{cases} 1/a^2 & \text{if } -a/2 \leq x \leq a/2 \wedge -a/2 \leq y \leq a/2 \\ 0 & \text{otherwise} \end{cases} \quad (3)$$

This TF in frequency domain becomes

$$H_E(a, f_x, f_y) = \text{sinc}(a \cdot f_x) \text{sinc}(a \cdot f_y) \quad (4)$$

Different from the TF of the circular electrode, TF of the square electrode only has symmetry at  $f_x$  equal to zero or  $f_y$  equal to zero as shown in Figure 2.

Circular electrode is more common than the square electrode. In this study we investigate the effect of different diameter of circular electrode on the power of the recorded sEMG maps.

## Materials and methods

*Experimental procedure.* The sEMG signals were recorded using a grid of electrodes (16x8,  $\varnothing = 1$  mm, IED = 5 mm) placed on the short head of biceps brachii of a subject holding a 4 Kg weight with 90° elbow flexion (see Figure 3). The skin was abraded and rinsed with water before attachment of the grid.

*Signal processing.* Bandpass filtering (20-500 Hz, 2<sup>nd</sup> order Butterworth zero phase filter), power line interference attenuation (by spectral interpolation), bad channel removal, and offset removal in time were performed for each signal. We recorded 30s monopolar sEMG signals sampled at 2048 Hz, and processed the central 15s. Signal processing was performed with MATLAB.

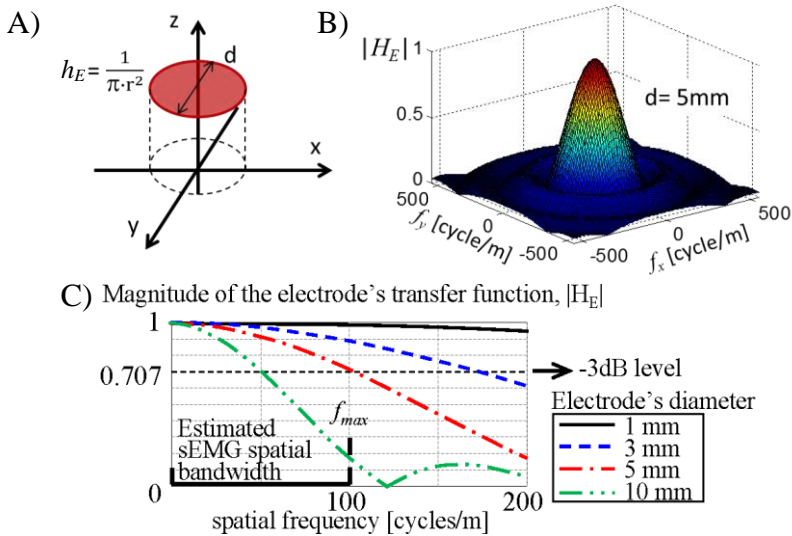


Figure 1. Impulse response of a circular electrode is depicted in A. Panel B shows the 2D transfer function of the electrode in frequency domain. Magnitude of the transfer function of a circular electrode ( $\varnothing = r = 1, 3, 5,$  and  $10$  mm) versus spatial frequencies are shown in panel C.  $f_{max}$  is the estimated max freq of sEMG in space.

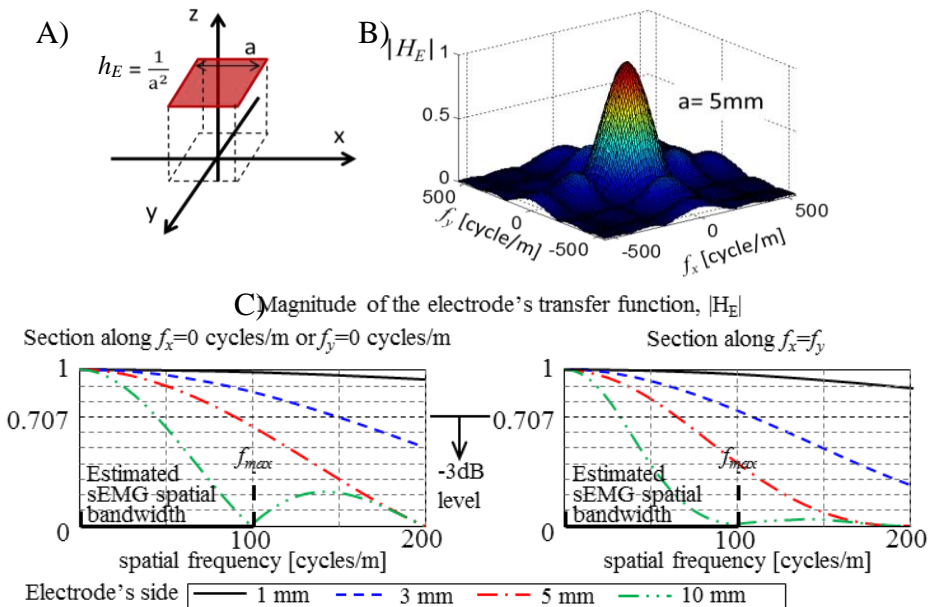


Figure 2. Impulse response of a square electrode is depicted in A. Panel B shows the 2D transfer function of the electrode in frequency domain. Magnitude of the transfer function of a square electrode ( $a = 1, 3, 5,$  and  $10$  mm) versus spatial frequencies are shown in panel C.  $f_{max}$  is the estimated max freq of sEMG in space.

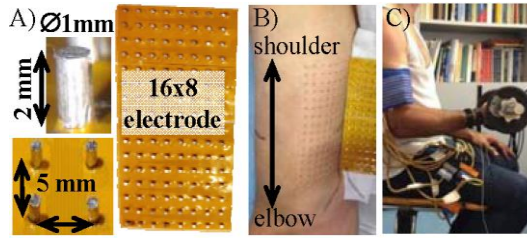


Figure 3. The grid of electrodes (A) is attached to the skin over the short head of biceps brachii (B) of the right hand of a subject holding 4Kg weight with 90° elbow flexion (C).

As mentioned above, the recorded sEMG maps are also affected by the IED. IED defines the EMG spatial sampling ( $f_s$ ). Insufficient spatial sampling frequency prevents us from reconstructing the spatial distribution of the muscle activity as well as the map of features (e.g. RMS value)<sup>1</sup>. Based on this fact, we remove the maps that have aliasing to limit the IED factors that affect the sEMG recordings. To define aliasing, the sEMG sampled in space at  $f_s$  greater than twice of its maximum spatial frequency component ( $f_{max}$ ) must be available. In other words, we need to have maps which satisfy the Shannon-Nyquist theorem [4]. Therefore, we establish an arbitrary definition of  $f_{max}$  based on the area spectrum where we reach 95% of the total power.

The Fourier transform with zero padding in space (64x64 points) is performed for each of the sEMG maps without removing the DC component. The apparent spatial frequency resolution is 3.125 c/m. Then we analyze the first quadrant, where all the frequencies are positive ( $+f_{x1}$ ,  $+f_{y1}$ ), and the second quadrant, where the vertical frequencies are negative and the horizontal frequencies are positive ( $+f_{x2}$ ,  $-f_{y2}$ ). We find  $f_{x1}$ ,  $f_{y1}$ ,  $f_{x2}$ , and  $f_{y2}$  such that the sum of the power reaches 95% of the total power in both quadrants.

$$P_i(f_{x1}, f_{y1}, f_{x2}, f_{y2}) = \sum_{u1=0}^{f_{x1}} \sum_{v1=0}^{f_{y1}} \sum_{u2=0}^{f_{x2}} \sum_{v2=0}^{f_{y2}} \left[ |c_i(u1, v1)|^2 + |c_i(u2, -v2)|^2 \right] \quad (5)$$

where  $c_i$  is the Fourier coefficient while  $P_i$  is the power of each map at time sample  $i$  computed up to spatial frequencies ( $f_{x1}$ ,  $f_{y1}$ ) for the first quadrant and up to spatial frequencies ( $f_{x2}$ ,  $f_{y2}$ ) for the fourth quadrant. Total power in both quadrants is obtained when  $f_{x1}$ ,  $f_{x2}$ ,  $f_{y1}$ , and  $f_{y2}$  are equal to 100 c/m. If there is more than one combination of the four frequencies, the one with largest  $f_x$  or  $f_y$  is considered.

Then we define  $f_{max}$  as the highest value among  $f_{x1}$ ,  $f_{y1}$ ,  $f_{x2}$ , and  $f_{y2}$ . Maps whose  $f_{max}$  greater than 87.5 c/m are categorized as maps with “spatial aliasing” (**definition 1**) and they are excluded from further analysis (see Figure 4). The total number of the maps without “aliasing” is 17258 out of 30720 maps.

<sup>1</sup> Estimation of the sEMG spatial bandwidth is discussed in Chapter 6 while the effect of IED on the sEMG RMS estimation will be discussed in Chapter 7.



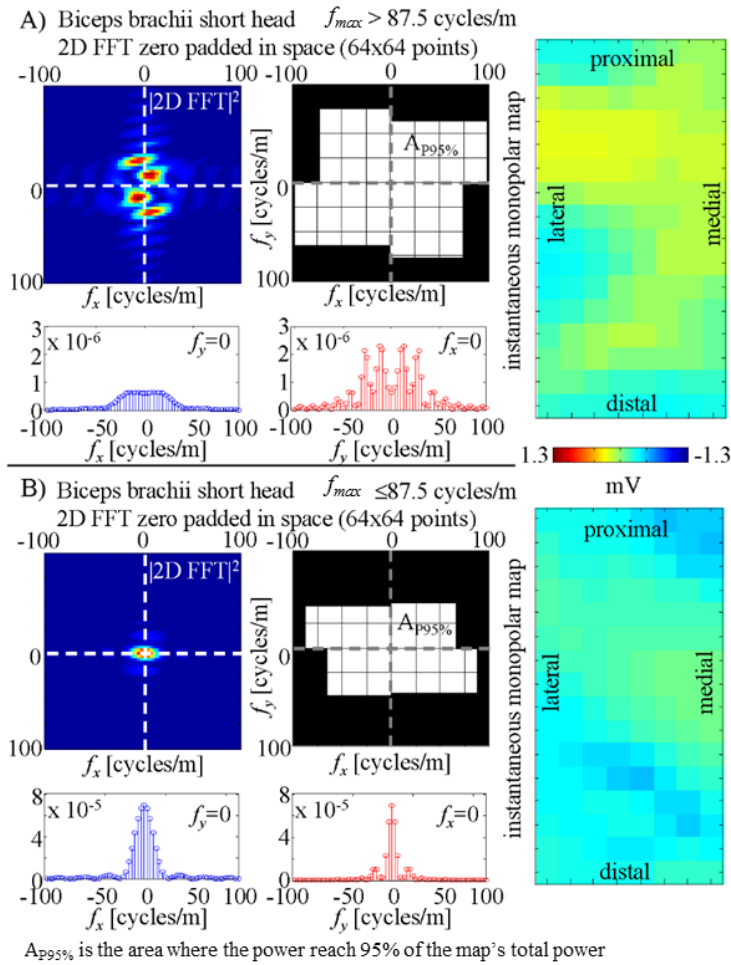


Figure 4. We evaluate the first and second quadrant of the 2D FFT. Panel A demonstrates an example of a map whose  $f_{max} > 87.5$  cycles/m and Panel B shows the other case.

**Data analysis.** We then remove the last row and the last column of the maps. A 2D Sinc function in space was applied to each of the selected maps to obtain the “continuous” maps (10,000 samples/m). Then we applied to each “continuous” map a circular averaging filter, with a size equal to the diameter of the electrode (2, 4, 6, 8, and 10 mm). We resampled the obtained images with 10 mm IED by maintaining the position of each electrode's center. The inverse TF ( $1/H_E$ ) of the electrode was applied to the Fourier Transform of each sampled map to try to compensate for the effect of the electrode size.

We computed the power of: a) each “continuous” map  $P_a$ , b) each sampled “continuous” map (100 samples/m)  $P_b$ , c) each map obtained by different

electrode size  $P_c$ , and d) each map after compensation with the inverse TF  $P_d$ . The relative error of the power of the maps obtained by different electrode size, (before and after applying inverse TF) with respect to the “continuous” ( $P_a$ ) and resampled “continuous” maps ( $P_b$ ), were computed for each time sample  $i$ .

$$P_{[\bullet]}(i) = \frac{1}{MN} \sum_{m=1}^M \sum_{n=1}^N I_{[\bullet]}(m, n, i)^2 \quad (6)$$

$$\Delta P\%(i) = \left[ \frac{P_{est}(i) - P_{ref}(i)}{P_{ref}(i)} \right] \cdot 100 \quad (7)$$

where  $\bullet$  is  $a, b, c$ , or  $d$ ;  $P_{est}$  refers to  $P_c$  or  $P_d$  while  $P_{ref}$  refers to  $P_a$  or  $P_b$ .  $M$  and  $N$  are the numbers of electrodes respectively in vertical and horizontal directions; 7 by 3 electrodes for sampled map with 100 samples/m and 701 by 301 for the “continuous” map.

### Results and discussion

The process of acquiring the sEMG map ( $R[m,n]$ ) with a grid of electrodes ( $M \times N$  having  $IED = w$ ) can be explained as sampling a limited size (rect ( $x,y$ )) of a “continuous” map ( $i(x,y)$ ) of muscle activity after applying a moving average filter ( $h_E$ ) whose shape and size are those of the electrode.

$$R[m,n] = \{ [A(x,y) \cdot \text{rect}(x,y)] * h_E(x,y) \} \cdot \sum_{m=0}^M \sum_{n=0}^N \delta(x - n \cdot w, y - m \cdot w) \quad (8)$$

The ideal measurement implies a point-like electrode with IED much smaller than  $1/(2 \cdot f_{max})$ . This condition is not feasible and the size of the electrode needs to be considered. Greater size of electrode implies that we average greater area (1). The power (RMS<sup>2</sup> in space) of each image obtained with different size of the electrodes can be higher or lower than that of the “continuous” map. Figure 5 shows an example of a map whose power in space is decreases along with greater diameter of the electrode and the same IED (10mm).

We compared the power of the maps obtained by different electrode size with that of the maps obtained by point-like electrodes with 10 mm IED. These errors increase with greater electrode size (see Figure 7A), but are negligible (<5%) for electrode with diameter smaller or equal to 4 mm. Applying the inverse TF of the electrode to the maps improves the results especially for large electrodes. However, in many cases it tends to overcompensate the results.

It is interesting to evaluate how the power of a sEMG map is affected by the electrode size and by the IED. We calculate the errors between the power of the maps obtained by different electrode sizes at 10 mm IED (100 samples/m) and the power of “continuous” maps (10,000 samples/m). Figure 7B shows that the error of the power estimation for a single map could reach up to 20%. Inverse TF does not reduce the error for an electrode with diameter smaller or equal to 4 mm.

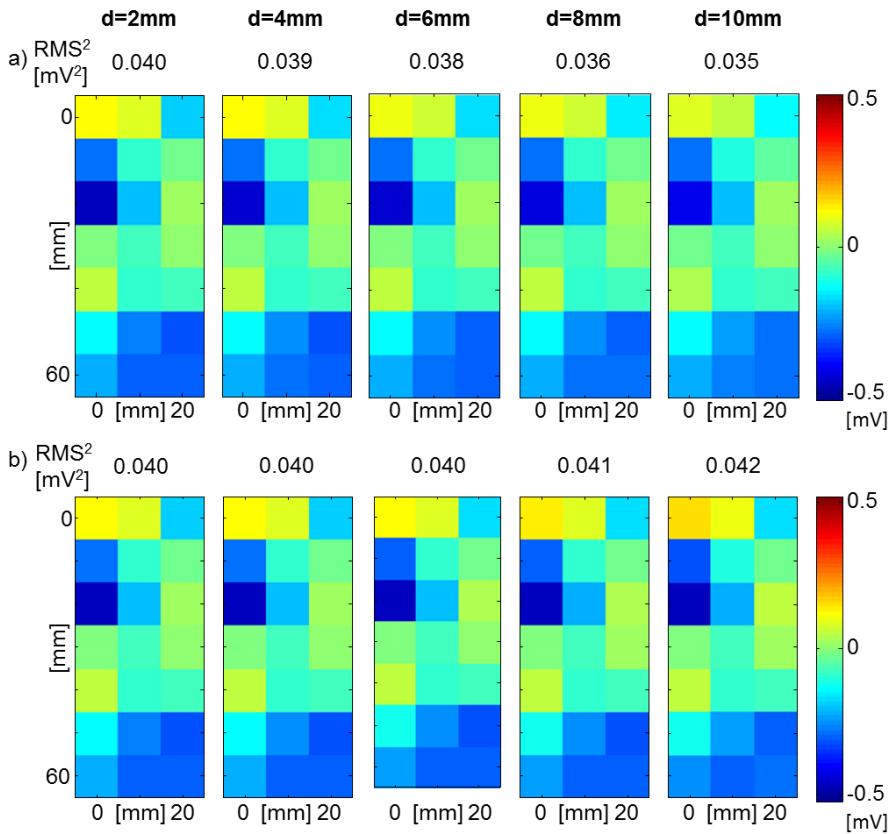


Figure 5. This figure demonstrates an example of: a) the filtering effect due to different diameter ( $d$ ) of circular electrode with IED = 10mm. b) the results of compensation by inverse filtering on images from different diameter of electrode to estimate the real values.

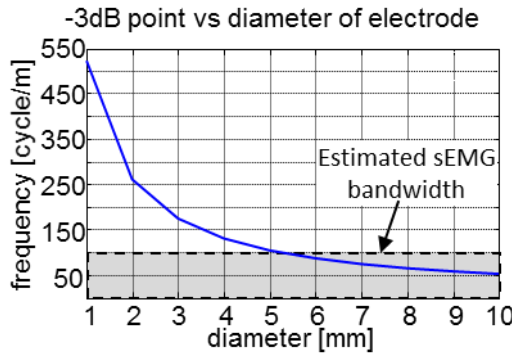


Figure 6. This figure shows the frequency where the power is attenuated by 50% (3dB point of the transfer function for circular electrode). Greater size of the electrode shifts the -3dB point to the lower spatial frequency.

Greater electrode size implies higher low-pass filtering (see Figure 1 and Figure 6) which should decrease the power of the maps and produce negative errors (4). However, Figure 7 shows that many maps have positive errors. The 10 mm IED could be the reason for these positive errors as it introduces spatial aliasing. Moreover, since the TF averages the potential under the contact area (1), the averaged value could be greater or smaller than the value obtained by a point-like electrode in the center point of the area. The discretization of the electrode TF and of  $1/H_E$  could be an additional reason for the power overestimation.

Based on this finding, we can infer that the error of power estimates in space is affected mainly by the IED rather than the electrode size when the diameter of the electrode smaller than 5mm (see Figure 6). The large range of the errors indicates that the electrode size and IED have effects that depend on the frequency components of the map.

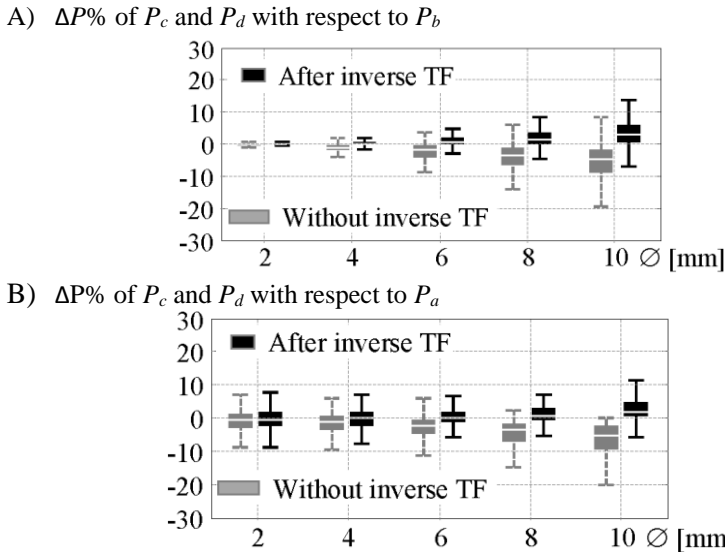


Figure 7. This figure shows boxplot (without outliers) of the relative error  $\Delta P\%$  of the power ( $RMS^2$ ) value computed on each map with respect to: A) the “continuous” map sampled at 100 samples/m, and B) the “continuous” map (10,000 samples/m).  $P_a$ ,  $P_b$ ,  $P_c$ , and  $P_d$  are the power of “a continuous” map, a sampled “continuous” map (100 samples/m), the power of each map obtained by different electrode size, and the power of each map after invers TF respectively. Median, 1°, 3° quartile, and range with  $N=17258$ . See (3) and (4) for computational details.

**Conclusion**

The error range of power ( $\text{RMS}^2$ ) due to electrode size of the EMG maps is smaller than the error due to the IED, although these two parameters are connected ( $d < \text{IED}$ ). Applying the inverse electrode TF to the maps reduces the errors only when we compare this with the resampled (100 samples/m) “continuous” map. On the other hand, larger electrode sizes provide an anti-aliasing filter (Figure 1) which reduces the spatial bandwidth of sEMG. This effect remains to be investigated.

**REFERENCES**

- [1] D. Farina, C. Cescon, and R. Merletti, "Influence of anatomical, physical, and detection-system parameters on surface EMG," *Biol. Cybern.*, vol. 86, no. 6, pp. 445–456, 2002.
- [2] A. J. Fuglevand, D. A. Winter, A. E. Patla, and D. Stashuk, "Detection of motor unit action potentials with surface electrodes: influence of electrode size and spacing," *Biol. Cybern.*, vol. 67, no. 2, pp. 143–153, 1992.
- [3] R. Merletti and P. A. Parker, *Electromyography: physiology, engineering, and non-invasive applications*, vol. 11. John Wiley & Sons, 2004.
- [4] A. K. Jain, *Fundamentals of Digital Image Processing*. Upper Saddle River, NJ, USA: Prentice-Hall, Inc., 1989.

# **Chapter VI**

*Surface EMG spatial  
frequency bandwidth  
analysis*





## Surface EMG spatial frequency bandwidth analysis

*Adapted from:*

*S. D. H. Soedirdjo, B. Afsharipour, P. Cattarello, and R. Merletti. Surface EMG spatial frequency bandwidth: preliminary estimation. "3rd International Conference on NeuroRehabilitation", Segovia, Spain, October 18-21, 2016. Submitted*

### **Abstract**

Appropriate inter-electrode distance (IED) is needed to enable the reconstruction of detailed muscle activity and obtain correct map's features of HDsEMG. The spatial frequency bandwidth of sEMG was estimated by placing a grid of 16x8 pin electrodes (IED = 5 mm) on the biceps brachii (BB) and medial deltoid (MD) of a subject. Signals were sampled at 2048Hz for 15s (30720 samples). The zero padded 2D FFT (64x64 points) was performed for each instantaneous map without removing the offset of the map. Two arbitrary approaches of spatial bandwidth  $f_{max}$  were tested: 1)  $f_{max}$  smaller or equal to 87.5 c/m that supports 90% of total power, 2)  $f_{max}$  smaller or equal to 87.5 c/m such that the amplitude of all spectral lines after it are smaller than 5% of PSD max. We found that 90% of the  $f_{max}$  values for BB (MD) muscle lies between 25.0-87.5 (15.6-87.5) c/m and 9.4-59.4 (9.4-46.9) c/m for approach 1 and 2 respectively.

### **Introduction**

The monopolar sEMG signals sampled from a grid of electrodes can be shown as series of maps (MxN) where each pixel in each instantaneous map represents either the instantaneous amplitude of the signal at that channel or its root mean square value over a selected time window (RMS map). The signals are affected by three grid-related factors (see Figure 1): a) the size of the electrodes, b) the inter-electrode distance (IED), and c) the size of the grid. The effect of the size of the electrodes on the power of each map of the recorded sEMG has been discussed in Chapter 5. In this chapter and the following chapter, the effect of the IED will be discussed.

In the time domain, 95% of the signal's power is within 20-500Hz [1], [2]. Therefore, the sEMG signal in time is sampled at least at 1kHz (2048Hz in this work). However, the spatial bandwidth  $f_{max}$  of sEMG signals is still unknown. Knowing the spatial bandwidth of the sEMG signals is important because it can be used to define an optimal IED needed to record the sEMG without losing any information.

The Fourier transform is a useful tool to analyze the spatial frequency component of a multichannel sEMG signals. A detailed explanation about it can be found in many writings, some of which are mentioned in the references at the end of this chapter. In this work, we will describe briefly the fundamental theory of the Fourier transform.

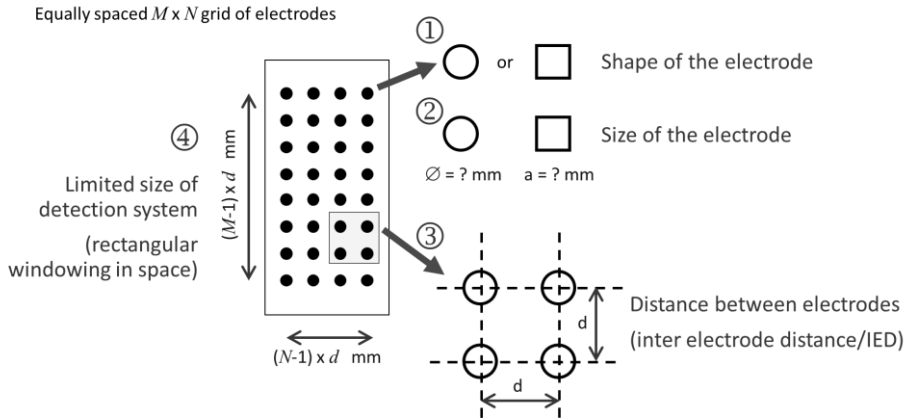


Figure 1. Issues of sEMG recording using a grid of electrode: 1) shape of the electrode, 2) size of the electrode, 3) inter-electrode distance, and 4) size of detection systems.

Any signal satisfying Dirichlet conditions [3] can be described as a finite summation of sine functions. In the case where the signal is periodic, this summation is shown as a Fourier series. In the other case, a Fourier transform can be used to decompose the signal into its sinusoidal component with a residual error. By using this mathematical technique, we assume that the signal is periodic with the period approaching infinity. Let us consider a one-dimensional continuous signal  $x(t)$  with infinite length and periodic with period  $T_p$ , the Fourier transform of this signal can be written as [4]

$$c_k = \frac{1}{T_p} \int_{T_p} x(t) e^{-j2\pi F_o t} dt \quad (1)$$

where  $c_k$  is a complex value defined as the Fourier coefficients. Thus, the signal can be represented in a Fourier series, that is,

$$x(t) = \sum_{k=-\infty}^{\infty} c_k e^{j2\pi k F_o t} \quad (2)$$

The harmonics obtained from the Fourier transform are represented in the frequency domain by a series of delta functions as shown in Figure 2.

We can extend the Fourier transform expressed in (1) for a two-dimensional continuous signal. Given  $u$  and  $v$  as spatial frequencies in the  $x$  and  $y$  direction respectively, the 2D Fourier transform can be written mathematically as

$$F(u, v) = \int_{-\infty}^{\infty} \int_{-\infty}^{\infty} f(x, y) e^{-j2\pi(ux+vy)} dx dy \quad (3)$$

The harmonics obtained from the Fourier transform are represented in the frequency domain by a *bed-of-nails* of delta function in a spatial frequency domain as shown in Figure 3.

A continuous-time signal with the highest frequency (bandwidth) B Hz can be uniquely recovered from its samples if the sampling rate in time  $f_s$  is greater than two times B per second. This theorem is known as the Shannon-Nyquist theorem. If the sampling rate is smaller than the required sampling rate, we cannot reconstruct the original signal from its samples. In the frequency domain, this phenomenon can be seen as a multiple folding of the frequency (see Figure 4).

The Shannon-Nyquist theorem is also applicable on a 2D signal or image. Given  $u$  and  $v$  as frequency component in  $x$  and  $y$  direction respectively. A continuous, band-limited function can be recovered with no error from a set of its samples if the sampling intervals are satisfy following conditions.

$$\Delta x < \frac{1}{2u_{\max}} \text{ and } \Delta y < \frac{1}{2v_{\max}} \tag{4}$$

Aliasing due to under-sampling in the space of a 2D signal or an image is known as spatial aliasing. Similar to the aliasing of the 1D signal, the spatial aliasing in frequency domain appears as an overlapping frequency component as shown in Figure 5.

The sEMG signals obtained by a grid of electrodes at an instantaneous time can be considered as a map or image, whereby its frequency component can be analyzed using the Fourier, transform. The results of this transformation can be used to compute the spatial frequency bandwidth of the sEMG map and determine the optimal IED.

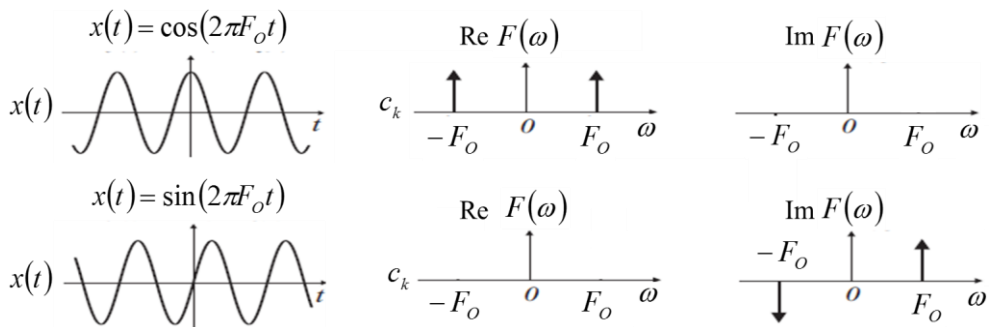
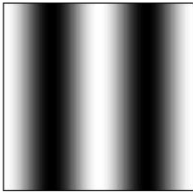


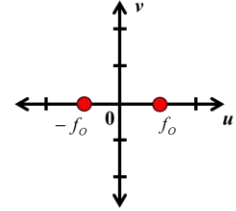
Figure 2. This figure demonstrates two examples of Fourier transform on the 1D continuous signal. The frequency components of the signal are represented in the frequency domain by a delta function.

A) 2D signal oscillating along X-axis

$$f(x, y) = \cos(2\pi f_o x)$$

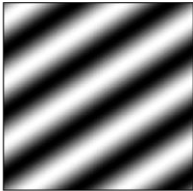


$$\begin{aligned} & F \{ \cos(2\pi f_o x) \} \\ &= F \left\{ \frac{e^{j2\pi f_o x} + e^{-j2\pi f_o x}}{2} \right\} \\ &= \frac{1}{2} \iint \left[ e^{j2\pi f_o x} + e^{-j2\pi f_o x} \right] e^{-j2\pi(u x + v y)} dx dy \\ &= \frac{1}{2} [\delta(u - f_o) + \delta(u + f_o)] \end{aligned}$$

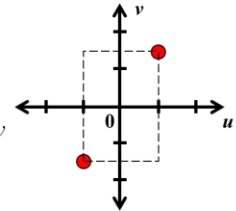


B) 2D signal oscillating at certain angle

$$f(x, y) = \sin(2\pi x + 2\pi(3/2)y)$$

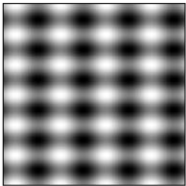


$$\begin{aligned} & F \{ \sin(2\pi x + 2\pi(3/2)y) \} \\ &= F \left\{ \frac{e^{j2\pi(x+(3/2)y)} - e^{-j2\pi(x+(3/2)y)}}{2j} \right\} \\ &= \frac{1}{2j} \iint \left[ e^{j2\pi(x+(3/2)y)} - e^{-j2\pi(x+(3/2)y)} \right] e^{-j2\pi(u x + v y)} dx dy \\ &= \frac{1}{2j} [\delta(u - 1, v - 3/2) - \delta(u + 1, v + 3/2)] \end{aligned}$$

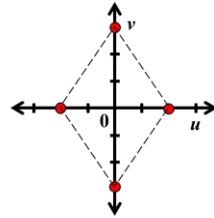


C1) 2D signal oscillating in both directions (x and y)

$$f(x, y) = \sin(2\pi 2x) + \cos(2\pi 3y)$$



$$\begin{aligned} & F \{ \sin(4\pi x) + \cos(6\pi y) \} = F \{ \sin(4\pi x) \} + F \{ \cos(6\pi y) \} \\ &= \frac{1}{2j} [\delta(u - 2, v) + \delta(u + 2, v)] + \frac{1}{2} [\delta(u, v - 3) + \delta(u, v + 3)] \end{aligned}$$



C2) 2D signal oscillating in both directions(x and y)

$$f(x, y) = \sin(2\pi 5x) \sin(2\pi 3y)$$



$$\begin{aligned} & F \{ \sin(2\pi 5x) \sin(2\pi 3y) \} \\ &= -\frac{1}{4} \iint \left[ e^{j2\pi 5x} - e^{-j2\pi 5x} \right] \left[ e^{j2\pi 3y} - e^{-j2\pi 3y} \right] e^{-j2\pi(u x + v y)} dx dy \\ &= -\frac{1}{4} [\delta(u - 5, v - 3) - \delta(u + 5, v + 3) + \delta(u - 5, v + 3) - \delta(u + 5, v - 3)] \end{aligned}$$

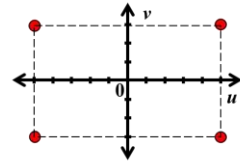


Figure 3. The Fourier components of 2D Fourier Transform are represented inside a plane. Several cases of signals in 2D are represented. The Fourier components might only lay on one axis (A), inside two quadrants (B), on both axis (C1), or all of the quadrants (C2) depending on the function used to generate the signal. In all cases, we can see that the Fourier components are symmetric through the origin (0,0) [5]. All signals extend from  $-\infty$  to  $\infty$  in both directions.

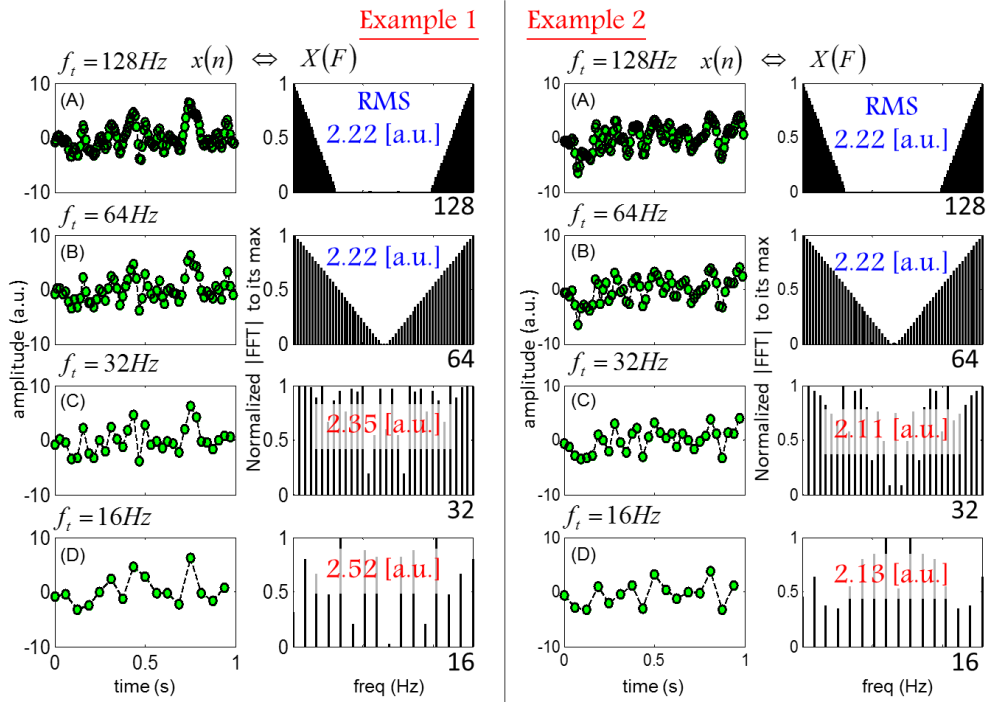


Figure 4. This figure shows two examples of one dimensional signals constructed from 30 sinusoidal signals (1-30Hz, random phase:  $-\pi/4$  to  $\pi/4$ ) sampled with enough sampling frequency ( $f_{s,t}=128\text{Hz}$ ) showing a clear separation of the magnitude of the Fourier transform between the positive and its mirror frequency, i.e. there is no aliasing (A). Although the sampling frequency is low, as long as it still satisfies the Nyquist theorem ( $f_{s,t}>2B$ ) we can still have a signal which is free from aliasing (B). When the sampling frequency no longer satisfies the Nyquist theorem (C), signal aliasing occurs. This aliasing in frequency domain appears as an overlap between the positive and its mirror frequency. A lower sampling frequency (D) results in a greater effect of aliasing, which prevents us to reconstructing the original continuous signal and its amplitude. As shown in the figure, the amplitude feature (RMS value) of the signal could be lower or higher than the original signal.

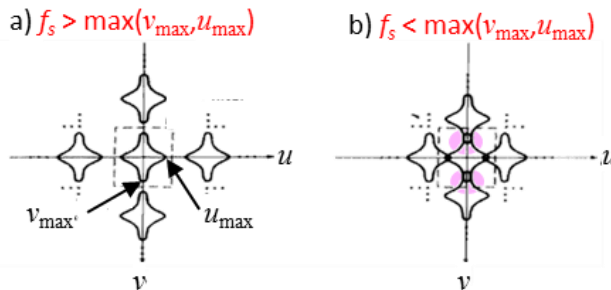


Figure 5. Figure a shows the Fourier transform of an image with correct sampling. Overlaps of the spectral periods appear in the undersampled image (b) and it becomes impossible to isolate a single spectral period. This figure is depicted from [6].



## Materials and methods

*Experimental procedure.* Surface EMG monopolar signals were recorded for 30s using a grid of electrodes (16x8,  $\varnothing=1\text{mm}$ , IED=5mm, sampled in time at 2048Hz). The grid was placed on: a) the short head of biceps brachii (BB) of a subject holding 4Kg in 90° elbow flexion, and b) the medial deltoid (MD) of a subject holding 4Kg in 90° abduction (see Figure 6). The skin was abraded and rinsed with water before attachment of the grid. The 5mm IED is equal to a spatial sampling frequency ( $f_s$ ) of 200 cycles/m (c/m).

*Signal processing.* Bandpass filtering (20-500 Hz, 2<sup>nd</sup> order Butterworth zero phase filter), power line interference attenuation (by spectral interpolation [7]), bad channel removal, and offset removal in time were performed. The central 15s of the signals (30720 samples) were processed. Signal processing was performed with MATLAB.

*Spatial bandwidth determination.* The sEMG bandwidth ( $f_{\text{max}}$ ) depends on how such frequency is defined. To provide such definition, the sEMG sampled in space at  $f_s > 2f_{\text{max}}$  must be available. In other words, we cannot estimate the spatial bandwidth of the sEMG maps that have “spatial aliasing”, i.e. maps whose frequency components near  $f_s/2$  are overlapping. The source of aliasing could be either the high frequency component of the map itself or the noise introduced by electrode-skin contact.

We assume that each instantaneous monopolar map is the superposition of the true sEMG map and a 2D uncorrelated random noise. Therefore, the power spectral density ( $\text{PSD}_{\text{tot}}$ ) of the recorded signals is the sum of the sEMG and noise PSDs. Both PSDs are unknown. Then to determine the “correct” bandwidth, we establish two approaches: 1)  $f_{\text{max}}$  based on 90% power, and 2)  $f_{\text{max}}$  based on the power of the harmonics.

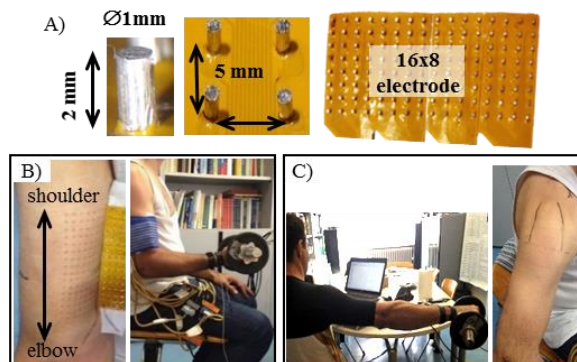


Figure 6. The grid of electrodes (A) was placed on: B) the short head of biceps brachii of a subject and C) the medial deltoid of a subject See text for details.

1) **Approach 1**  $f_{\max}$  based on 90% power

Two premises used in this approach are: each of the maps is wide sense stationary and is affected by a white Gaussian noise. Therefore, a 3 by 3 pixelwise adaptive Wiener filter is applied to each of the recorded maps (see reference [8] for a detailed discussion about the 2D Wiener filter). Then, the Fourier transform with zero padding in space (62 by 64 points) is performed for each map without removing the DC component of the map. The spatial frequency resolution is 3.125 c/m.

We analyze the first quadrant ( $+f_{x1}, +f_{y1}$ ) and the fourth quadrant ( $+f_{x2}, -f_{y2}$ ). We find  $f_{x1}, f_{y1}, f_{x2}$ , and  $f_{y2}$  such that the sum of the PSD harmonics reaches 90% of the total power in both quadrants.

$$P_i(f_{x1}, f_{y1}, f_{x2}, f_{y2}) = \sum_{u1=0}^{f_{x1}} \sum_{v1=0}^{f_{y1}} \sum_{u2=0}^{f_{x2}} \sum_{v2=0}^{f_{y2}} \left[ |c_i(u1, v1)|^2 + |c_i(u2, -v2)|^2 \right] \quad (5)$$

where  $c_i$  is the Fourier coefficient while  $P_i$  is the power of each map at the time sample  $i$  computed up to the spatial frequencies ( $f_{x1}, f_{y1}$ ) for the first quadrant and up to the spatial frequencies ( $f_{x2}, f_{y2}$ ) for the fourth quadrant. The total power in both quadrants is obtained when  $f_{x1}, f_{x2}, f_{y1}$ , and  $f_{y2}$  are equal to 100 c/m. If there is more than one combination of the four frequencies, the one with the largest  $f_x$  or  $f_y$  is considered. Then we define  $f_{\max-P}$  as the highest value among  $f_{x1}, f_{y1}, f_{x2}$ , and  $f_{y2}$ . Maps whose  $f_{\max-P}$  is greater than 87.5 c/m are categorized as maps with “spatial aliasing” (**definition 1**) and they are excluded from further analysis (see Figure 7).

2) **Approach 2**  $f_{\max}$  based on the power of the harmonics

In this approach, we hypothesize that each of the maps is affected by white gaussian noise whose amplitude of the power of each harmonic is equal to 5% of the maximum PSD value.

Similar to the first approach, we perform the Fourier transform with zero padding in space (64x64 points), such that we obtain spatial frequency resolution of 3.125 c/m. Then we compute the PSD of each monopolar map.

The power of the harmonics in the first and fourth quadrants are analyzed to find  $f_{x1}, f_{y1}, f_{x2}$ , and  $f_{y2}$  such that the power of each harmonic located after those spatial frequencies is less than 5% of the maximum PSD value.

Then we define  $f_{\max-A}$  as the highest value among  $f_{x1}, f_{y1}, f_{x2}$ , and  $f_{y2}$ . Maps whose  $f_{\max-A}$  are greater than 87.5 c/m are categorized as maps with “spatial aliasing” (**definition 2**) and they are excluded from further analysis.

## Results and discussion

Reconstruction and feature estimation of the sampled map are possible without error if the spatial sampling frequency satisfies the Nyquist-Shannon sampling theorem.

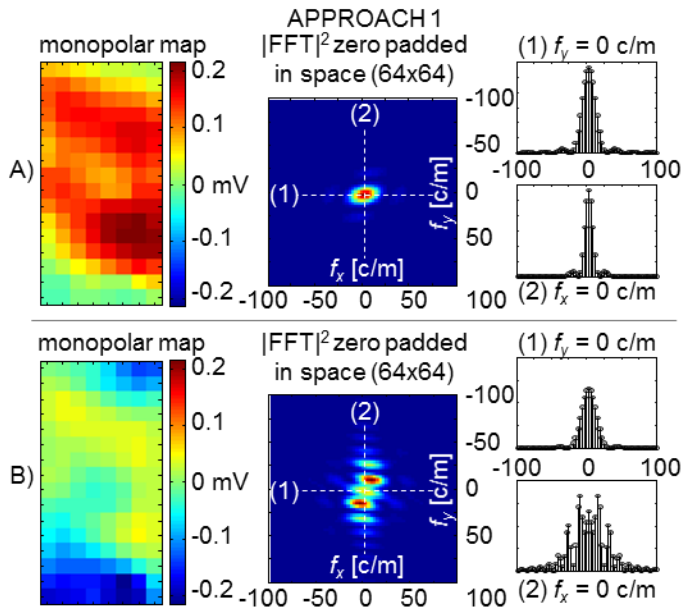


Figure 7. Image A) shows an example of map, after 3x3 Wiener filtering, that satisfies definition 1 of spatial bandwidth:  $(f_{x1}, f_{y1})$  and  $(f_{x2}, f_{y2})$  below 87.5 c/m, while image B) does not.

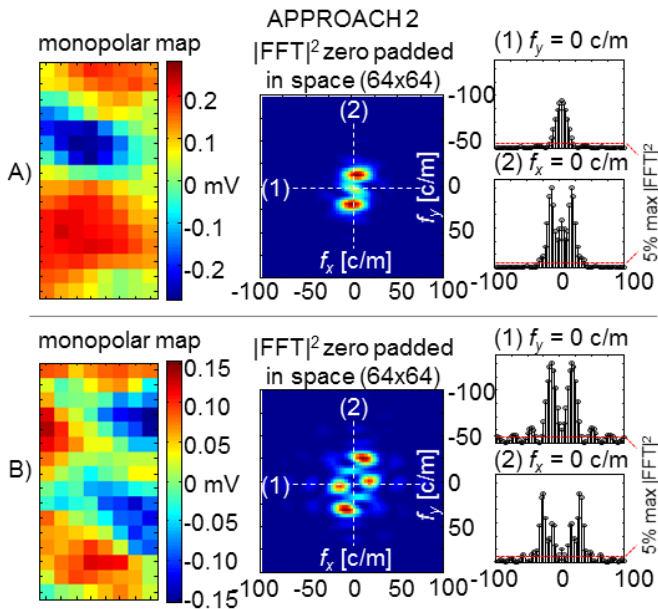


Figure 8. Image A) shows an example of map that satisfies definition 2 of spatial bandwidth:  $f_{max}$  below 87.5 c/m, while image B) does not.



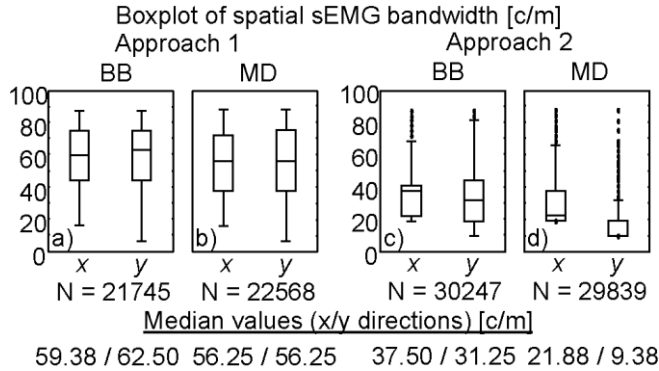


Figure 9. Spatial bandwidth of  $N$  out of 30720 maps obtained from two muscles: BB and MD. Panels a) and b) show a boxplot of spatial sEMG bandwidths obtained using Approach 1. Panels c) and d) show boxplot of spatial sEMG bandwidths obtained using Approach 2.

According to the first approach, 90% of  $f_{max-P}$  values for BB muscle lies in the range of 25.0-87.5 c/m while for MD muscle lies in the range of 15.6-87.5 c/m. In addition, for each BB and MD muscle, 71% and 74% of 30720 maps show no “aliasing” respectively (Figure 9). According to the second approach, 90% of  $f_{max-A}$  values for BB muscle lies in the range of 9.4 – 59.4 c/m while the MD muscle lies in the range of 9.4 – 46.9 c/m. We found that 98% of the 30720 maps for both BB and MD muscles show no “aliasing”.

Approach 2 provides lower estimates of  $f_{max}$  and a greater percentage of maps whose  $f_{max}$  is smaller or equal to 87.5 c/m. If Approach 2 is adopted, IED=5mm would be acceptable for 97% of the maps from BB and MD muscles. If Approach 1 is adopted IED=5mm would be acceptable for 71% of the instantaneous sEMG monopolar maps from BB and MD muscles.

The evidence that Approach 2 provides lower estimates than Approach 1 can be explained as follows. Given two continuous one-dimensional signals, the first signal has a power spectrum that resembles a triangular shape with no tail (see Figure 10A). The second signal has a power spectrum which has a steep decreasing slope until a certain frequency where its amplitude is equal to the 5% of the maximum PSD ( $H^2$ ) then gradually decreasing and forming a long tail (see Figure 10B).

- A) Case 1: the power spectrum of the signal has a triangular shape with no tail  
The total power of the whole signal is the area under the plot.

$$P_{tot} = \frac{1}{2} \cdot f_{last} \cdot H^2 \quad (6)$$

Lets  $f_A$  be the frequency harmonic whose power equal to 5% of the maximum PSD ( $H^2$ ). Thus, the total power of the harmonics between  $f_A$  and  $f_{last}$  is computed as follows.

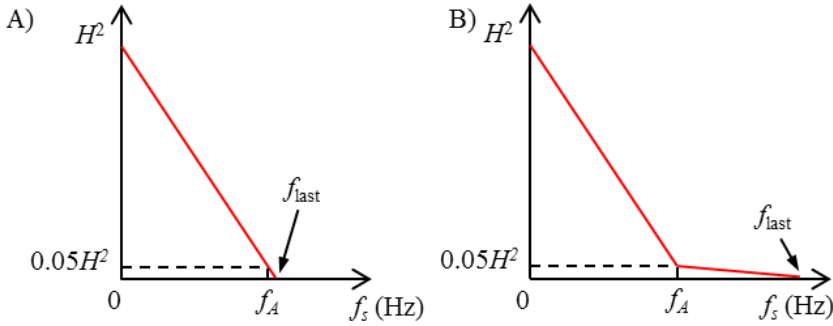


Figure 10. These are three example of power spectral shape that might give different results for approach 1 and approach 2.

$$P_{f_A \text{ to } f_{\text{last}}} = \frac{1}{2} (f_{\text{last}} - f_A) \cdot 0.05 \cdot H^2 \quad (7)$$

By substituting (6) to (7) we obtain

$$P_{f_A \text{ to } f_{\text{last}}} = \frac{(f_{\text{last}} - f_A)}{f_{\text{last}}} \cdot 0.05 \cdot P_{\text{tot}} \quad (8)$$

In consequence, the total power of the harmonics between  $f_A$  and  $f_{\text{last}}$  will be always smaller than 5% of the whole signal's power. Furthermore, we can infer that the  $f_{\text{max}}$  obtained by the Approach 1 will always lower than Approach 2 because Approach 1 maintains the total power of the harmonics between  $f_A$  and  $f_{\text{last}}$  equal to 10% of the  $P_{\text{tot}}$ .

- B) Case 2: the power spectrum of the signal has steep decreasing slope until a certain frequency where its amplitude is equal to the 5% of the maximum PSD ( $H^2$ ) then gradually decreasing and forming a long tail  
The total power of the whole signal is the area under the plot.

$$P_{\text{tot}} = \frac{1}{2} \cdot f_A \cdot 0.95H^2 + 0.05 \cdot f_A \cdot H^2 + \frac{1}{2} \cdot (f_{\text{last}} - f_A) \cdot 0.05H^2 \quad (9)$$

Then, the total power of the harmonics between  $f_A$  and  $f_{\text{last}}$  is computed as follows.

$$P_{f_A \text{ to } f_{\text{last}}} = \frac{1}{2} (f_{\text{last}} - f_A) \cdot 0.05 \cdot H^2 \quad (10)$$

By substituting (9) to (10) we obtain

$$P_{f_A \text{ to } f_{\text{last}}} = \frac{f_{\text{last}} - f_A}{0.05f_{\text{last}} + f_A} \cdot 0.05 \cdot P_{\text{tot}} \quad (11)$$

If  $f_{\text{last}}$  is equal to 2.1 times  $f_A$ , then the total power of the harmonics between  $f_A$  and  $f_{\text{last}}$  will be equal to 5% of  $H^2$ . If  $f_{\text{last}}$  is less than 2.1 times  $f_A$ , the total power of the harmonics between  $f_A$  and  $f_{\text{last}}$  it will be less than 5% of  $H^2$ . In other conditions, the total power of the harmonics between  $f_A$  and  $f_{\text{last}}$  will be greater than 5% of  $H^2$ .

In this case, the  $f_{\text{max}}$  obtained by the Approach 1 could be lower or higher or equal to that obtained by Approach 2 depending on the frequency components of the map.

### Conclusion

The issue of inter electrode distance is important in many applications such as sEMG RMS estimation or signal decomposition. To estimate its spectral domain features a signal must be sampled at  $f_s$  greater than  $2f_{\text{max}}$ . This requires knowledge of its  $f_{\text{max}}$ , which is not available. Estimating  $f_{\text{max}}$  when it is near  $f_s/2$  requires approximations and assumptions. We provide two approaches with their corresponding results obtained from one BB and one MD muscle. Based on the fact that the second approach depends on the length of the power spectrum's tail, approach 1 is recommended to be used.

More work is required to obtain consensus on the IED that would provide an acceptable compromise between cost of the electrode system and information loss.

**REFERENCES**

- [1] J. S. Karlsson, K. Roeleveld, C. Grönlund, A. Holtermann, N. Ostlund, and P. T. R. S. A., “Signal processing of the surface electromyogram to gain insight into neuromuscular physiology,” *Philos. Trans. R. Soc. A*, vol. 367, no. 1887, pp. 337–356, 2009.
- [2] R. Merletti and P. A. Parker, *Electromyography: physiology, engineering, and non-invasive applications*, vol. 11. John Wiley & Sons, 2004.
- [3] A. Antoniou, *Digital Signal Processing, Signals, Systems and Filters*. McGraw-Hill, 2006.
- [4] J. G. Proakis and D. G. Manolakis, *Digital Signal Processing (3rd Ed.): Principles, Algorithms, and Applications*. Upper Saddle River, NJ, USA: Prentice-Hall, Inc., 1996.
- [5] J. W. Woods, *Multidimensional signal, image, and video processing and coding*. Academic press, 2011.
- [6] R. C. Gonzalez and R. E. Woods, *Digital Image Processing*, 3rd ed. Prentice-Hall, 2008.
- [7] D. T. Mewett, K. J. Reynolds, and H. Nazeran, “Reducing power line interference in digitised electromyogram recordings by spectrum interpolation,” *Med. Biol. Eng. Comput.*, vol. 42, pp. 524–531, 2004.
- [8] J. S. Lim, “Two-dimensional signal and image processing,” *Englewood Cliffs, NJ, Prentice Hall, 1990, 710 p.*, vol. 1, 1990.

# **Chapter VII**

*Effect of inter-electrode  
distance on RMS  
amplitude estimation*



## Effect of inter-electrode distance on RMS amplitude estimation

*Adapted from:*

*Soedirdjo S.D.H., Afsharipour B., Cattarello P., Merletti R. Errors in RMS amplitude estimation attributable to the Inter-Electrode Distance of the surface EMG electrode grids. "XXI Congress of The International Society of Electrophysiology and Kinesiology", Chicago, United States, July 5-8, 2016. Accepted*

### Abstract

The estimated spatial amplitude (spatial RMS) and reconstructed map of muscle activity from the recorded sEMG signals is affected by physical dimension of the electrodes (size and shape), size of the grid, and the inter-electrode distance (IED). We focus on the effect of IED on the spatial RMS. The effect of IED on spatial RMS estimation was investigated using the 30s monopolar sEMG signals sampled in space using a grid of pin electrodes (16x8;  $\varnothing=1\text{mm}$ , IED = 5mm, 200 samples/m,) and sampled in time at 2048 Hz. The grid was placed on short head of biceps brachii (BB) and medial deltoid (MD). Then, the central 30720 instantaneous map (15s) were processed. To reduce the likelihood of heavy aliasing, the Fourier transform with zero padding in space (64x64 points, 3.125 cycles/m resolution) was performed for all maps without removing the offset of each map. Maps in which at least one row or column showed more than 10% of its power above 87.5 cycles/m were excluded. The remaining maps were kept for reconstructing high-resolution maps as reference maps (0.1mm IED) by using 2D Sinc function.

Maps with larger IED were obtained by down sampling the reference maps while maintaining the area. We computed: 1) the spatial RMS of each sEMG map, 2) the mean of the spatial RMS values over a 1s period for 15s and 3) the RMS of each channel in the 1s period and then the spatial mean over all channels. Larger IEDs result in loss of details in the sEMG maps and cause an error in spatial RMS estimation (RMSE). We found that the spatial RMSE could reach up to 18% and 9% for BB and MD muscles respectively. However, when the RMS of the map is computed in 1s epoch, the RMSE is negligible.

### Introduction

Muscle activities can be recorded as electric potentials through one or more electrodes placed on the skin over the targeted muscle, called as surface electromyogram (sEMG) [1]. It is well known that the recorded sEMG signal is affected by electrode location with respect to the innervation zones (IZ), inter-electrode distance (IED), and electrode physical dimension. A single differential (SD) sEMG signals obtained from electrodes near the IZ has a lower amplitude

(see Figure 1) and higher power spectral frequency compares to the SD signals obtained from the other part of the muscle except the tendon area [2], [3]. For this reason, to obtain a complete representation of muscle activity, multi-channel sEMG systems such as linear electrode arrays [4] or grid of electrodes [5] is suggested.

Linear electrode arrays can be used to estimate muscle fiber conduction velocity (CV) and determine the location of innervation zones and tendons. On the other hand, a grid of electrodes allows the user to demonstrate the spatial distribution of sEMG over the skin surface above a single muscle [5] and enhance the prediction of IZ location and estimation of CV and it can be used to predict the length and orientation of the muscle fiber [6]. In addition, the sEMG signals obtained by a grid of electrodes are useful for sEMG signal decomposition.

The multi-channel sEMG systems solve the issue about electrode location. However, the recorded signals are still affected by three factors: a) size of the electrodes (see Chapter 5), b) the IED, and c) the size of the grid. In this study, we will focus on the effect of IED on the amplitude estimation of sEMG signals obtained with a grid of electrodes.

Larger IED has been shown to decrease motor unit potential contribution to the recorded surface electromyography recorded with a grid of electrodes [7]. Moreover, larger IED is demonstrated to increase the time-averaged rectified value (t-ARV) of the signals recorded not only with bipolar electrodes placed on the *frontalis* muscle [8] but also the t-ARV of the single differential signals recorded with an array of electrodes placed on jaw elevator muscles [9] and human upper trapezius muscle [10]. Larger IED also increase the root mean square (RMS) values computed in 1s epoch of sEMG signals recorded from *vastus lateralis* with bipolar configuration [11].

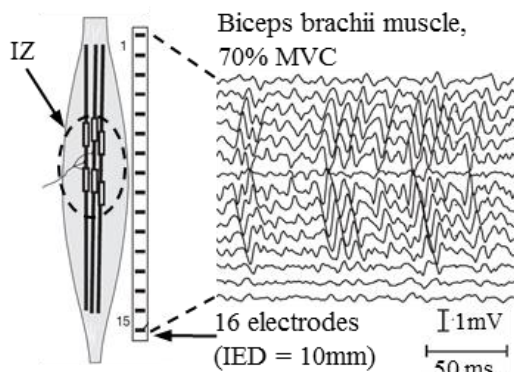


Figure 1. The single differential signal obtained from biceps brachii muscle contracted at 70% MVC shows that the amplitude of the signals is lower at the IZ. The image was taken from [1].



The investigations mentioned above evaluate the effect of IED on the bipolar electrode configuration and a linear array of electrodes, but not a grid of electrodes. The monopolar sEMG signals sampled from a grid of electrodes can be shown as series of maps ( $M \times N$  pixel) where each pixel in each instantaneous map represents either the instantaneous amplitude of the signal at that channel or its root mean square value over a selected time window (RMS map). Large IED could introduce aliasing (see Chapter 6) which implies on disabilities to reconstruct the continuous distribution of muscle activity and loss of information. Investigation on the simulated sEMG maps of a monopolar potential distribution (superficial single muscle fiber or motor unit action) proves that larger IED tends to increase the error of sEMG amplitude estimation [12]. However, since that in the practical situation there is millions of muscle fibers activated, it is interesting to see the effect of the IED on the recorded sEMG signals.

## Materials and methods

*Experimental procedure.* The 30s surface EMG monopolar signals were recorded using a grid of electrodes (16x8,  $\varnothing=1\text{mm}$ , IED=5mm, sampled in time at 2048Hz). The grid was placed on a) short head of biceps brachii (BB) of a subject holding 4Kg in 90° elbow flexion, and b) medial deltoid (MD) of a subject holding 4Kg in 90° abduction (see Figure 2). The grid was placed on the skin after slightly abrading the skin with abrasive paste (Nuprep; Weaver and Company, USA) and cleaning it with water.

*Signal processing.* Bandpass filtering (20-500 Hz, 2<sup>nd</sup> order Butterworth zero phase filter), power line interference attenuation using spectral interpolation [13], bad channel removal, and offset removal in time were performed. The central 15s of the signals (30720 samples) were processed. Signal processing was performed with MATLAB. Then we adopt **Approach 1** presented in Chapter 6 to determine which map has aliasing. Maps with “aliasing”, i.e. maps whose  $f_{max}$  is greater than 87.5 cycle/m, are excluded from further analysis.

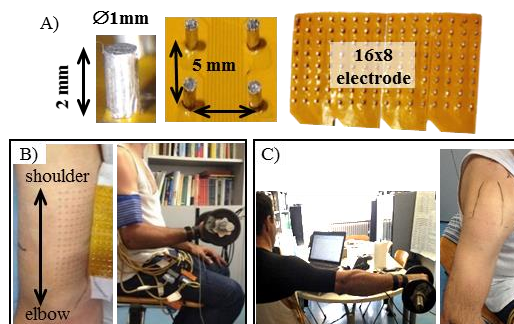


Figure 2. The grid of electrodes (A) was placed on B) the short head of biceps brachii of a subject and C) medial deltoid of a subject See text for details.

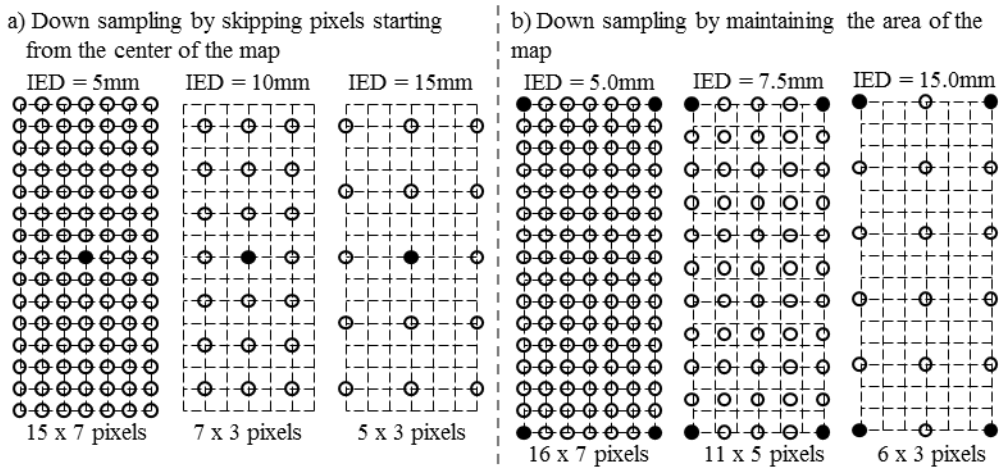


Figure 3. Downsampling a map can be done by a) skipping pixels starting from the center of the map, or b) down sampling the map while maintaining the area.

*Downsampling the sEMG maps.* Each of the “alias free” maps is interpolated with a 2D Sinc function to obtain a set of reference maps sampled with 10,000 samples/m. Then, these reference maps are down sampled in space to simulate the different IED. There are two ways to downsampling a map:

- 1) Downsampling by skipping electrodes from the center of the map [12].  
The pixel located at the center of the map is considered as a reference point which is always included in the maps down sampled for different IED. Then the other pixels are selected by skipping pixels starting from the reference point. (see Figure 3a). The advantage of this method is the ability to simulate IED with size multiple of the pixel's size (1000/spatial sampling frequency in c/m). However, if the total area of the skin covered by the electrodes is defined by the boundary formed by the outer electrodes, the coverage area of the simulated grid of electrodes is changing and depends on the IED.  
In the signal processing point of view, the size of the electrode's grid means the size of a 2D windowing function which is applied to the 2D signal. Therefore this downsampling method introduces a different windowing effect for each IED.
- 2) Down sampling while maintaining the coverage area of the electrodes  
In this approach, the four corner electrodes are maintained for different IED resulting in equal coverage area (see Figure 3b). Even so, the number of IED that can be simulated is limited since the number of selected pixels need to be an integer value. In contrast with the first method, since we maintain the size of the coverage area, the windowing effect is equal for each IED.

In this work, we adopt the second method to obtain eight sets of sEMG maps sampled with 10,000, 1,000, 666.67, 400, 333.33, 200, 133.33, and 66.67 samples/m.

*Calculating the Root Mean Square (RMS) value.* The activity of muscle can be recorded using a grid of electrode constructed from  $M$  by  $N$  electrode placed with equal distance in both vertical and horizontal directions (see Figure 4). At each instantaneous time  $t$ , we obtain a map whose value at each position is the instantaneous sample of each channel at the corresponding location  $(m,n)$ . The root mean square (RMS) value of the  $T$  samples in time and  $M$  by  $N$  samples in space of multichannel sEMG signals is defined in several ways described below.

1) Definition 1

The RMS value of multichannel sEMG signals at the  $k$ th time window (each time window consist of  $T$  samples) is the square root of the EMG power inside that time window. The power of sEMG signals can be computed in two ways:

- a) Compute the power in time and take the average of all values in space

By computing the power in time, we have a map where each pixel  $P(m,n)$  is the power of the signal for  $T$  samples in time at the corresponding location  $(m,n)$ .

$$P(m,n) = \frac{1}{T} \sum_{t=1}^T [S(m,n,t)]^2 \quad (1)$$

Then we take the average of all channels.

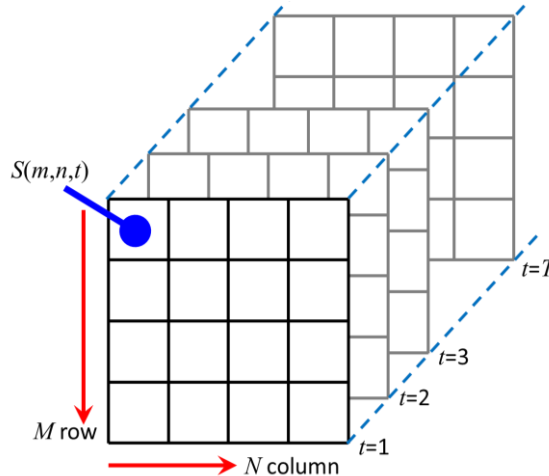


Figure 4. A multichannel sEMG signals can be shown as a series of map in time where the column and row of the map represent the location of the electrodes

$$\begin{aligned}
P_{\text{average in space}} &= \frac{1}{M} \sum_{m=1}^M \left[ \frac{1}{N} \sum_{n=1}^N P(m,n) \right] = \frac{1}{MN} \sum_{m=1}^M \sum_{n=1}^N P(m,n) \\
&= \frac{1}{MN} \sum_{m=1}^M \sum_{n=1}^N \left[ \frac{1}{T} \sum_{t=1}^T [S(m,n,t)]^2 \right] \\
&= \frac{1}{MNT} \sum_{m=1}^M \sum_{n=1}^N \sum_{t=1}^T [S(m,n,t)]^2
\end{aligned} \tag{2}$$

- b) Compute the power in space and take the average in time  
 By computing the power in space, for each instantaneous time  $t$  we have a value, which is the power of the instantaneous map.

$$P(t) = \frac{1}{MN} \sum_{m=1}^M \sum_{n=1}^N (S(m,n,t))^2 \tag{3}$$

Then we take the average of all time samples

$$\begin{aligned}
P_{\text{average in time}} &= \frac{1}{T} \sum_{t=1}^T P(t) \\
&= \frac{1}{T} \sum_{t=1}^T \left( \frac{1}{MN} \sum_{m=1}^M \sum_{n=1}^N (S(m,n,t))^2 \right) \\
&= \frac{1}{MNT} \sum_{m=1}^M \sum_{n=1}^N \sum_{t=1}^T [S(m,n,t)]^2
\end{aligned} \tag{4}$$

Both equations (2) and (4) show an identical result.

$$P_{\text{average in space}} = P_{\text{average in time}} = \frac{1}{MNT} \sum_{m=1}^M \sum_{n=1}^N \sum_{t=1}^T [S(m,n,t)]^2 \tag{5}$$

Then the RMS value at the  $k$ th time window is obtained as follow.

$$\begin{aligned}
Rl_k &= \sqrt{P_{\text{average in space}}} = \sqrt{P_{\text{average in time}}} \\
&= \sqrt{\frac{1}{MNT} \sum_{m=1}^M \sum_{n=1}^N \sum_{t=1}^T [S(m,n,t)]^2}
\end{aligned} \tag{6}$$

## 2) Definition 2

The RMS value of multichannel sEMG signals in one time window of  $T$  samples is the average in space over  $M$  by  $N$  samples of RMS value computed for each channel.

$$R2_k = \frac{1}{MN} \sum_{m=1}^M \sum_{n=1}^N \sqrt{\frac{1}{T} \sum_{t=1}^T [S(m,n,t)]^2} \quad (7)$$

## 3) Definition 3

The RMS value of multichannel sEMG signals in one time window of  $T$  samples is the average in time over  $T$  samples of RMS value computed in space over  $M$  by  $N$  samples for each time sample.

$$R3_k = \frac{1}{T} \sum_{t=1}^T \sqrt{\frac{1}{MN} \sum_{m=1}^M \sum_{n=1}^N [S(m,n,t)]^2} \quad (8)$$

Considering only one instantaneous map, the result obtained by (8) will be equal to (6) and smaller than (7). Furthermore, in the case of single map, definition 2 violates the concept of root mean square value since the result will be the mean of the values in space over  $M$  by  $N$  samples.

Then, for each set of maps obtained with different spatial sampling frequencies, we calculate the RMS values computed on each map as in Definition 3 (8). The next step is evaluating the effect of different spatial sampling frequencies ( $RMS_d$ ) by computing the relative RMS error ( $RMSE_n$ ) of the map at the  $n$ th sample with respect to the reference map sampled with 10,000 sample/m ( $RMS_{ref}$ ).

$$RMSE_n = \frac{RMS_d - RMS_{ref}}{RMS_{ref}} \times 100\% \quad (9)$$

Additionally, we also evaluate the relative RMS error ( $RMSE_g$ ) of the RMS value computed on each instantaneous map (8) for each IED ( $RMS_d$ ) and averaged within a groups of 1000 “alias-free” maps. The samples remainder of the grouping process were discarded.

$$RMSE_g = \frac{\overline{RMS_d} - \overline{RMS_{ref}}}{\overline{RMS_{ref}}} \times 100\% \quad (10)$$

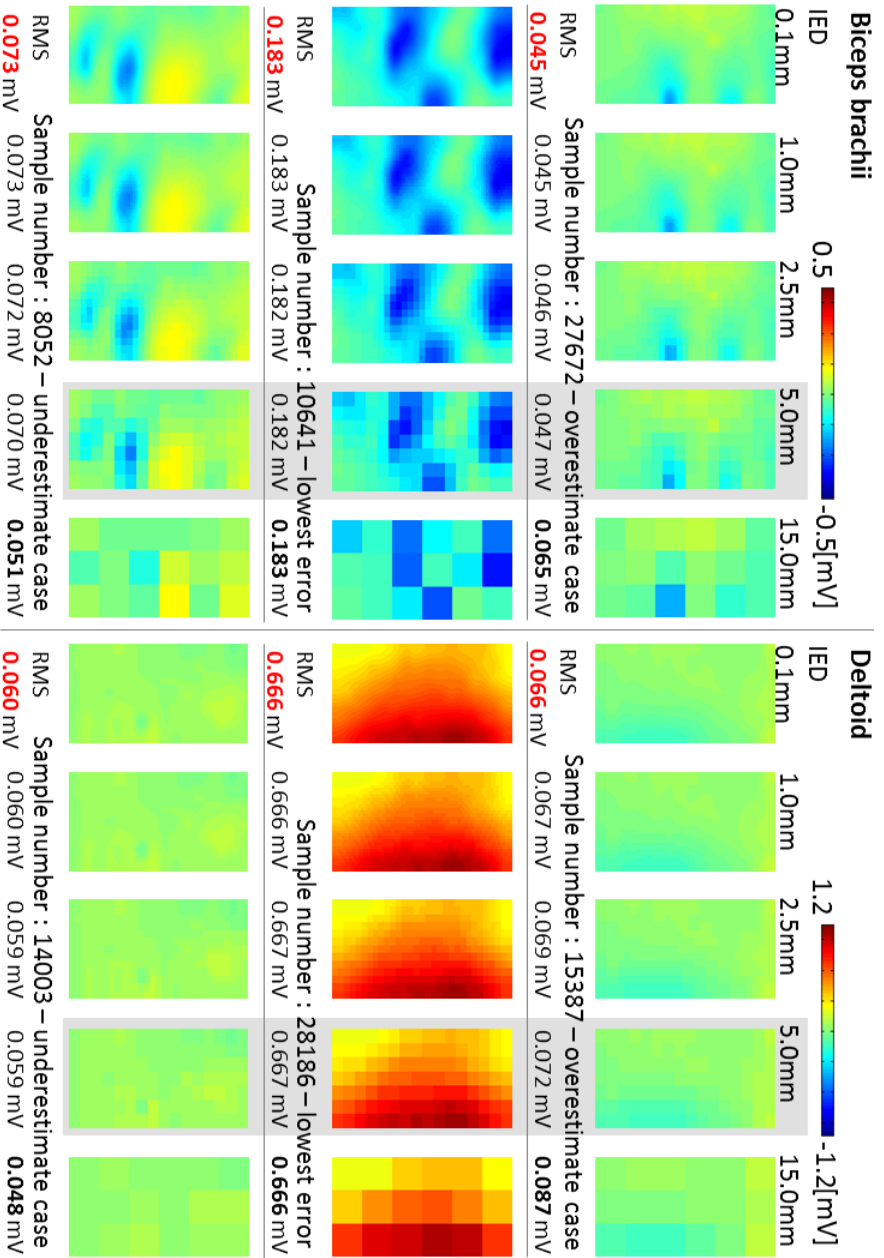


Figure 5 This figures show series of instantaneous time images obtained from biceps brachii and deltoid muscle sampled with different inter electrode distance. For an instantaneous time, different IED might either over estimate or under estimate the estimation of sEMG amplitude of the real value. Along with increasing distance between electrodes, the details of the image disappear.

## Results and discussion

The consequence of using larger IED is the loss of detail information which shows in the error on the estimation of RMS value. Figure 5 demonstrates that at one instantaneous time, different IED might give a different estimation of sEMG RMS value: overestimate, underestimate, or equal compared to the continuous map. One of the sources that cause these differences is the spatial aliasing (see **Chapter 6**). We adapt Approach 1 presented in Chapter 6 to obtain correct RMS calculation of the sEMG map. Then, exclude the maps which have “aliasing” and obtain 21745 maps for BB muscle and 22568 maps for MD muscle out of 30720 maps. Since the criterion of “aliasing” used in Approach 1 is very primitive and not necessarily correct in each case, the selected maps may not be all “alias-free”.

The RMS amplitude estimation error at the instantaneous time could reach up to  $\pm 18\%$  for map obtained from BB muscle sampled with 66.67 sample/m (equal to IED of 15mm) as shown in Figure 6. The same figure also suggests that for both BB and MD muscles, the errors of amplitude estimation are monotonically increased along with lower spatial sampling (larger IED) and it tends to underestimate the RMS amplitude estimation of the sEMG map. The median (interquartile range) of the RMS amplitude errors of the map obtained with 15mm IED is -1.2% (8.8%) for BB muscle and -2.1% (4.0%) for MD muscle.

Recall the Shannon-Nyquist theory which stated that a continuous 2D signal can be reconstructed from its sample without error if the sampling frequency in space greater than twice of its highest spatial frequency component. In other word, the RMS of the sampled 2D signal should be equal to the RMS of its continuous form. This is not in the case since the plot in Figure 6 shows that there are errors between the recorded sEMG map (IED 5mm) with the “reconstructed” map (IED <5mm) using 2D Sinc function. Thus, we can infer that the selected maps not really alias free which may caused by the noise of the map.

Boxplot of relative error between the RMS of each “alias-free” (at IED = 5mm) map resampled with different IED and RMS of the same map obtained with IED = 0.1mm [%]

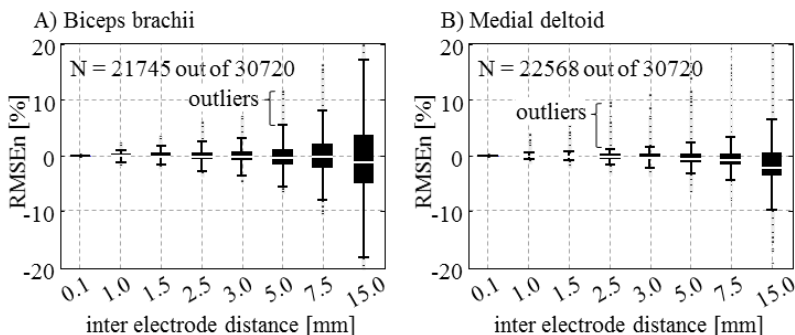


Figure 6. The RMS errors of maps obtained from biceps brachii (A) and medial deltoid (B) are increased along with greater IED. Up to IED of 5.0mm, the error is negligible (within a range of  $\pm 5\%$ ). There are errors between the recorded sEMG map (IED 5mm) with the “reconstructed” map (IED <5mm) using 2D Sinc function which implies that the selected maps not really alias free.

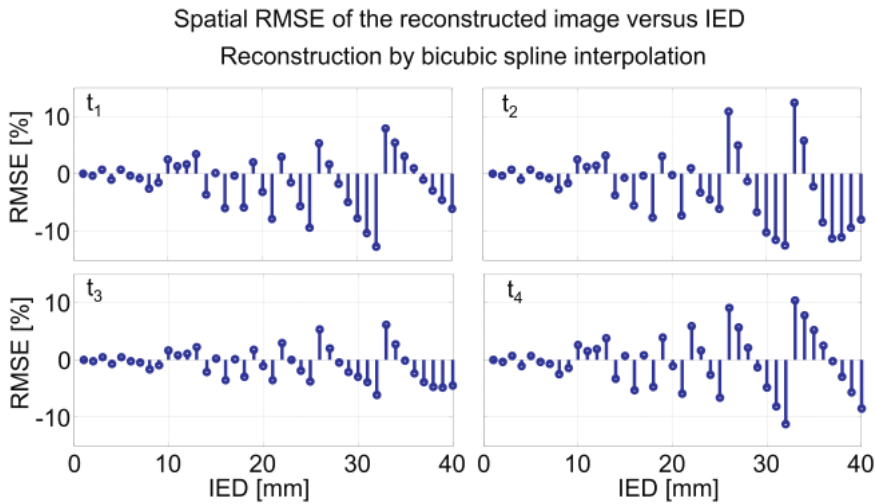


Figure 7. Spatial root mean square relative error RMSE [%] versus IED of the reconstructed image. The figure is reproduced from [12].

This finding is different from the results of the previous investigation using simulated monopolar sEMG map [12]. In their work, they assume that the detecting system is a grid of point like electrode with 1mm IED covering  $128 \times 128 \text{ mm}^2$  area of the skin. The EMG map obtained from this reference map (1mm IED) is down sampled up to 20mm IED starting from the central electrode towards the edges (see Figure 3a). Later on, they reconstruct the original map from its sampled map with bicubic spline. Then the two EMG amplitude indicators (average rectified value/ARV and root mean square/RMS) for different IED were computed. Furthermore, they compare these ARV and RMS values to the ARV and RMS values of the original simulated sEMG map with 1mm IED. They found that the spatial RMS errors ( $\text{RMSE}_n$ ) of the reconstructed map oscillate as the IED increases (see Figure 7). The oscillating RMSE might be due to changing of coverage area of the electrodes which implies different windowing effect (see Figure 3a). Greater sample size leads to smaller windowing effect, i.e. narrow power spectrum leakage in the frequency domain. In this study, the downsampling process of the map maintains the coverage area of the electrode grid thus the results are not affected by the changing of the area.

In addition, it is noticeable that the  $\text{RMSE}_n$  values of maps obtained from MD muscle are smaller than RMSE of BB muscle. Based on this evidence, we can infer that the sEMG map obtained from MD muscle is smoother (slow pixels variation) than those of BB muscle. A smooth sEMG map reflects low spatial frequency components which in line with the findings in Chapter 6 where the bandwidth of sEMG for MD muscle is lower than BB muscle (see Figure 9 in Chapter 6).



Then, we analyze the error in a group of maps ( $RMSE_g$ ). We take the maps without “aliasing”, i.e. 21745 maps from BB muscle and 22568 maps for MD muscle, and divide it into groups of 1000 maps. Thus, we obtain 21 groups and 22 groups of maps for BB and MD muscles respectively for each IED. The remaining samples are discarded. Then the average RMS value for each group is computed and the relative errors between the average RMS value obtained from each IED and the average RMS value obtained from maps (IED 0.1mm) were evaluated (10).

We found that the  $RMSE_g$  of the maps obtained from both muscles (BB and MD) are monotonically increases significantly ( $p < 0.05$ ) along with larger IED. However,  $RMSE_g$  shown in Figure 8 are smaller than the relative errors obtained from each map (see Figure 6) and negligible as they are smaller than 3% with respect to the RMS values of the maps resampled with 10,000 sample/m computed in the same way. While  $RMSE_n$  values show both positive and negative errors,  $RMSE_g$  values are all negative. This evidence can be explained as the results of averaging the RMS values in a group of maps.

Boxplot of relative errors of the spatial RMS computed for each “alias-free” map (at IED = 5mm) resampled with different IED and averaged within 1000 maps with respect to the averaged RMS of “alias-free” map obtained with IED = 0.1mm computed in the same way [%]

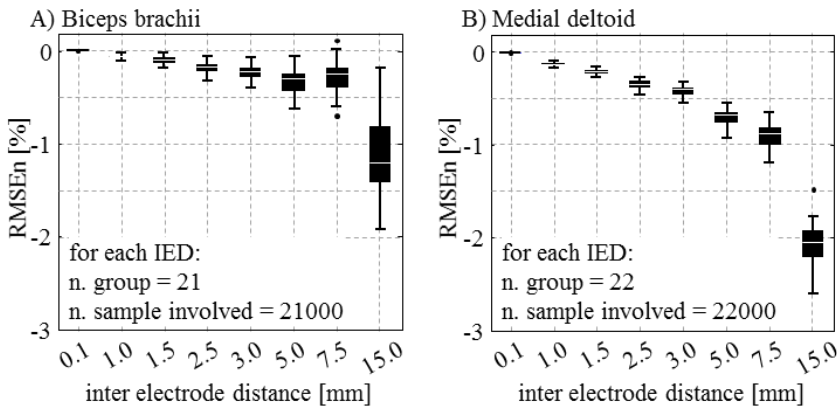


Figure 8. The relative error of the spatial RMS of sEMG “alias-free” map (at IED = 5mm) resampled with different spatial sampling and averaged within a group of 1000 maps with respect to the spatial RMS of the sEMG maps resampled at 10,000 sample/m computed in the same way. Larger IED tends to underestimate the amplitude of sEMG for signals. See text for detail.

**Conclusion**

Downsampling the instantaneous maps while maintaining the coverage area of the electrode resolves the issue of the different windowing effect that appears in the previous investigation [12]. Having the same windowing effect on each of the maps resampled with different spatial sampling (different IED) allow us to compare the results.

Larger IEDs result in loss of details in the sEMG maps and cause an error in spatial RMS estimation ( $RMSE_n$ ). We quantified the  $RMSE_n$  for IEDs ranging from 0.1mm to 15mm. For the maps with 15mm IED, the RMSE were  $\pm 18\%$  and  $\pm 9\%$  for BB and MD muscles respectively.

If we consider the average of spatial RMS in a group of samples, the error between these averaged values and the spatial RMS of the reference maps computed in the same way ( $RMSE_g$ ) is lower than 3%. Still, in specific applications such as differentiating signals or segmenting regions of activation in a muscle or activities of small muscles, small IED is recommended.

## REFERENCES

- [1] R. Merletti and P. A. Parker, *Electromyography: physiology, engineering, and non-invasive applications*, vol. 11. John Wiley & Sons, 2004.
- [2] A. Rainoldi, G. Melchiorri, and I. Caruso, “A method for positioning electrodes during surface EMG recordings in lower limb muscles,” *J. Neurosci. Methods*, vol. 134, no. 1, pp. 37–43, 2004.
- [3] S. H. Roy, C. J. De Luca, and J. Schneider, “Effects of electrode location on myoelectric conduction velocity and median frequency estimates.,” *J. Appl. Physiol.*, vol. 61, no. 4, pp. 1510–1517, 1986.
- [4] R. Merletti, D. Farina, and M. Gazzoni, “The linear electrode array: A useful tool with many applications,” *J. Electromyogr. Kinesiol.*, vol. 13, no. 1, pp. 37–47, 2003.
- [5] M. J. Zwarts and D. F. Stegeman, “Multichannel surface EMG: basic aspects and clinical utility.,” *Muscle Nerve*, vol. 28, no. 1, pp. 1–17, 2003.
- [6] R. Merletti, A. Botter, A. Troiano, E. Merlo, and M. A. Minetto, “Technology and instrumentation for detection and conditioning of the surface electromyographic signal: State of the art,” *Clin. Biomech.*, vol. 24, no. 2, pp. 122–134, 2009.
- [7] K. Roeleveld, D. F. Stegeman, H. M. Vingerhoets, and A. van Oosterom, “Motor unit potential contribution to surface electromyography,” *Acta Physiol. Scand.*, vol. 160, no. 2, pp. 175–183, 1997.
- [8] A. van Boxtel, P. Goudswaard, and L. R. B. Schomaker, “Amplitude and the Bandwidth of the Frontalis Surface EMG: Effects of Electrode Parameters.,” *Psychophysiology*, vol. 21, no. 6, pp. 699–707, 1984.
- [9] T. Castroflorio, D. Farina, A. Bottin, M. G. Piacino, P. Bracco, and R. Merletti, “Surface EMG of jaw elevator muscles: Effect of electrode location and inter-electrode distance,” *J. Oral Rehabil.*, vol. 32, no. 6, pp. 411–417, 2005.
- [10] D. Farina, P. Madeleine, T. Graven-Nielsen, R. Merletti, and L. Arendt-Nielsen, “Standardising surface electromyogram recordings for assessment of activity and fatigue in the human upper trapezius muscle,” *Eur. J. Appl. Physiol.*, vol. 86, no. 6, pp. 469–478, 2002.
- [11] A. Tomita, R. Ando, A. Saito, K. Watanabe, and H. Akima, “Effect of interelectrode distance on surface electromyographic signals of vastus intermedius muscle in women and men,” *J. Electromyogr. Kinesiol.*, Oct. 2015.
- [12] B. Afsharipour, K. Ullah, and R. Merletti, “Amplitude indicators and spatial aliasing in high density surface electromyography recordings,” *Biomed. Signal Process. Control*, vol. 22, pp. 170–179, Sep. 2015.
- [13] D. T. Mewett, K. J. Reynolds, and H. Nazeran, “Reducing power line interference in digitised electromyogram recordings by spectrum interpolation,” *Med. Biol. Eng. Comput.*, vol. 42, pp. 524–531, 2004.



# Part III



*Elbow joint angle and force:  
effect on the recorded EMG*



# Chapter VIII

*The effect of elbow joint  
angles and contraction  
levels on the RMS of  
sEMG*





## **The effect of elbow joint angle and contraction level on the RMS of sEMG**

### **Introduction**

Flexion and extension of the arm are frequently used in various activities of daily living. Three muscles that are responsible for elbow flexion movement are biceps brachii, brachialis, and brachioradialis [1]. Thus to allow these movements, a certain correlation between activation of the elbow flexor muscles and the position of the arm should exist. Knowing the relation between muscle activity and the elbow joint angle can be useful in many fields such as the control system of the exoskeleton of the upper limb [2].

Several approaches to correlate the sEMG recorded from one or both superficial elbow flexor muscles have been proposed such as the Principal Component Analysis [3], the Artificial Neural Network [4], [5], the angle-EMG biomechanical model [6], and the mathematical approach with pre-defined angle and load [7]. However, the direct correlation between sEMG and elbow joint angle is still unknown.

In this study, the correlation between sEMG RMS amplitude, recorded from biceps brachii and brachioradialis and elbow joint angle and force, is investigated.

### **Materials and methods**

*Subjects.* Ten healthy sedentary men [median (interquartile range): age 25 (5) years; height 170 (2) cm; weight 70 (16) kg] volunteered to participate in the study. No subject had any known neuromuscular or skeletal impairment. Each subject received a detailed explanation of the study and gave written informed consent prior to participate.

*Experimental procedure.* Participants were sitting on a chair with the arm at 90 degree flexion. The upper arm of the subjects was rested on a brace and the lower arm was in supinated position (see Figure 1). The surface EMG monopolar signals were recorded from biceps brachii (both short head/ SH and long head/ LH) and brachioradialis (BR). The position of each head of the biceps brachii was analyzed using a B-mode ultrasound (TELEMED). Then, we abrade the skin with abrasive paste (Nuprep; Weaver and Company, USA) and cleaned with water. A grid of electrodes (8x6,  $\varnothing=3\text{mm}$ , IED=10mm) was placed on the BB such that both heads of the BB were equally covered. To record the muscle activity from BR muscle, we used a linear array of electrodes (8 electrodes,  $\varnothing=3\text{mm}$ , IED=5mm). An array of electrodes with equal properties was also placed on the triceps to evaluate whether co-contraction exists.

The participants were asked to perform, in random order, isometric contractions at four different contraction levels (10%, 30%, 50% and 100% of the maximum voluntary contraction /MVC) and five elbow joint angles (multiples of 15 degrees

from 75 to 135 degree) against an isometric brace. The MVC was measured for each joint angle as suggested in [8]. The 5s sEMG signals were recorded when the participants performed MVC and 10s for the other tasks. The signals were sampled with 2048 sample/s.

*Signal processing.* The central 3s of the single differential (SD) signals obtained when the participants performed MVC and the central 5s of the SD signals obtained from the other task were processed. Bandpass filtering (20-500 Hz, 2<sup>nd</sup> order Butterworth zero phase filter), power line interference(PLI) attenuation using spectral interpolation [9], bad channel removal, and offset removal in time were performed. The selection of the method to attenuate the PLI is based on the investigation reported in Chapter II, where we found that spectral interpolation is a simple way to attenuate the PLI while maintaining the shape of the signals. Then, the RMS value of each channel of the sEMG map was computed within 500ms epoch.

In this study, we adopted two methods to obtain representative RMS value: 1) calculate the average of the channels whose RMS values are above 70% of the maximum RMS at that epoch, and 2) compute the average of the RMS values from channels inside the muscle active region. The first and second method were applied to the signals obtained from BR and BB muscles respectively. To estimate the muscle active region watershed segmentation [10] is used. The active regions of the muscle, i.e. regions of interest/ROI of the sEMG map, are one or more clustered pixel with a total number of pixels inside the ROI denoted as  $P_{ROI}$ . Then the RMS values inside the selected area were averaged in space as shown in (1).

$$R_k = \frac{1}{P_{ROI}} \sum_{n=1}^{P_{ROI}} \sqrt{\frac{1}{T} \sum_{t=1}^T [S(P_{ROI}, t)]^2} \quad (1)$$

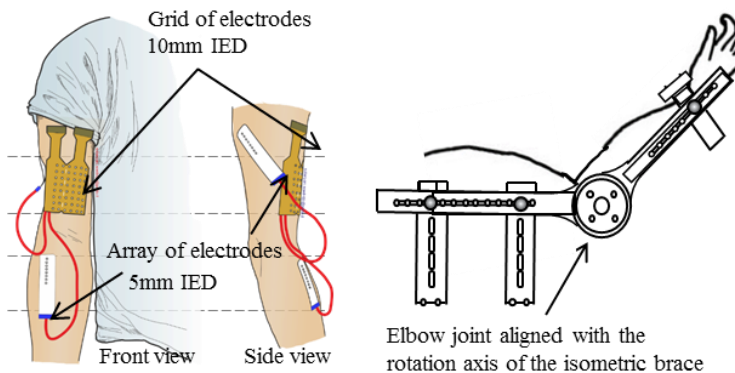


Figure 1. The grid of electrodes was placed on biceps brachii. Each of the participants was asked to perform isometric contraction against an isometric brace. See text for details.

where  $R$  is the RMS value averaged in space at  $k$ th epoch,  $T$  is the length of the epoch, and  $S(P_{ROI}, t)$  is the instantaneous sEMG amplitude located at the channel inside the ROI.

Using these methods, the RMS values coming from electrodes located over the innervations zone (IZ) were excluded and we obtain six averaged RMS values for the sEMG signals acquired at MVC task and ten averaged RMS values for the rest of the task.

*Statistics.* The Spearman rank correlation is used to test the correlation between joint angle and the RMS values obtained from biceps brachii and brachioradialis.

## **Results and discussion**

### *Evaluation on the grid of electrodes*

The sEMG signals acquired with a grid of electrodes are affected by the physical dimension of the electrode, the inter-electrode distance (IED) and the size of the grid. In this study, we used a grid of electrode composed with 48 circular electrodes having 3mm diameter and 10mm IED. In the previous chapter, IED of 10mm shows an error on the RMS value computed in space at each instantaneous sample about  $\pm 15\%$  compared to the RMS value of the interpolated sEMG map (see Figure 6 in Chapter 7). However, these errors may cancel out each other and becomes negligible when we average it in a group of samples (see Figure 8 in Chapter 7). In the same sense, since the RMS of each channel is computed within a 500ms time window, we can conclude that the grid with 10mm IED shall introduce an error of the RMS values (defined in (1)) at about 2.0%.

### *Maximum torque at different elbow joint angles*

For each participant, the torque at MVC at each joint angle is measured and normalized to its maximum value. Then, a quadratic fitting curve is drawn. The plot in Figure 2 shows that the maximum torque is decreased monotonically as the participants extend their arms. This finding is similar to the results reported in [8] although, in their investigation, the upper arm was placed parallel to the trunk.

### *Co-activation of triceps brachii muscle*

Visual analysis was made on the sEMG signals obtained from triceps brachii. Besides the amplitude of the RMS value that is similar to the noise level, propagation of the motor unit action potential is not detected (see Figure 3). The same figure suggests that the non-propagating component of the signals obtained from the triceps brachii could be evidence of the cross talk from the BB muscle.

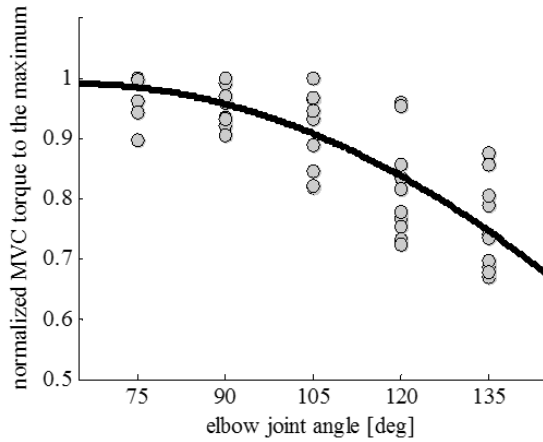


Figure 2. The torque produced at maximal voluntary contraction decreases along with greater elbow joint angle. The values for each subject are normalized with respect to the maximum torque produced by that subject.

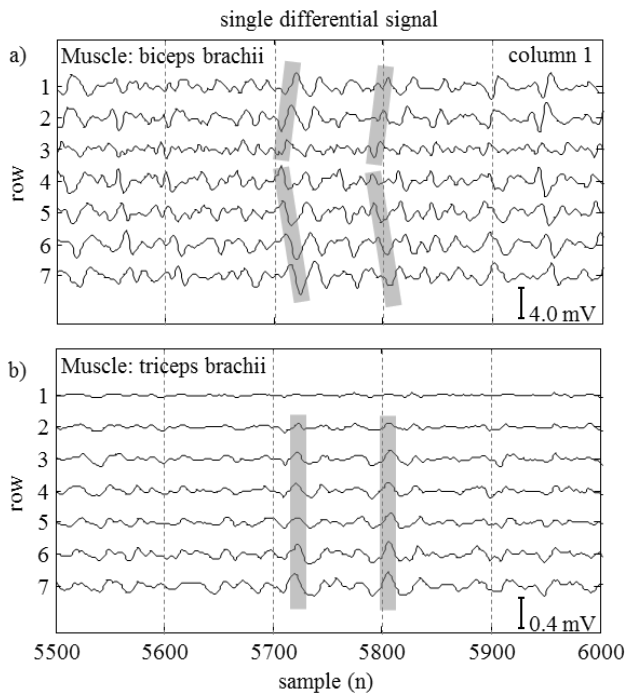


Figure 3. These plots show two single differential signals obtained from a) the first column of the grid of electrodes placed over the biceps brachii (BB) muscle and b) the linear array of electrodes placed over the triceps brachii (TR) muscle of a subject performing MVC at 120° elbow joint angle. The gray lines show the evidence of the propagation of motor unit action potentials in the signals obtained from BB and at the same time, non-propagating components are observed in the signals obtained from TR.

Crosstalk is a phenomenon where the sEMG signals from the active muscle can be detected over the adjacent non-active muscle as a non-propagating component with smaller amplitude [11]. Based on this evidence, we conclude that the triceps brachii is not activated. This finding is not supporting the results in [12] where they found co-activation of antagonist muscle during maximum voluntary contraction of the elbow flexion. This difference might occur since in this study the upper arm of the participant is supported and fixed to the isometric brace.

*Bad channels*

Visual inspection on each sEMG channel is performed to determine bad channels. The number of bad channels found in this study for each recorded set of signals is as high as four channels out of 48 channels for the grid of electrodes and 1 channel out of 8 channels for the array of electrodes. The signals at that bad channels are replaced by the average of their adjacent channels.

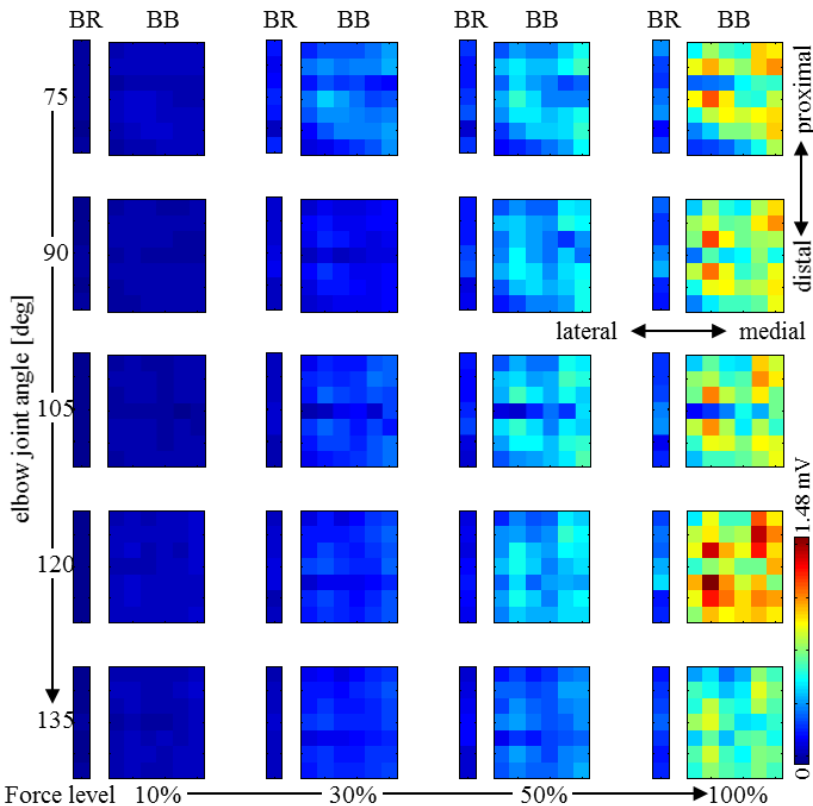


Figure 4. These figures show the effect of elbow joint angle and force level on the single differential RMS map averaged for all the epochs (see text for detail) from one participant. The force level is computed with respect to the maximum voluntary contraction measured on that particular joint angle.



*Selecting muscle active region*

In this study, we analyze the sEMG obtained from two elbow flexor muscles, i.e. biceps brachii and brachioradialis. The activity of these muscles changes according to the force level and elbow joint angle. An example of the muscles' activities measured as RMS values (1) computed for each channel within 0.5s epoch and averaged through all epochs are shown in Figure 4. This figure demonstrates that for this particular subject the activity of both muscles (BB and BR) are increased along with higher force level. As the arm extended, up to 120-degree elbow joint angle, the activity of both muscles increased and then decreased at 135-degree elbow joint angle. To obtain a representative value for each task, we compute the average of RMS values of the channels inside the muscle active region to avoid computational bias from IZ. As mentioned in the section **Materials and Method**, the Watershed algorithm is used to estimate the active region of the BB muscle.

The concept of the watershed algorithm used to segment the sEMG map can be explained as follows. A map of sEMG can be represented as a topographical relief. Pixels with high intensity considered as elevated surface and pixels with low intensity as catchment basins. Then the segmentation lines were estimated by processing the gradient of the map [10] and the result of this method is the estimated active regions or region of interest (see Figure 5). Using this method, we can avoid the RMS values obtained from the channels over the IZ. We obtain the representative RMS value of each epoch at each task as the average of the RMS values that are located inside the muscle active region.

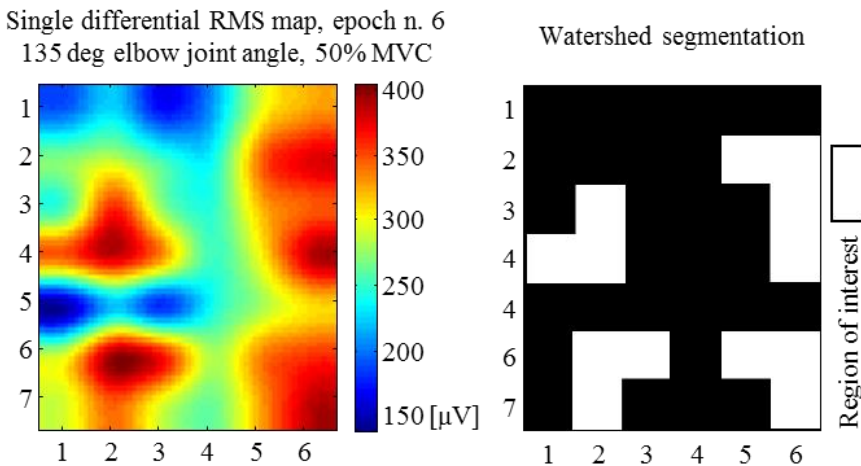


Figure 5. Watershed segmentation estimates the active region of the muscle. The left figure shows an example of a single differential RMS map (interpolation of the map only for display purpose) while the figure on the right is the result of the segmentation. The representative RMS value is obtained by taking the average of the RMS values that located inside the muscle active region (region of interest).

*Activity of biceps brahii short head and long head*

In the first attempt, we would like to evaluate whether the activity of each of the BB heads differs along with changing of the force level and elbow joint angle. This issue has never been addressed before. The grid of electrodes was placed carefully on the biceps after knowing the location of the head. Thus, we can infer that the signals from the first three columns are obtained from the long head (LH) of the biceps brachii and the signals from the last three columns are obtained from the short head (SH) of biceps brachii. Then for each head, the representative RMS value is the average of RMS values inside the active region located at the first three columns and the last three columns for the LH and SH respectively.

Table 1. The Wilcoxon rank sum test was performed to evaluate whether the activity of the short head of biceps brachii is different from the long head. Three of the participants show similar activity between their short head and long head while the other participants show that their short head is more active than the long head. Significant difference of activity between the heads ( $p < 0.05$ ) is denoted with the symbol '+'

Subject	10% MVC				
	75°	90°	105°	120°	135°
A	+			+	
B					
C		+	+		+
D	+			+	
E					
F	+				
G					
H				+	+
I					
J					

Subject	30% MVC				
	75°	90°	105°	120°	135°
A		+			+
B					
C	+				
D					
E					
F			+		
G					
H	+	+			
I					+
J					

Subject	50% MVC				
	75°	90°	105°	120°	135°
A	+				
B					
C			+		
D					
E					
F	+	+			
G		+	+	+	
H		+	+		
I		+			
J					

Subject	100% MVC				
	75°	90°	105°	120°	135°
A			+		
B					
C					+
D					
E					
F		+			
G					
H	+	+			+
I					
J					



The Wilcoxon rank sum test was used to evaluate whether the activity of the short head of the BB muscle is different from the long head. We found that three participants (B, E, and J) had similar muscle activity at both heads while the other participants activated more the SH rather than the LH (see Table 1). However, no general pattern of the activity of each head can be observed from this data.

In the elbow flexion task, the SH of the biceps brachii muscle should be more activate than the LH since the SH is known as a strong flexor while the LH is known as a strong supinator [13]. The differences in the SH and LH activity might derive from different strategies of the muscle contribution for each task.

*Biceps brachi and brachioradialis muscles activities*

Furthermore, we want to evaluate the general activity of the biceps brachii and brachioradialis. Figure 6 shows the boxplot of the representative RMS value at each epoch and at each task obtained from the same subject as in Figure 4. This figure suggests that the activity of both muscles (BB and BR) behave similarly. The RMS value increases at a higher force level and decreases at a larger joint angle. However, this behavior does not occur in the sEMG from the other participants.

Boxplot of the RMS values averaged inside muscle's active area of one subject at each epoch [mV]

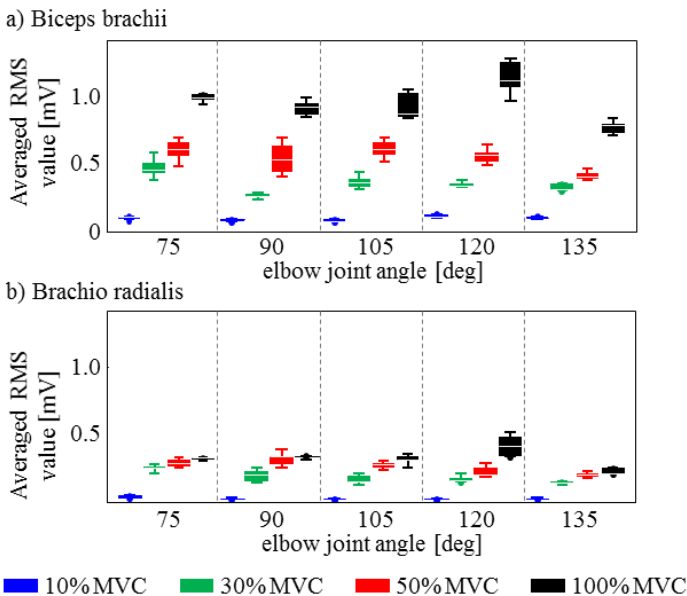


Figure 6. This plot demonstrates the changes in muscle activity of biceps brachii and brachioradialis recorded from a subject while performing isometric contraction at five elbow joint angles and four contraction levels. The average RMS values increase at higher force levels regardless of the elbow joint angle.



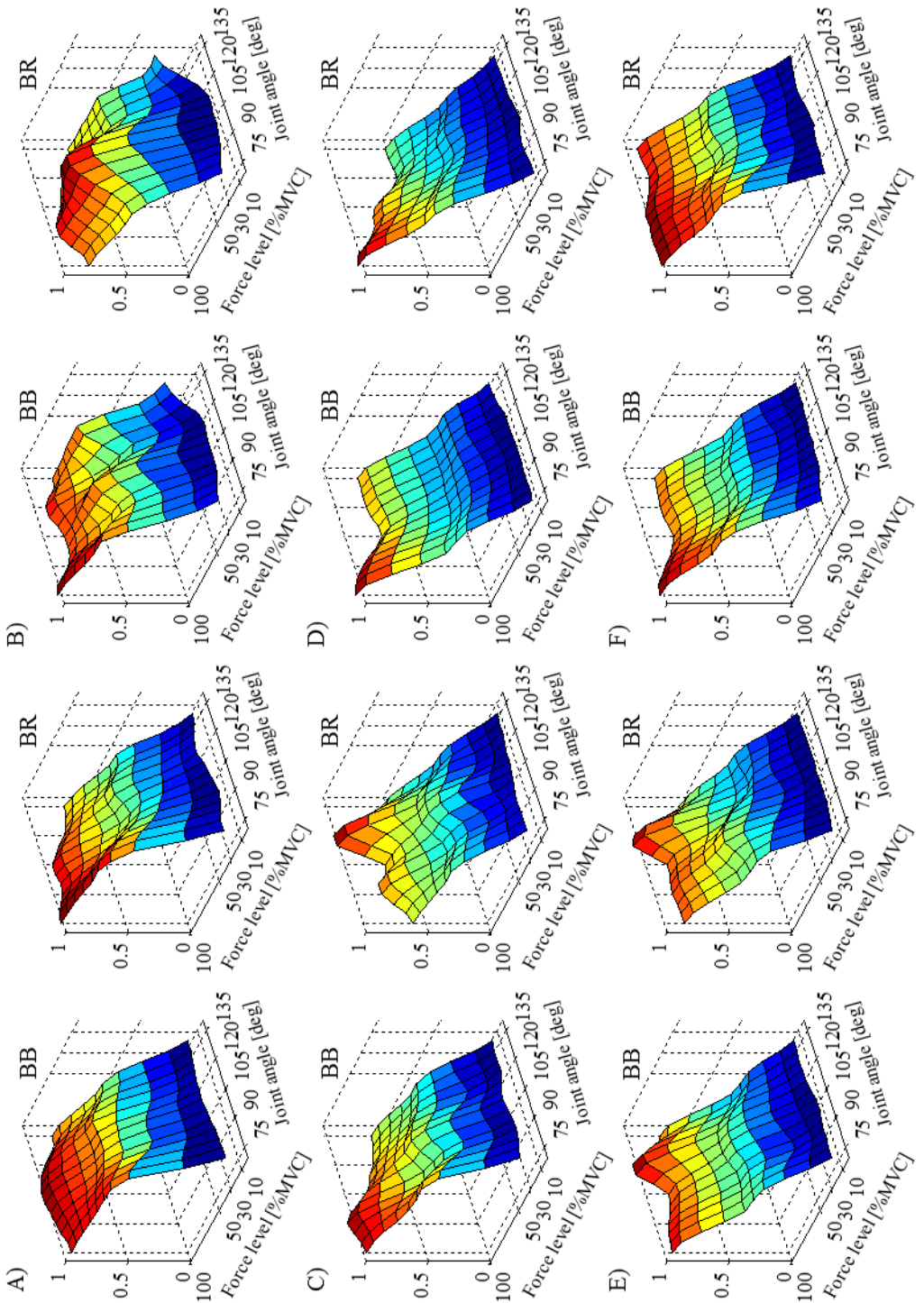
For each submaximal contraction level we have ten epochs and we have six epochs for the MVC. Figure 7 shows the median of the averaged RMS value from all epochs which has been normalized to its maximum value (the plots were interpolated only for demonstration purpose). Five participants show similar behavior on both muscles (participant A-E). The activities of both muscles increase at greater force levels and decrease along the extension of the arm except for the BR muscle of participant C. In contrast with the other participants, two participants (F and G) show that their muscle activities are not affected by different elbow joint angles. The last three participants (H-J) show that their muscle activities increase along with a higher force level and a greater elbow joint angle except for the activity of the BR muscle of participant J.

The Spearman rank correlation test is performed for each participant using the data from all epochs at the same force level and different elbow joint angles (see Table 2). The rho value of zero means that the ranks of one variable do not covary with the ranks of the other variable while the p-value shows the significance level. The RMS values of the BB muscle are monotonically decreased with significant level  $p < 0.05$  along with the arm extension for seven participants (A-C, E, G-H, and J) regardless of the force level except for participants B, E, and J. These three participants, at 10% MVC, show increasing RMS values along with a greater elbow joint angle. Two participants (D and I) show opposite behavior i.e. the RMS values monotonically increase at a greater elbow joint angle. This characteristic also appears on the RMS values of the BR muscle of the same participants. In contrast with the other participants, one participant (F) shows increasing activity of BB and decreasing activity of BR along with the extension of the arm.

We observed that there are three main groupings of the behavior of BB and BR muscle activities. The participants of the first group are those whose muscle activities of biceps brachii and brachioradialis decrease as the joint angles increase (participants A-C, E, G-H, and J). The second group is the participant whose muscle activities of BB and BR increase along with greater elbow joint angle. The third group is the participant whose BB muscle activity increases while the BR muscle activity decreases as the participant extends his arm. The first group corresponds to the results presented in the investigation performed in the dynamic condition reported in [14] which is opposite of the behavior of the second group which is in line with the result reported in [15], [16].

The origin of these differences might come from the fact that the innervation zones (IZ) of the muscle shift along with the changing of the elbow joint angle. It has been reported that the IZ shifts proximally about 4.5-7.00mm with increases in isometric torque [17] and shifts distally up to 30mm along with the extension of the arm. It is well known that the amplitude of sEMG signals recorded from the area over the IZ is significantly different than the other area [18], i.e. in single differential configuration the amplitude is nearly zero [19]–[21]. Investigations [14]–[16] did not locate the IZ which might be the reason for their findings. Another reason for these differences is the unknown activity level of brachialis muscle.

Median of the averaged RMS values obtained from biceps brachii and brachioradialis muscles (value normalized to the maximum)



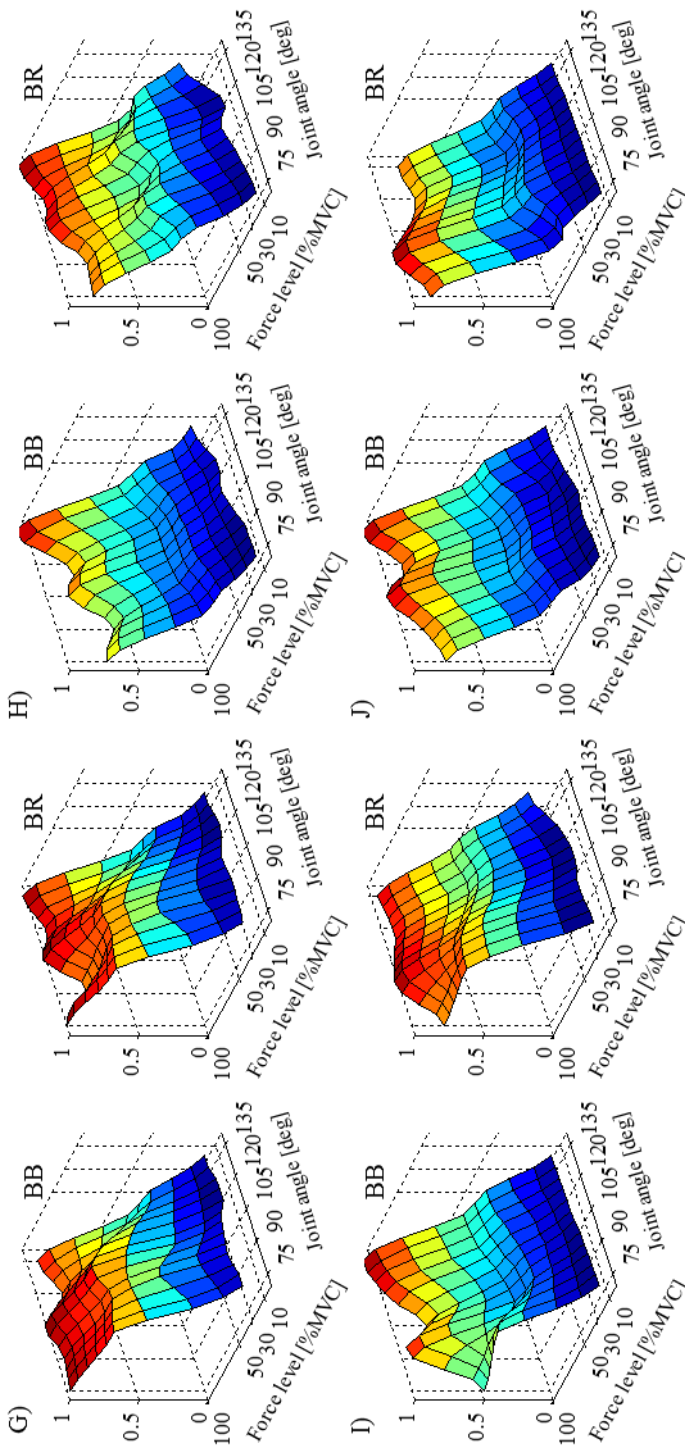


Figure 7. The figures demonstrate the median of the averaged RMS value (see “Materials and method”) obtained from biceps brachii and brachioradialis muscles of ten participants. These values are normalized to its maximum. The median of the averaged RMS value is increased along with higher force level. Greater elbow joint angle implies lower averaged RMS value for seven participants (A-G) but not for three participants (H-J). See text for details.



Table 2. The Spearman rank correlation between the EMG RMS amplitude averaged inside the ROI (defined in (1)) obtained at the same force level and different joint angle.

a) Biceps brachii \* If not stated, p-values are < 0.05

Force level [% MVC]	Rho (p-value) of participant*				
	A	B	C	D	E
10%	-0.22 (> 0.05)	0.08 (> 0.05)	-0.78	0.87	0.44
30%	-0.84	-0.53	-0.77	0.85	-0.02 (> 0.05)
50%	-0.78	-0.40	-0.72	0.86	-0.57
100%	-0.46	-0.54	-0.89	0.55	-0.62

Force level [% MVC]	Rho (p-value) of participant*				
	F	G	H	I	J
10%	0.89	-0.69	-0.94	0.88	0.26 (> 0.05)
30%	0.05 (> 0.05)	-0.73	-0.80	0.69	-0.26 (> 0.05)
50%	0.02 (> 0.05)	-0.74	-0.87	0.81	-0.48
100%	0.69	-0.41	-0.71	0.44	-0.36 (> 0.05)

b) Brachio radialis \* If not stated, p-values are < 0.05

Force level [% MVC]	Rho (p-value) of participant*				
	A	B	C	D	E
10%	-0.42	0.18 (> 0.05)	-0.83	0.70	-0.19 (> 0.05)
30%	-0.96	-0.38	-0.53	0.74	-0.88
50%	-0.88	-0.28	-0.20 (> 0.05)	0.40	-0.89
100%	-0.82	-0.41	0.14 (> 0.05)	0.42	-0.93

Force level [% MVC]	Rho (p-value) of participant*				
	F	G	H	I	J
10%	0.54	-0.64	-0.57	0.78	-0.46
30%	-0.55	-0.71	-0.82	0.60	-0.66
50%	-0.68	-0.72	-0.76	0.30	-0.73
100%	0.16 (> 0.05)	0.22 (> 0.05)	-0.57	-0.45	-0.22 (> 0.05)

\*p-value < 0.05 reflects that the Rho is significantly different from zero

### **Conclusion**

The IZ of the muscle is shifted as the arm extended. To avoid measurement bias caused by the IZ, a grid of electrodes is used.

We found that for most of the participants, the short head of the biceps brachii is more active than the long head. This difference in behavior might be introduced by the different strategies of load sharing between the muscles and the activity of the brachialis muscle which is difficult to measure via surface EMG detection systems.

The results in this work suggest that the activity of the two elbow flexor muscles (biceps brachii and brachioradialis) might depend on the subject. In general, the activity increases as the force levels increase and decreases along with greater elbow joint angle.

However, the results presented in this study might not be correct since we used a grid of electrodes where the diameter of the electrode is 3mm, i.e. the limit of the electrode's size to obtain negligible spatial filtering effect (see Figure 1 in Chapter 5). Moreover, the 10mm IED introduces aliasing in a considerable number of sEMG maps depending on how aliasing is defined (see Figure 9 in Chapter 6).

## REFERENCES

- [1] N. Hamilton, W. Weimar, and K. Luttgens, *Kinesiology: Scientific basis of human motion*, 11th ed. Boston: McGraw-Hill, 2008.
- [2] M. C. F. Castro, E. L. Colombini, P. T. A. Junior, S. P. Arjunan, and D. K. Kumar, “sEMG feature evaluation for identification of elbow angle resolution in graded arm movement,” *Biomed. Eng. Online*, vol. 13, no. 1, pp. 155–164, 2014.
- [3] K. Englehart, B. Hudgins, P. A. Parker, and M. Stevenson, “Classification of the myoelectric signal using time-frequency based representations,” *Med. Eng. Phys.*, vol. 21, no. 6–7, pp. 431–438, 1999.
- [4] S. Suryanarayanan, N. P. Reddy, and V. Gupta, “Acial neural networks for estimation joint angle from EMG signals,” pp. 823–824, 1995.
- [5] Y. Mon and A. Al-Jumaily, “Estimation of Upper Limb Joint Angle Using Surface EMG Signal,” *Int. J. Adv. Robot. Syst.*, p. 1, 2013.
- [6] Y. S. Gao, S. X. Wang, F. Y. Xiao, and J. Zhao, “An angle-EMG biomechanical model of the human elbow joint,” *J. Mech. Med. Biol.*
- [7] H.-J. Yu, A. Y. Lee, and Y. Choi, “Human elbow joint angle estimation using electromyogram signal processing,” *IET Signal Process.*, vol. 5, no. 8, p. 767, 2011.
- [8] E. P. Doheny, M. M. Lowery, D. P. FitzPatrick, and M. J. O’Malley, “Effect of elbow joint angle on force-EMG relationships in human elbow flexor and extensor muscles,” *J. Electromyogr. Kinesiol.*, vol. 18, no. 5, pp. 760–770, 2008.
- [9] D. T. Mewett, K. J. Reynolds, and H. Nazeran, “Reducing power line interference in digitised electromyogram recordings by spectrum interpolation,” *Med. Biol. Eng. Comput.*, vol. 42, pp. 524–531, 2004.
- [10] T. M. M. Vieira, R. Merletti, and L. Mesin, “Automatic segmentation of surface EMG images : Improving the estimation of neuromuscular activity,” *J. Biomech.*, vol. 43, no. 11, pp. 2149–2158, 2010.
- [11] D. Farina, R. Merletti, B. Indino, and T. Graven-Nielsen, “Surface EMG Crosstalk Evaluated from Experimental Recordings and Simulated Signals: Reflections on Crosstalk Interpretation, Quantification and Reduction,” in *Methods of Information in Medicine*, 2004, vol. 43, no. 1, pp. 30–35.
- [12] I. Bazzucchi, P. Sbriccoli, and G. Marzattinocci, “Coactivation of the elbow antagonist muscles is not affected by the speed of movement in isokinetic exercise,” no. February, pp. 191–199, 2006.
- [13] L. A. Pederzini, D. Eygendaal, and M. Denti, *Elbow and Sport*. Springer, 2016.
- [14] V. Linnamo, V. Strojnik, and P. V. Komi, “Maximal force during eccentric and isometric actions at different elbow angles,” *Eur. J. Appl. Physiol.*, vol. 96, no. 6, pp. 672–678, 2006.
- [15] T. Kleiber, L. Kunz, and C. Disselhorst-Klug, “Muscular coordination of biceps brachii and brachioradialis in elbow flexion with respect to hand position,” *Front. Physiol.*, vol. 6, no. Aug, pp. 1–5, 2015.
- [16] S. C. F. A. von Werder and C. Disselhorst-Klug, “The role of biceps brachii and brachioradialis for the control of elbow flexion and extension movements,” *J. Electromyogr. Kinesiol.*, vol. 28, pp. 67–75, 2016.

- [17] J. M. DeFreitas, P. B. Costa, E. D. Ryan, T. J. Herda, J. T. Cramer, and T. W. Beck, "An examination of innervation zone movement with increases in isometric torque production," *Clin. Neurophysiol.*, vol. 119, no. 12, pp. 2795–2799, Dec. 2008.
- [18] T. J. Herda, J. M. Zuniga, E. D. Ryan, C. L. Camic, H. C. Bergstrom, D. B. Smith, J. P. Weir, J. T. Cramer, and T. J. Housh, "Quantifying the effects of electrode distance from the innervation zone on the electromyographic amplitude versus torque relationships.," *Physiol. Meas.*, vol. 34, no. 3, pp. 315–24, Mar. 2013.
- [19] A. Rainoldi, G. Melchiorri, and I. Caruso, "A method for positioning electrodes during surface EMG recordings in lower limb muscles," *J. Neurosci. Methods*, vol. 134, no. 1, pp. 37–43, 2004.
- [20] M. Barbero, R. Merletti, and A. Rainoldi, *Atlas of muscle innervation zones: understanding surface electromyography and its applications*. Springer Science & Business Media, 2012.
- [21] D. Farina, R. Merletti, M. Nazzaro, and I. Caruso, "Effect of joint angle on EMG variables in leg and thigh muscles," *Eng. Med. Biol. Mag. IEEE*, vol. 20, no. 6, pp. 62–71, 2001.





# General Conclusions





The idea of the works presented is to introduce a new perspective on surface EMG analysis. Several important issues that might affect the result of sEMG measurement such as attenuating power line interference (PLI), selection of digital low pass filter to extract the sEMG envelope, the effect of subcutaneous layer thickness, the properties of 2D detection system are presented and discussed. These issues are important to provide a correct sEMG measurement, i.e. we can reconstruct the continuous muscle activity in space and obtain correct properties (RMS value, the centre of mass, etc).

An ideal PLI attenuator should maintain the shape of the signal while attenuating the frequency component of the power line. Signal shape is important for some application such as computation of conduction velocity. We found that to attenuate PLI of a short signal ( $\pm 3s$ ), spectral interpolation technique is preferred. To maintain signal shape and online application, an adaptive noise canceller with phase locked loop (ANC-PLL) is suggested.

There are infinite configurations of digital low pass filters that can be used to extract the envelope of a rectified sEMG signal. In this study, we evaluate the performances of 160 filters. The lowest root mean square error computed between the average rectified value (ARV) of the input signal and the output signal envelope is 7.61% (1<sup>st</sup> order zero phase low pass Elliptic filter with 1Hz cutoff frequency). The shortest rise time is 24ms (2<sup>nd</sup> order one directional low pass Elliptic filter with 10Hz cutoff frequency). The shortest computation time is 0.48ms (1<sup>st</sup> order one directional low pass Elliptic filter with 3Hz cutoff frequency). We found that a filter which has the best performance over all criteria does not exist. A global best filter is selected by choosing a filter that has zero delays and close to the data boundary which is obtained with a curve fitting line. The results suggest that the 2<sup>nd</sup> order zero phase Butterworth low pass filter (2<sup>nd</sup> order at each direction) with 5Hz cutoff frequency shows the best performance.

A thicker subcutaneous layer (SL) implies smaller surface EMG amplitude. Results from 10 subjects show that the thickness of the SL above the biceps brachii muscle decrease significantly as the arms extend in rest condition. The thickness of the SL also decreases significantly at 75° elbow joint angle when the contraction level increases from rest condition to the maximum voluntary contraction. We found that the averaged RMS values tend to decrease as thicker SL with 32.4 dB/decade.

As the amplitude of the EMG signals recorded in single differential configuration above the innervation zones (IZ) is nearly zero and the IZ shifts as the arm extends, a linear array of electrodes or a grid of electrodes is needed such that the amplitude obtained from the area above the IZ can be avoided. The existing guidelines for sEMG measurement, i.e. SENIAM, are applicable for electrodes placed in the bipolar configuration. Therefore, characterization of sEMG in space to determine the ideal configuration of 2D sEMG detection system is needed. Three factors that bounded to the 2D sEMG detection system are the physical dimension of the electrode, the distance between the electrodes

(IED), and the limited size of the detection system. In this study, the first and second factors are discussed.

Each electrode of the detection system acts as low pass spatial filter that averages the potential over the electrode area. A greater size of electrode implies higher low pass effect. We demonstrate that larger electrode with 10mm IED introduces higher error in the power estimation of an instantaneous sEMG map compare to the map obtained with pin-like electrode and 10mm IED. In some of the maps, larger electrode tends to underestimate the power estimation and in some other maps it tends to overestimate. When we compare the maps obtained with different IED and of its continuous sEMG map, larger IED tends to underestimate the power estimation which is obvious since larger IED attenuate the higher spatial frequency component of the sEMG maps.

The ideal distance between the electrodes or sampling frequency in space is related to the spatial frequency component of the instantaneous sEMG map. According to the Nyquist-Shannon theorem, to be able to reconstruct the continuous map without error, the sampling frequency in space should be greater than twice of the highest spatial frequency of the map. We establish two approaches to determine the highest spatial frequency component of the map: 1)  $f_{\max}$  based on 90% power, and 2)  $f_{\max}$  based on the power of the harmonics. Based on the first approach, the median of sEMG spatial bandwidth is 62.5 cycles/m for sEMG recorded from biceps brachii and 56.25 cycles/m for sEMG recorded from medial deltoid. Based on the second approach, the median of sEMG spatial bandwidth is 37.5 cycles/m for sEMG recorded from biceps brachii and 21.88 cycles/m for sEMG recorded from medial deltoid.

Larger IED leads to aliasing, i.e. loss of information and wrong conclusions. In fact, we show that the relative error between the RMS of each “alias-free” maps (evaluated at 5mm IED) resampled with different IED and RMS of the same map obtained with 0.1mm IED increases as the IED increase. However, if we take the average of RMS in a group of 1000 maps, these errors are negligible.

Considerations mentioned above are necessary for analyzing the sEMG RMS amplitude obtained from biceps brachii and brachioradialis at different elbow joint angles and different contraction levels. The relationship between the EMG signal amplitude and joint angle has been and is still discussed with diverging results. One of the possible reasons of disagreement is the location of IZ which is not considered in most of the investigations. Although we cannot generalize the results obtained in this study, we demonstrate that the activity of the two elbow flexor muscles (biceps brachii and brachioradialis) might depend on the subject. This difference in behavior might be introduced by the different strategies of load sharing between the muscles and the activity of the brachialis muscle which is difficult to measure via surface EMG detection systems.

